

Aus dem

Institut für Kardiovaskuläre Physiologie und Pathophysiologie im Walter-Brendel-Zentrum für Experimentelle Medizin

Ludwig-Maximilians-Universität München



Spatiotemporal Dynamics of Nuclear Positioning during Amoeboid Migration

Dissertation

zum Erwerb des Doctor of Philosophy (Ph.D.)

an der Medizinischen Fakultät der

Ludwig-Maximilians-Universität München

vorgelegt von

Janina Kroll

aus

Starnberg

Jahr

2024

Mit Genehmigung der Medizinischen Fakultät der
Ludwig-Maximilians-Universität München

Erstes Gutachten: Prof. Dr. Jörg Renkawitz

Zweites Gutachten: Priv. Doz. Dr. Markus Moser

Drittes Gutachten: Prof. Dr. Michael Kiebler

Viertes Gutachten: Prof. Dr. Florian Gärtner

Dekan: Prof. Dr. med. Thomas Gudermann

Tag der mündlichen Prüfung: 08.04.2024



Dekanat Medizinische Fakultät
Promotionsbüro



Affidavit

Kroll, Janina

Surname, first name

Großhaderner Str. 9

Street

82152 Planegg-Martinsried, Germany

Zip code, town, country

I hereby declare, that the submitted thesis entitled

“Spatiotemporal Dynamics of Nuclear Positioning during Amoeboid Migration”

is my own work. I have only used the sources indicated and have not made unauthorised use of services of a third party. Where the work of others has been quoted or reproduced, the source is always given.

I further declare that the dissertation presented here has not been submitted in the same or similar form to any other institution for the purpose of obtaining an academic degree.

Munich, 16.04.2024

Place, Date

Janina Kroll

Signature doctoral candidate



Confirmation of congruency between printed and electronic version of the doctoral thesis

Kroll, Janina

Surname, first name

Großhaderner Str. 9

Street

82152 Planegg-Martinsried, Germany

Zip code, town, country

I hereby declare, that the submitted thesis entitled

“Spatiotemporal Dynamics of Nuclear Positioning during Amoeboid Migration”

is congruent with the printed version both in content and format.

Munich, 16.04.2024

Place, Date

Janina Kroll

Signature doctoral candidate

Table of Contents

Affidavit.....	3
Confirmation of congruency between printed and electronic version of the doctoral thesis.....	4
Table of Contents	5
List of Abbreviations.....	6
List of Publications	7
1. Contribution to the Publications.....	8
1.1 Contribution to paper I.....	8
1.2 Contribution to paper II	8
2. Introductory Summary	9
2.1 Summary	9
2.2 Cell migration	10
2.2.1 Migration modes	10
2.2.2 Shape coordination during cell motility	12
2.2.3 Guidance cues	13
2.3 Organelle positioning.....	14
2.3.1 Centrosome positioning.....	15
2.3.2 Nuclear positioning.....	15
2.4 Aims.....	17
3. Paper I: Adaptive Pathfinding by Nucleokinesis during Amoeboid Migration.....	18
4. Paper II: Centrosome Positioning in Migrating <i>Dictyostelium</i> Cells	61
References.....	82
Acknowledgements.....	90

List of Abbreviations

2D	2-dimensional
3D	3-dimensional
Arp2/3	Actin-related protein 2/3
cAMP	Cyclic adenosine monophosphate
CCL19	C-C motif chemokine ligand 19
CCL21	C-C motif chemokine ligand 21
CCR7	CC-chemokine receptor 7
DC	Dendritic cell
ECM	Extracellular matrix
ESCRT	Endosomal sorting complex required for transport
GEF	Guanine nucleotide exchange factor
GFP	Green fluorescent protein
GTP	Guanosine triphosphate
INM	Interkinetic nuclear migration
LINC	Linker of nucleoskeleton and cytoskeleton
LPA	Lysophosphatidic acid
MMP	Matrix metalloproteinase
MT	Microtubule
MTOC	Microtubule-organizing center
NK (cell)	Natural killer (cell)
RFP	Red fluorescent protein
RNA	Ribonucleic acid
TAN (lines)	Transmembrane actin-associated nuclear (lines)

List of Publications

List of publications used for the cumulative thesis

1. **Kroll J**, Hauschild R, Kuznetcov A, Stefanowski K, Hermann MD, Merrin J, Shafeek L, Müller-Taubenberger A, Renkawitz J (2023) Adaptive Pathfinding by Nucleokinesis during Amoeboid Migration. *The EMBO Journal*: e114557. <https://doi.org/10.15252/embj.2023114557>
2. Ishikawa-Ankerhold H, **Kroll J**, van den Heuvel D, Renkawitz J, Müller-Taubenberger A (2022) Centrosome Positioning in Migrating *Dictyostelium* Cells. *Cells* 11: 1776. <https://doi.org/10.3390/cells11111776>

Complete list of publications

1. **Kroll J**, Hauschild R, Kuznetcov A, Stefanowski K, Hermann MD, Merrin J, Shafeek L, Müller-Taubenberger A, Renkawitz J (2023) Adaptive Pathfinding by Nucleokinesis during Amoeboid Migration. *The EMBO Journal*: e114557. <https://doi.org/10.15252/embj.2023114557>
2. Ishikawa-Ankerhold H, **Kroll J**, van den Heuvel D, Renkawitz J, Müller-Taubenberger A (2022) Centrosome Positioning in Migrating *Dictyostelium* Cells. *Cells* 11: 1776. <https://doi.org/10.3390/cells11111776>
3. **Kroll J**, Ruiz-Fernandez MJA, Braun MB, Merrin J, Renkawitz J (2022) Quantifying the Probing and Selection of Microenvironmental Pores by Motile Immune Cells. *Current Protocols* 2: e407. <https://doi.org/10.1002/cpz1.407>

Submitted manuscripts

1. **Kroll J**, Renkawitz J. Principles of Organelle Positioning and Polarity in Motile and Non-motile Cells. *Submitted Review*.
2. Schmitt MT, Ruiz-Fernandez MJA, Stefanowski K, **Kroll J**, Hauschild R, Merrin J, Penz T, Kiermaier E, Bock C, Straub T, Renkawitz J. Mechanical Centrosome Fracturing during Cell Navigation. *Submitted Article*.

I. Contribution to the Publications

I.1 Contribution to paper I

Kroll J, Hauschild R, Kuznetsov A, Stefanowski K, Hermann MD, Merrin J, Shafeek L, Müller-Taubenberger A, Renkawitz J (2023) Adaptive Pathfinding by Nucleokinesis during Amoeboid Migration. *The EMBO Journal*: e114557. <https://doi.org/10.15252/embj.2023114557>

I performed all experiments shown in Figure 2B, Figure 3A-C and 3F-H, Figure 4, Figure 5D-H, Figure 6, Figure EV2, Figure EV3, Figure EV4, Figure EV5 (supervision of the Latrunculin A titration experiments in Figure EV5A and B), Appendix Figure S1 (excluding the data in 3D collagen matrices in Appendix Figure S1), Appendix Figure S2, Appendix Figure S3, Appendix Figure S4, Appendix Figure S5, Appendix Figure S6, and Appendix Figure S7. I did the analysis for the data shown in Figure 2B, Figure 3E, Figure 4B-D, Figure 5E-H, Figure 6, Figure EV2, Figure EV4A-C, Figure EV5A-B (supervision) and EV5D-E, Appendix Figure S1 (excluding the data in 3D collagen matrices in Appendix Figure S1), Appendix Figure S2, Appendix Figure S4B-C, and Appendix Figure S6E-F. In addition, I performed the analysis in Figure 3B-C and 3G-H, Figure 4G-J, Figure EV3, Figure EV4D-G, Figure EV5C and EV5F-I, Appendix Figure S3, Appendix Figure S5, and Appendix Figure S6A-D in collaboration with RH (software). The workflow for the analysis of nucleokinesis in the blocked Y-channels is depicted in Appendix Figure S2, in which I performed the identification of nucleokinesis events, segmentation of the MTOC, and tracking of nucleus and MTOC. Furthermore, I designed the microchannels for pore size decision experiments (Figure 2A and Figure EV1A) and for path choices in competing chemokines and pore size gradients (Figure 2B-L, Figure 5A-C, and Figure EV1C-E). I wrote the Materials and Methods Section, Movie Legends, and parts of the Figure Legends. Additionally, I generated the movies, contributed to manuscript writing and creation of the figures.

I.2 Contribution to paper II

Ishikawa-Ankerhold H, **Kroll J**, van den Heuvel D, Renkawitz J, Müller-Taubenberger A (2022) Centrosome Positioning in Migrating *Dictyostelium* Cells. *Cells* 11: 1776. <https://doi.org/10.3390/cells11111776>

I performed all microchannel and -pillar assays shown in Figure 1, Figure 4, Figure S1a-f and Figure S2. I did the analysis for the data shown in Figure S1a-e and Figure S2. I contributed to writing parts of the Materials and Methods Section and parts of the Figure Legends. Additionally, I assisted with reviewing and editing of the draft.

2. Introductory Summary

2.1 Summary

Cell migration is crucial in many different physiological and developmental processes as well as in the context of diseases (Yamada & Sixt 2019). During migration, cells are surrounded by complex microenvironments, ranging from the extracellular matrix or other tissue cells in multicellular organisms to soil in the case of migrating single cell organisms (Müller-Taubenberger et al. 2013, Kameritsch & Renkawitz 2020). The microenvironment provides motile cells with diverse cues that guide them along their path of migration. It is increasingly well understood how cells perceive and respond to these guidance cues (SenGupta et al. 2021), but it is not known how cells coordinate and respond to multiple competing signals at the same time. The publication Kroll J, Hauschild R, Kuznetsov A, Stefanowski K, Hermann MD, Merrin J, Shafeek L, Müller-Taubenberger A, Renkawitz J (2023) Adaptive Pathfinding by Nucleokinesis during Amoeboid Migration. *The EMBO Journal*: e114557 aimed to elucidate the principles of how amoeboid cells migrate and navigate in heterogeneous microenvironments composed of multiple guidance cues. During their migration, amoeboid cells employ complex and dynamic cell shapes characterized by multiple protrusions (Bodor et al. 2020) that explore the immediate local microenvironment for guidance cues. Using dendritic cells and T cells as models for amoeboid migration, I identified rapid and long-distance nucleokinesis (nuclear positioning relative to cell movement) as a novel factor of navigational pathfinding in microenvironments of competing guidance cues during amoeboid migration. To mimic microenvironments of heterogeneous mechanochemical composition, I designed microchannels to measure chemical guidance by different chemokine concentrations and simultaneously analyze mechanical pore size decisions in a tightly controlled environment. Using these reductionistic and highly defined microenvironments, I discovered that leukocytes use nucleokinesis to flexibly navigate in competing chemokine and pore size cues. To uncouple the process of nucleokinesis from effects that might be caused by cellular squeezing, I generated microchannels leading to a junction with one dead-end and one open path leading to cells reorienting out of the dead-end into the open path. Using dendritic cells with markers for the centrosome and nucleus, I found that nucleokinesis in amoeboid migrating leukocytes comprises a two-step polarity switch in the nucleus-MTOC axis with the MTOC leading the way out of the dead-end followed by the nucleus, which subsequently overtakes the MTOC to restore the initial nucleus-MTOC axis configuration. Further experiments with pharmacological inhibitors for different cytoskeletal components and various knockout lines revealed that nucleokinesis is driven by actomyosin contractility.

The publication Ishikawa-Ankerhold H, Kroll J, van den Heuvel D, Renkawitz J, Müller-Taubenberger A (2022) Centrosome Positioning in Migrating *Dictyostelium* Cells. *Cells* 11: 1776 aimed to systematically test centrosome positioning in the single cell amoeba *Dictyostelium discoideum*. Using diverse microenvironments, we identified that *Dictyostelium discoideum* preferentially migrates with the nucleus in front of the centrosome, with the centrosome stabilized around the cell center. This held true during migration towards cAMP and folic acid as chemoattractants in different developmental stages, as well as diverse microenvironments, such as 2-dimensional substrates, confining microchannels, and 3-dimensional hydrogel or collagen matrices. These findings suggest that the nucleus-MTOC axis configuration in migrating amoeboid cells is conserved. As *Dictyostelium discoideum* is in general a widely studied model organism for amoeboid migration (Devreotes & Zigmond 1988, Andrew & Insall 2007, Jin et al. 2009, Müller-Taubenberger et al. 2013) and as we could show that the nucleus-MTOC axis is conserved between the single cell amoeba and amoeboid migrating leukocytes (Renkawitz et al. 2019), the question remained if nucleokinesis was also

conserved between these two species. Indeed, in the publication Kroll et al. 2023, I could show that adaptive pathfinding by nucleokinesis is a general component of amoeboid migration consisting of a two-step polarity switch in the nucleus-MTOC axis driven by myosin-II forces in leukocytes and the amoeba *Dictyostelium discoideum*.

In summary, the two publications identify (i) the nucleus forward configuration as a conserved feature of amoeboid migration and (ii) nucleokinesis as a general and conserved feature of amoeboid migrating cells to ensure adaptive pathfinding in microenvironments of heterogenous mechanochemical composition. As adaptation to multiple competing guidance cues is probably relevant for most cells migrating in complex environments, these findings indicate a general role for nucleokinesis during adaptive pathfinding in migrating cells.

2.2 Cell migration

Cell migration is crucial for diverse functions in biology, such as organismal development, tissue maintenance, immune responses, and brain morphogenesis. Furthermore, it is essential for cancer dissemination or migration of unicellular organisms, such as parasites and single cell amoebae (te Boekhorst et al. 2016). During migration, cells are surrounded by complex microenvironments necessitating the ability to adapt or interact with their local surrounding. These surroundings can differ strongly between cell types and contexts, ranging from extracellular matrix (ECM), tissue cells or interstitial fluid in multicellular organisms to soil in case of migrating single cell organisms, such as the amoeba *Dictyostelium discoideum* (Müller-Taubenberger et al. 2013, Kameritsch & Renkawitz 2020). For example, during innate and adaptive immune responses, leukocytes (white blood cells) move very efficiently through the body of multicellular organisms encountering a variety of environments, such as the vasculature or interstitium (Kameritsch & Renkawitz 2020). Circulating leukocytes in the blood or lymphatic system need to enter tissues by active migration for surveillance and upon inflammation (Lämmermann & Germain 2014, Nourshargh & Alon 2014). While some immune cell types become sessile during embryonic development, most leukocytes exit the bone marrow and thymus to execute their specific effector functions (Weninger et al. 2014). In contrast, the social amoeba *Dictyostelium discoideum* lives in the soil (Müller-Taubenberger et al. 2013). In its vegetative growth phase, it feeds on bacteria using folic acid as chemoattractant to move towards its prey (Pan et al. 1972). In the single cell stage *Dictyostelium* cells undergo mitotic division but can adapt in times of starvation by secreting cAMP to assemble into multicellular aggregates which form fruiting bodies with spores that can resist unfavorable environmental conditions (van Driessche et al. 2002).

2.2.1 Migration modes

To adapt to a variety of environments, different cell types or organisms developed a variety of migration modes, such as mesenchymal, amoeboid, lobopodial or even collective migration (Yamada & Sixt 2019).

Mesenchymal migration is characterized by actin polymerization at the leading edge of the cell, which pushes against the plasma membrane generating the force to move the entire cell forward. This requires strong adhesion to the substrate to couple the intracellularly generated actin force to the extracellular microenvironment. This adhesive connection is mediated by focal adhesions (Doyle et al. 2009, Caswell & Zech 2018). Focal adhesions are formed by integrin transmembrane receptors that bind to extracellular ECM components, intracellular signaling proteins, and force transducing proteins, such as talin and vinculin, that connect the focal adhesion complex to the actin cytoskeleton (Moser et al. 2009, Doyle et al. 2022). Mesenchymal migration is rather slow ($< 1 \mu\text{m}/\text{min}$) due to the necessity to detach adhesions at the cell rear (Pollard & Borisy 2003, Bear & Haugh 2014). Notably,

the mesenchymal migration mode involves proteolytic degradation of the ECM by secreting proteases to enlarge pores or generate tunnels in the matrix for the cell to migrate through (Figure 1) (Wolf et al. 2013). For instance, fibroblasts, various stem cells, and some cancer cells employ this mode of migration (SenGupta et al. 2021).

Amoeboid migrating cells are characterized by a rounded cell morphology, low adhesiveness, and frequent changes in their cell shape driven by actin protrusions or membrane blebs, indicating their high contractility (Lämmermann & Sixt 2009, Paluch et al. 2016). In contrast to mesenchymal migration, amoeboid migration usually does not involve remodeling of the ECM (Wolf et al. 2003). Thus, the movement of amoeboid cells through narrow ECM pores relies on squeezing or mechanical widening of pores in their microenvironment (Pflücke & Sixt 2009, Barzilai et al. 2017, Gärtner et al. 2022). Additionally, amoeboid migrating leukocytes usually position their nucleus in front of the centrosome, which is in contrast to mesenchymal cells migrating with the centrosome in front (Figure 1) (Gundersen & Worman 2013, Renkawitz et al. 2019). It has been shown that immune cells, such as dendritic cells (DCs) and T cells use this forward nuclear positioning as a mechanical guide to facilitate pore decisions, leading to migration along the path of least resistance (Renkawitz et al. 2019).

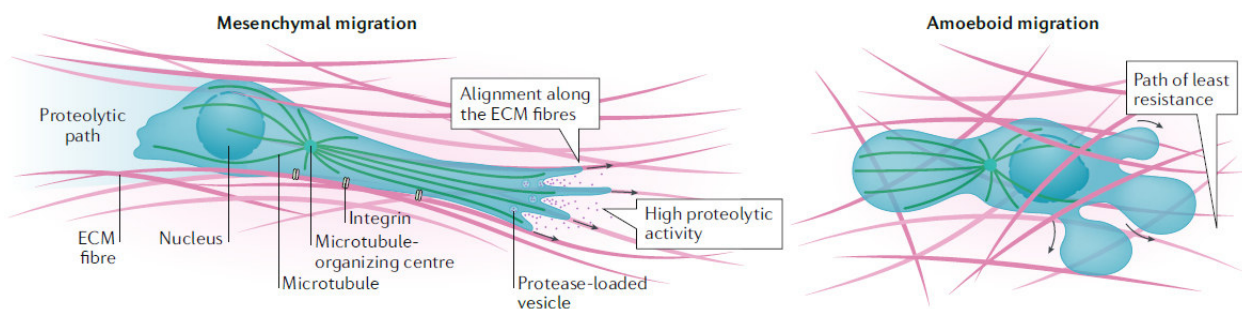


Figure 1: Mesenchymal and amoeboid migration mode. Mesenchymal migration involves strong adhesion to the ECM and proteolytic activity. The centrosome (microtubule-organizing center (MTOC)) is located in front of the nucleus. In contrast, amoeboid migration requires no adhesion or proteolytic activity. The centrosome usually locates behind the nucleus. (From Yamada & Sixt 2019, reproduced with permission of Springer Nature)

Amoeboid migration is further defined by a rapidly changing cell shape which comprises frequent protrusion formation and retraction cycles (Figure 2). Protrusions are formed by the actin cytoskeleton either pushing against the plasma membrane or contracting to generate a flow of cytosol along a hydrostatic pressure gradient that deforms the plasma membrane, the latter being myosin-dependent (Mitchison & Cramer 1996, Paluch et al. 2005). Notably, these mechanisms are not exclusive and can occur simultaneously as shown in *Dictyostelium* cells indicating that a balance between both mechanisms is likely to determine the amoeboid migration mode (Yoshida & Soldati 2006). Amoeboid migrating leukocytes are able to migrate adhesion-independent solely by protrusion of the actin network at the lamellipodium and squeezing by actomyosin contractility at the cell rear whenever cells encounter 3-dimensional surroundings (Lämmermann et al. 2008). Forward movement of the cell is achieved by generating traction forces onto the substrate using only the retrograde forces of actin polymerization (Renkawitz et al. 2009, Renkawitz & Sixt 2010). Furthermore, it has been shown that Arp2/3-nucleated perinuclear actin facilitates squeezing through tight pores in migrating dendritic cells (Thiam et al. 2016), while high myosin II activity is selectively needed for dendritic cell migration in highly confined microenvironments (Barbier et al. 2019).

Next to mesenchymal and amoeboid migration modes, lobopodial migration has been more recently identified as an additional migration mode (Petrie & Yamada 2015). Lobopodial migration is

characterized by high contractility that generates asymmetric intracellular pressure to push the plasma membrane forward. The nucleus can act as piston by dividing the cytoplasm into a front and rear compartment, thereby increasing the hydrostatic pressure at the leading edge (Petrie et al. 2014). Notably, cells are also able to migrate collectively in the same direction, requiring highly coordinated responses to their environment (Mayor & Etienne-Manneville 2016).

The following thesis will focus on amoeboid migrating cells, employing leukocytes and *Dictyostelium* cells as models for amoeboid migration. Yet, it is important to mark the plasticity of these migration modes as cells are able to flexibly switch between them depending on the context and the environment they are migrating in (Yamada & Sixt 2019).

2.2.2 Shape coordination during cell motility

A hallmark of amoeboid migration is a highly dynamic and complex cell shape. Amoeboid cells are able to rapidly and simultaneously form multiple protrusions that intrinsically display complex morphologies (Lämmermann & Sixt 2009). These complex protrusions grow remarkably quickly (10-100 $\mu\text{m}/\text{min}$) and have been shown to form rosettes from multiple, interleaved lamella (Figure 2) (Fritz-Laylin et al. 2017).

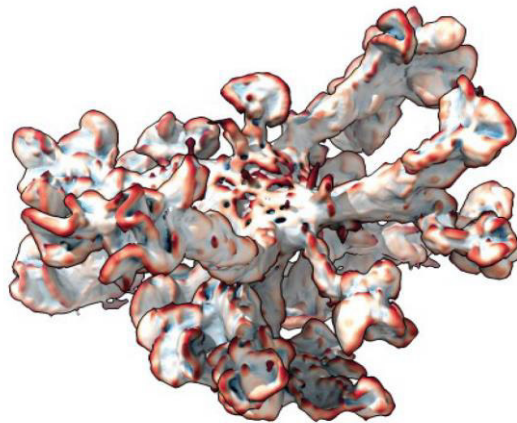


Figure 2: Complex cell shape in amoeboid migrating cells. Light-sheet microscopy of a dendritic cell in a 3D collagen matrix showing multiple protrusions. (From Renkawitz et al. 2019, reproduced with permission from Springer Nature)

Therefore, a major challenge of the highly dynamic cell shapes, which amoeboid cells employ while migrating in complex 3-dimensional (3D) environments, is the coordination of protrusion formation and retraction cycles (Bodor et al. 2020). To tackle this challenge, migrating cells rely on signal transduction pathways that originate locally and propagate throughout the cell (Devreotes et al. 2017, Pal et al. 2019). For example, neutrophils utilize a mechanical feedback loop, where actin retrograde flow leads to myosin accumulation and contraction at the cell rear and thereby increases persistence and turning efficiency (Tsai et al. 2019). In general, cortical actomyosin is a major contributing factor to cell shape (Quintanilla et al. 2023). Especially myosin-II is necessary for coordination of bleb formation and retraction (Paluch et al. 2005, Charras et al. 2006). Moreover, deletion of the small GTPase Cdc42 causes entanglement of dendritic cells in 3D-environments due to dysregulated protrusion dynamics (Lämmermann et al. 2009). Similarly, disruption of DOCK8 (upstream regulator of Cdc42) leads to cell shape deformations and migration defects in DCs, T cells, and NK cells (Harada et al. 2012, Zhang et al. 2014). In addition to cell shape regulation by the actin cytoskeleton, the depolymerization of microtubules (MTs) in retracting protrusions in migrating dendritic cells leads to release of the RhoA guanine nucleotide exchange factor (GEF) Lfc (murine

homologue of GEF-H1), which in turn increases actomyosin contractility and retraction of the protrusion (Kopf et al. 2020). These findings suggest that the coordination of cell shape is a complex process involving the interplay of multiple signaling pathways and cytoskeletal components.

2.2.3 Guidance cues

In a physiological setting, it is critical for cells to not only coordinate their own shape but also to sense, process, and adapt to diverse guidance cues in their microenvironment (Shellard & Mayor 2020, SenGupta et al. 2021). These cues can be chemical, mechanical, or geometrical in nature (Charras & Sahai 2014, te Boekhorst et al. 2016, van Helvert et al. 2018). They induce a distinct cell polarity with a distinguishable cell front characterized by protrusion formation and a cell rear that is retracted (Ridley et al. 2003).

Probably most well investigated are chemical cues, such as diffusible chemicals (chemotaxis) or substrate-bound chemicals (haptotaxis). For example, in the case of leukocytes, the chemokines CCL19 and CCL21 - recognized by the CC-chemokine receptor 7 (CCR7) - guide dendritic cells to and within lymphatic vessels (Worbs et al. 2017). Dendritic cells show haptokinetic movement when encountering surface bound CCL21, which becomes directional when soluble CCL19 (chemotaxis) is present and even maintain collective migration by generating a soluble form of CCL21 along their path of migration (Schumann et al. 2010, Weber et al. 2013). Haptotaxis along immobilized CCL21 gradients strongly depends on chemokine concentration and steepness of the gradient, which has been shown to be optimal in *in vivo* settings guiding dendritic cells towards lymph vessels (Schwarz et al. 2017). Migration towards inflamed tissues is further dependent on ECM-bound adhesion receptors when leukocytes have to traverse the endothelial layer to reach sites of inflammation (Nourshargh & Alon 2014).

Depending on their life cycle phase, *Dictyostelium* cells follow the chemoattractants cAMP or folic acid. The life cycle of *Dictyostelium discoideum* comprises a vegetative reproduction phase in which the amoeba senses bacteria by folic acid (Pan et al. 1972) and an aggregation phase which is induced by starvation and mediated by cAMP (Konijn et al. 1967). Interestingly, *Dictyostelium* cells have been shown to navigate complex environments with the help of self-generated chemical gradients by locally degrading chemoattractant (Tweedy et al. 2020). Recently, it was found that dendritic cells modulate CCL19 gradients by internalizing CCR7-bound CCL19, thereby sustaining long-range collective dendritic cell migration and even guiding T cell migration (Alanko et al. 2023).

Simultaneously to chemical guidance cues, migrating cells can encounter mechanical signals, such as differently sized pores in the extracellular matrix (Wolf et al. 2013) or stiffness of the substrate that determines to which degree cells can deform (DuChez et al. 2019). The degree of confinement by the ECM differs according to the concentration of ECM components, which can in turn affect stiffness gradients or pore sizes within the microenvironment (Yamada & Sixt 2019). In order to deal with space restraints while migrating in dense tissue, cells develop diverse migration strategies. Active proteolytic remodeling of the ECM is a major feature of mesenchymal migrating cells (Wolf & Friedl 2011). Another mechanism described in invading cancer cells shows that stromal fibroblasts lead the way for carcinoma cells by forming tracks within the extracellular matrix (Gaggioli et al. 2007). Moreover, mechanical plasticity of the ECM has been shown to influence proteolysis-dependent and -independent migration modes in breast cancer cells (Wisdom et al. 2018). As amoeboid migrating cells are typically not proteolytically active (Wolf et al. 2003) and physiological pore sizes usually range from 2-10 μm (Wolf et al. 2009, Kameritsch & Renkawitz 2020), they rely on different mechanisms involving active pore widening (Pflücke & Sixt 2009, Barzilai et al. 2017) or pore size sensing to choose paths along larger pores (Renkawitz et al. 2019).

Finally, the geometry and topography of the microenvironment can make a substantial difference for migrating cells. For example, leukocytes migrating on a 2-dimensional (2D) surface employ an

adhesive crawling migration mode, where actin polymerization generates the force to push the plasma membrane at the cell front while adhesions to the substrate function as force transmitters (Lämmermann & Sixt 2009). In contrast, when migrating in a 3D environment, leukocytes switch to an adhesion-independent amoeboid migration mode (Yamada & Sixt 2019). Interestingly, leukocytes are even able to migrate in the total absence of adhesive forces by using topographical features of the microenvironment to move themselves forward (Reversat et al. 2020).

It is increasingly well understood how cells measure and respond to these specific guidance cues of either chemical or mechanical nature, but it remains unclear how migrating cells deal with and respond to diverse or even competing inputs. Another challenge arising from multiple competing guidance cues is certainly the coordination of complex cell shapes or protrusions along the selected path of migration.

2.3 Organelle positioning

Similarly to the coordination of multiple protrusions along the path of migration, the positioning of intracellular content and particularly organelles towards dominant protrusions presents a challenge for highly dynamic and motile cells. Cellular organelles are often positioned actively in a non-random manner to perform or support a specific function (Gundersen & Worman 2013, Renkawitz et al. 2019, Roman et al. 2021, Garde et al. 2022). In many cases, for example during cell division, organelle positioning requires a connection between the cellular organelle and the cytoskeleton (Lancaster et al. 2013, Knoblach & Rachubinski 2015, Moore et al. 2021). Moreover, membrane-less organelles, such as the centrosome itself can be positioned non-randomly in a region defined by the actomyosin network (Jimenez et al. 2021). Furthermore, biomolecular condensates can be actively positioned (Alberti & Hyman 2021) as shown for RNA granules that associate with lysosomes to be transported to distal regions in neurons (Liao et al. 2019).

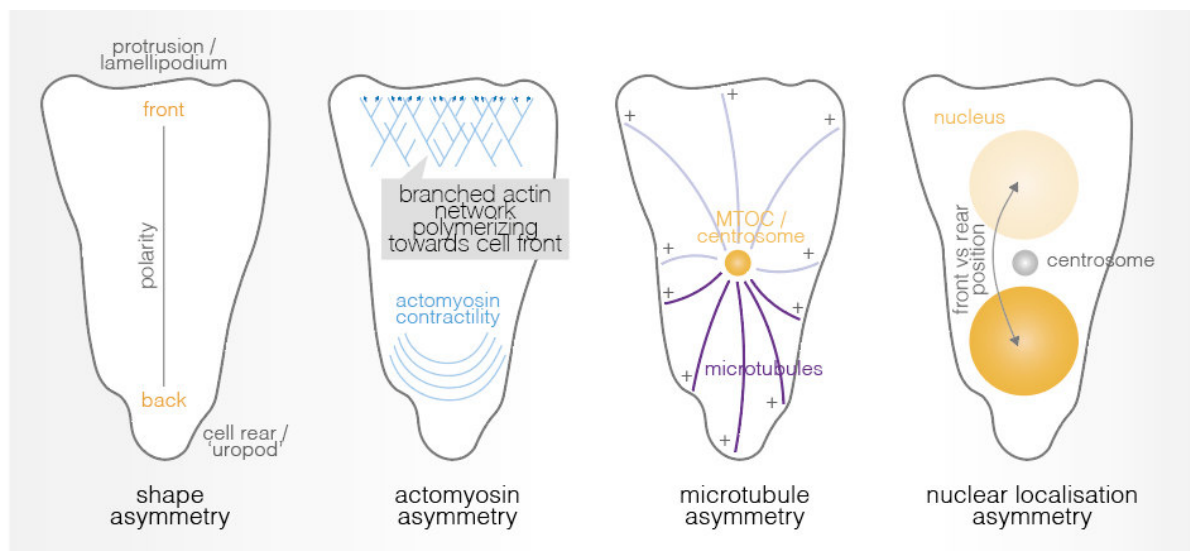


Figure 3: Asymmetry in motile cells. Motile cells show a distinct cell polarity with a cell front pushed forward by a branched actin network and actomyosin contractility at the back. The centrosome usually locates approximately to the cell center providing a reference for positioning of other cellular organelles, such as the differential localization of the nucleus in amoeboid and mesenchymal migrating cells. (Modified with permission from Kroll & Renkawitz, submitted review)

In many cells active positioning of cellular organelles leads to a defined cell polarity as described earlier for migrating cells with a distinguishable cell front and cell back (Figure 3) (Bornens 2008). This polarity often arises from an asymmetric distribution of cytoskeletal components, such as actin or microtubules, in which the actin cytoskeleton serves as the scaffold and the microtubule network as a stabilizer of polarity (Li & Gundersen 2008). Highly specialized and stably polarized along the apical-basal cell axis are for example epithelial cell layers that line organs, such as the intestine, lungs, or reproductive organs (Rodriguez-Boulan & Macara 2014). Notably, maintaining and adapting cell polarity becomes more challenging in fast moving cells that form highly dynamic and ramified cell shapes, need to respond to diverse or changing guidance cues, and thereby relocate large portions of their cytoplasm including cellular organelles (SenGupta et al. 2021).

2.3.1 Centrosome positioning

One of the main organelles that contributes to cell polarity is the centrosome which anchors microtubules and thereby functions as microtubule-organizing center (MTOC) (Bornens 2008). Microtubules themselves grow in a polarized manner with the minus end at the centrosome and the plus end extending towards the cell periphery (Akhmanova & Kapitein 2022). Additionally, microtubules form tracks for motor proteins, such as kinesins and dyneins that anchor and move organelles (Akhmanova & Kapitein 2022).

The centrosome normally locates approximately to the center of the cell, providing a reference for positioning of other cellular organelles (Bornens 2008). For example, the MTOC in fibroblasts is actively maintained at the cell center upon lysophosphatidic acid (LPA) treatment while the nucleus is translocated towards the cell rear (Gomes et al. 2005). Moreover, the position of the centrosome in the amoeba *Dictyostelium discoideum* is tightly regulated (Sameshima et al. 1988, Ueda et al. 1997, Odell et al. 2019). Notably, the positioning of the centrosome appears to be coupled to specific functions. During tumor cell migration the centrosome targets the distribution of the matrix metalloproteinase MT1-MMP storage endosomes towards the invadopodium facilitating proteolysis of the microenvironment (Infante et al. 2018). Furthermore, cytotoxic T lymphocytes position their centrosome close to the plasma membrane at the immunological synapse to deliver secretory granules (Stinchcombe et al. 2006). In migrating dendritic cells the centrosome even acts as a steering organelle inducing the retraction of “loosing” protrusions once it locates into the “winning” protrusion (Kopf et al. 2020), emphasizing the functional relevance of centrosome positioning in migrating cells.

2.3.2 Nuclear positioning

Tightly coupled to centrosome positioning is the position of the nucleus. As the largest and stiffest organelle in the cell body, the nucleus presents a particular challenge for the cell (Gundersen & Worman 2013, McGregor et al. 2016, Kalukula et al. 2022).

Especially during cell migration in 3D environments, nuclear stiffness determined by lamin A/C levels limits migration through tight constrictions (Davidson et al. 2014, Harada et al. 2014) and can even result in rupturing of the nucleus resulting in chromatin leaking into the cytoplasm, necessitating resealing of the nuclear envelope by components of the repair machinery ESCRT III (Denais et al. 2016, Raab et al. 2016). However, cells have developed mechanisms to sense and circumnavigate mechanical stress during migration (Lomakin et al. 2020, Venturini et al. 2020). Cell confinement below a specific threshold - defined by the ability of the nuclear envelope to stretch - increases actomyosin contractility via stretch-sensitive protein signaling (Lomakin et al. 2020, Venturini et al. 2020).

In addition to migration, nuclear positioning is also strictly regulated during proliferation or differentiation (Gundersen & Worman 2013, Bone & Starr 2016) and malfunctioning can lead to

dysfunction and diseases, such as muscular dystrophy, dilated cardiomyopathy, or (premature) aging (Zwerger et al. 2011). An important key player during nuclear positioning in many different cellular contexts is the LINC (linker of nucleoskeleton and cytoskeleton) complex (Figure 4) (Starr & Han 2002, Sosa et al. 2012). The LINC complex spans the inner and outer nuclear membrane and consists of outer nuclear membrane KASH (Klarsicht, ANC-1, and Syne homology) proteins and inner nuclear membrane SUN (Sad1 and Unc-84) proteins (Starr & Fridolfsson 2010, Sosa et al. 2012). The KASH proteins bind to different cytoskeletal components, thereby anchoring the nucleus to the cytoskeleton (Padmakumar et al. 2005, Crisp et al. 2006). Mutations in LINC complex proteins have been linked to multiple diseases (Kalukula et al. 2022) emphasizing the importance of nuclear positioning for cellular function. A very prominent and widely studied example of nuclear positioning mediated by the LINC complex is the rearward positioning of the nucleus in fibroblasts polarizing for migration (Gomes et al. 2005). The LINC complex components nesprin2G and SUN2 connect to dorsal actin cables forming so called TAN (transmembrane actin-associated nuclear) lines that move the nucleus along the retrograde actin flow (Luxton et al. 2010).

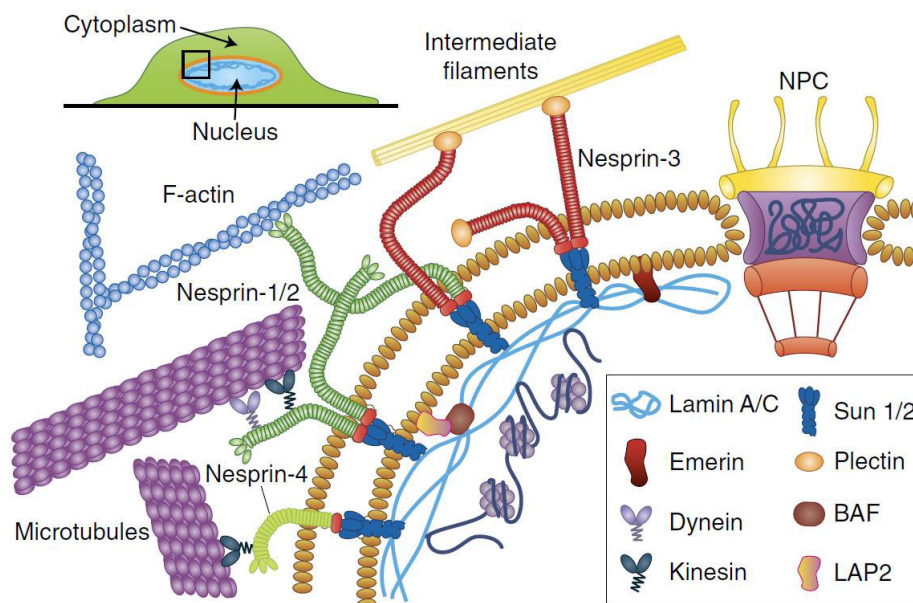


Figure 4: Schematic depiction of the LINC complex coupling the nucleus to the cytoskeleton. SUN proteins in the inner nuclear membrane and KASH proteins (nesprins) in the outer nuclear membrane form the LINC complex. Nesprins directly or indirectly (for example via motor proteins) link the nucleus to cytoskeletal components, such as microtubules, actin, or intermediate filaments. (From Kirby & Lammerding 2018, reproduced with permission from Springer Nature)

In addition, nuclear positioning can be mediated by microtubules, as shown for pronuclei in fertilized *Xenopus* eggs (Reinsch & Gönczy 1998). During development, proliferation in pseudostratified epithelia is linked to interkinetic nuclear migration (INM), in which the nucleus moves bidirectional along the basal-apical cell axis undergoing mitosis specifically at the apical side of the cell (Sauer 1935, Taverna & Huttner 2010). The cytoskeletal component driving INM varies strongly between different tissues (Tsai et al. 2007, Norden et al. 2009, Tsai et al. 2010). Nuclear positioning of multiple nuclei of fused myoblasts to the periphery of myofibers in skeletal muscles is driven by motor proteins along microtubule tracks (Metzger et al. 2012, Gache et al. 2017, Roman & Gomes 2018). Notably, muscle damage leads to myonuclei moving towards the damage site via microtubules and dynein to locally deliver messenger RNA for cellular repair (Roman et al. 2021).

Finally, cellular migration requires a defined front-rear polarity which is often dependent on nuclear positioning to specific cellular locations (Calero-Cuenca et al. 2018). For example, in migrating neurons the nucleus undergoes saltatory forward movement while following the leading centrosome (Solecki et al. 2004, Tsai et al. 2007, Solecki et al. 2009). Migration in interneurons is accompanied by actin localizing behind the nucleus and was shown to be myosin-dependent (Silva et al. 2018). In the context of amoeboid migration, it has been shown that these cells favor a nucleus forward positioning (Renkawitz et al. 2019), but it remains unclear how this configuration is achieved or maintained.

2.4 Aims

Amoeboid cells are fast migrating cells that are characterized by frequent and dynamic cell shape changes while they are navigating through microenvironments of heterogeneous composition (Lämmermann & Sixt 2009). The heterogeneity in the microenvironment provides diverse guidance cues for motile cells, such as chemokines or differently sized pores (SenGupta et al. 2021). These different cues are sensed by multiple explorative protrusions that undergo constant formation and retraction cycles. Many aspects of how motile amoeboid cells coordinate these multiple explorative protrusions have been identified (Lämmermann et al. 2009, Harada et al. 2012, Zhang et al. 2014, Kopf et al. 2020, Hadjithodorou et al. 2021, Hadjithodorou et al. 2023). But how amoeboid cells deal with locally competing guidance cues and how they organize their intracellular content including the large nucleus along the selected path of migration remains unknown.

To address this knowledge gap, I designed microenvironments of heterogeneous mechanochemical composition, such as microchannels, which provided the possibility to simultaneously measure chemical guidance by different chemokine concentrations and mechanical guidance by pore size decisions in a tightly controlled environment. I further employed 3-dimensional collagen matrices, that mimic the physiological surroundings of cells migrating in the interstitium. To uncover nuclear and centrosome positioning during amoeboid migration, I used leukocytes (dendritic cells and T cells) and the single cell amoeba *Dictyostelium discoideum* as models for fast migrating amoeboid cells. I used Hoxb8 cell lines with various fluorescent labels for the centrosome and nucleus, and *Dictyostelium* cells expressing GFP- α -tubulin as microtubule marker and mRFP-histone as marker for the centrosome (Bindl et al. 2020). To quantify the relative positioning of nucleus and centrosome as key cell polarity markers, I established manual analysis workflows as well as semi-automated analysis tools, which employed different image analysis software, such as Fiji (Schindelin et al. 2012), ilastik (Berg et al. 2019), and Imaris (Bitplane). To further elucidate the mechanism underlying nuclear positioning in migrating amoeboid cells, I used pharmacological inhibitors for different cytoskeletal components, such as nocodazole for microtubules, Latrunculin A for actin, and para-nitroblebbistatin (Képiró et al. 2014) for myosin-II. Additionally, I employed a mutant myosin-II-deficient *Dictyostelium* strain (Manstein et al. 1989), dendritic cells derived from bone marrow of MyoIIa-Flox*CD11c-Cre mice, and dendritic cells with a knockout for the myosin regulator Lfc (*Lfc*^{-/-}) (Kopf et al. 2020) to further decipher general principles and the mechanistic basis behind nuclear positioning.

3. Paper I: Adaptive Pathfinding by Nucleokinesis during Amoeboid Migration

Janina Kroll¹, Robert Hauschild², Artur Kuznetsov¹, Kasia Stefanowski¹, Monika D. Hermann¹, Jack Merrin², Lubuna Shafeek², Annette Müller-Taubenberger³, Jörg Renkawitz¹

¹ Biomedical Center Munich (BMC), Walter Brendel Center of Experimental Medicine, Institute of Cardiovascular Physiology and Pathophysiology, University Hospital, Ludwig Maximilians University Munich; Munich, Germany

² Institute of Science and Technology Austria; Klosterneuburg, Austria



³ Biomedical Center Munich (BMC), Department of Cell Biology (Anatomy III), Ludwig Maximilians University Munich; Munich, Germany

This article was published in The EMBO Journal 2023, e114557.

DOI: <https://doi.org/10.15252/emboj.2023114557>

I performed all experiments shown in Figure 2B, Figure 3A-C and 3F-H, Figure 4, Figure 5D-H, Figure 6, Figure EV2, Figure EV3, Figure EV4, Figure EV5 (supervision of the Latrunculin A titration experiments in Figure EV5A and B), Appendix Figure S1 (excluding the data in 3D collagen matrices in Appendix Figure S1), Appendix Figure S2, Appendix Figure S3, Appendix Figure S4, Appendix Figure S5, Appendix Figure S6, and Appendix Figure S7. I did the analysis for the data shown in Figure 2B, Figure 3E, Figure 4B-D, Figure 5E-H, Figure 6, Figure EV2, Figure EV4A-C, Figure EV5A-B (supervision) and EV5D-E, Appendix Figure S1 (excluding the data in 3D collagen matrices in Appendix Figure S1), Appendix Figure S2, Appendix Figure S4B-C, and Appendix Figure S6E-F. In addition, I performed the analysis in Figure 3B-C and 3G-H, Figure 4G-J, Figure EV3, Figure EV4D-G, Figure EV5C and EV5F-I, Appendix Figure S3, Appendix Figure S5, and Appendix Figure S6A-D in collaboration with RH (software). The workflow for the analysis of nucleokinesis in the blocked Y-channels is depicted in Appendix Figure S2, in which I performed the identification of nucleokinesis events, segmentation of the MTOC, and tracking of nucleus and MTOC. Furthermore, I designed the microchannels for pore size decision experiments (Figure 2A and Figure EV1A) and for path choices in competing chemokines and pore size gradients (Figure 2B-L, Figure 5A-C, and Figure EV1C-E). I wrote the Materials and Methods Section, Movie Legends, and parts of the Figure Legends. Additionally, I generated the movies, contributed to manuscript writing and creation of the figures.

Adaptive pathfinding by nucleokinesis during amoeboid migration

Janina Kroll¹ , Robert Hauschild², Artur Kuznetsov¹, Kasia Stefanowski¹, Monika D Hermann¹, Jack Merrin² , Lubuna Shafeek² , Annette Müller-Taubenberger³  & Jörg Renkawitz^{1,*} 

Abstract

Motile cells encounter microenvironments with locally heterogeneous mechanochemical composition. Individual compositional parameters, such as chemokines and extracellular matrix pore sizes, are well known to provide guidance cues for pathfinding. However, motile cells face diverse cues at the same time, raising the question of how they respond to multiple and potentially competing signals on their paths. Here, we reveal that amoeboid cells require nuclear repositioning, termed nucleokinesis, for adaptive pathfinding in heterogeneous mechanochemical microenvironments. Using mammalian immune cells and the amoeba *Dictyostelium discoideum*, we discover that frequent, rapid and long-distance nucleokinesis is a basic component of amoeboid pathfinding, enabling cells to reorientate quickly between locally competing cues. Amoeboid nucleokinesis comprises a two-step polarity switch and is driven by myosin-II forces that readjust the nuclear to the cellular path. Impaired nucleokinesis distorts path adaptations and causes cellular arrest in the microenvironment. Our findings establish that nucleokinesis is required for amoeboid cell navigation. Given that many immune cells, amoebae, and some cancer cells utilize an amoeboid migration strategy, these results suggest that nucleokinesis underlies cellular navigation during unicellular biology, immunity, and disease.

Keywords cell migration; cell polarity; mechanochemical cues; myosin; nuclear positioning

Subject Categories Cell Adhesion, Polarity & Cytoskeleton

DOI 10.15252/embj.2023114557 | Received 19 May 2023 | Revised 31 October 2023 | Accepted 3 November 2023

The EMBO Journal (2023) e114557

Introduction

The ability of cells to navigate their path while moving themselves forward is critical for innate and adaptive immune responses, organismal development, tissue maintenance, and single-cell organisms. During navigational migration, cells are surrounded by local

environments that are composed of extracellular matrix, interstitial fluid, and tissue cells in the case of cellular migration in multicellular organisms, or natural environments like soil in the case of motile single-cell organisms. To efficiently navigate through these environments, migrating cells are equipped with mechanisms to follow diverse chemical as well as mechanical cues (Charras & Sahai, 2014; Moreau *et al*, 2018; van Helvert *et al*, 2018; Yamada & Sixt, 2019). Most well investigated are chemotactic signals like chemokines, which are detected by the respective cellular receptors and align intracellular force generation by the actin cytoskeleton toward the chemotactic cue, such as during the recruitment of immune cells to sites of inflammation or into lymphatics (Nourshargh & Alon, 2014; Hauser *et al*, 2016; Worbs *et al*, 2017). Yet at the same time, motile cells also encounter mechanical guidance cues along their paths, such as differently sized pores in the extracellular matrix (Wolf *et al*, 2013; Renkawitz *et al*, 2019).

Navigating motile cells frequently generate new protrusions (“leading edges”; “cell fronts”) next to preexisting ones, followed by a preference for one of the protrusions, along which the path of migration is subsequently orientated. This morphological characteristic of multiple simultaneous protrusions is particularly common in shallow chemotactic gradients (Gerisch & Keller, 1981; Swanson & Taylor, 1982; Andrew & Insall, 2007; Kay *et al*, 2008), suggesting that cells employ these multiple protrusions to sense chemotactic cues at different micro-locations in their immediate surrounding. This notion is supported by the observation that deficiency of the Arp2/3 regulator Hem1 in motile immune cells not only reduces protrusion formation but also impairs migration along chemotactic gradients (Leithner *et al*, 2016). Collectively, these findings suggest that cells utilize alternative protrusions to simultaneously explore and measure guidance cues at different local sites in their immediate microenvironment. These explorative protrusions are most evident in fast-migrating amoeboid cells, such as neutrophils and dendritic cells, which adopt highly dynamic and ramified cell shapes (Fritz-Laylin *et al*, 2017; Driscoll *et al*, 2019; Renkawitz *et al*, 2019). While some principles of how migrating cells coordinate these complex cell shapes have been identified (Devreotes *et al*, 2017; Kopf *et al*, 2020; Hadjithodorou *et al*, 2021, 2023), it remains entirely unknown how motile cells deal with locally diverse and potentially

1 Biomedical Center Munich (BMC), Walter Brendel Center of Experimental Medicine, Institute of Cardiovascular Physiology and Pathophysiology, University Hospital, Ludwig Maximilians University Munich, Munich, Germany

2 Institute of Science and Technology Austria, Klosterneuburg, Austria

3 Biomedical Center Munich (BMC), Department of Cell Biology (Anatomy III), Ludwig Maximilians University Munich, Munich, Germany

*Corresponding author. Tel: + 49 089 2180 71516; E-mail: joerg.renkawitz@med.uni-muenchen.de

competing mechanochemical inputs, and how they reorganize their intracellular content along the dominant protrusion once a path has been selected.

Here, we address these open questions by investigating how amoeboid cells navigate their path in locally heterogeneous microenvironments. We identify thresholds at which chemical chemokine cues overrule mechanical pore size cues and vice versa. Furthermore, we reveal that protrusions extending through larger extracellular pores often contain the nucleus, necessitating rapid and large-distant intracellular repositioning of the nucleus, when the cell decides to follow a path defined by an emerging stronger chemotactic cue. Active intracellular relocation of the nucleus to specific intracellular locations is known to occur in various model systems, including neurons and multinuclear muscle cells (Gundersen & Worman, 2013), and has been termed “nucleokinesis.” Yet, how amoeboid migrating cells position their nucleus by nucleokinesis to align the nuclear path to the cellular path, despite their high shape dynamics, fast migration velocity, and unusual forward position of the nucleus in front of the MTOC (microtubule-organizing center), remained unknown. Here, we identify nucleokinesis during amoeboid migration, elucidate its mechanistic basis, and uncover its role in adaptive pathfinding within microenvironments characterized by competing chemical and physical cues.

Results

Rapid and long-distance nucleokinesis during amoeboid immune cell migration

As a model system for cell migration in microenvironments of heterogeneous mechanochemical composition, we imaged dendritic cells migrating along a chemotactic gradient (CCL19) while being embedded in a three-dimensional collagen matrix composed of varying pore sizes (Wolf *et al*, 2013; Schwarz *et al*, 2017; Driscoll *et al*, 2019; Renkawitz *et al*, 2019). Migrating dendritic cells frequently showed a ramified cell shape with multiple protrusions, continuously generating new protrusions next to existing ones and eventually favoring one protrusion to select the preferred path of migration (Fig 1A and B, and Movie EV1). In line with the function of the nucleus to act as a mechanical ruler to guide migration along the path of larger pore sizes (Renkawitz *et al*, 2019; Lomakin *et al*, 2020; Venturini *et al*, 2020), the cellular path was frequently identical with the nuclear path (Fig 1B). Yet, in one out of four path decisions we observed mispositioning of the nucleus into future ‘losing’ protrusions (Fig 1C and D). This deviation of the nuclear path from the cellular path caused a subsequent long-distance repositioning of the entire nucleus toward the winning protrusion, effectively realigning the nuclear with the cellular path (Movie EV1). Additionally, we also often observed repositioning of only parts of the nucleus, when the nucleus itself deformed simultaneously towards alternative cell protrusions, without entirely locating into these protrusions. In these situations, only the subnuclear part (nuclear protrusion) locating inside the “losing” protrusion had to be repositioned towards the “winning” protrusion along the selected cell path (Fig 1C and Movie EV1).

The intracellular repositioning of the entire nucleus relative to the cell body, also called nucleokinesis (Tsai & Gleeson, 2005;

Gundersen & Worman, 2013), was very rapid with velocities of 2–9 $\mu\text{m}/\text{min}$ (Fig 1F and Appendix Fig S1A) and displayed rapid accelerations faster than the movement of the cell body (Fig 1H). Nucleokinesis occurred approximately once per hour during DC migration within collagen matrices (Fig 1E) and over long intracellular distances of up to 45 μm (Fig 1G and Appendix Fig S1A–C). To test whether nucleokinesis is a general feature of amoeboid immune cell migration, we imaged T cells, which have a smaller and less-branched cytoplasmic cell body, and still detected frequent and rapid repositioning of the entire nucleus from “losing” into winning protrusions (Fig 1D–I and Movie EV3). These findings identify nucleokinesis as a novel component of amoeboid immune cell migration.

Nucleokinesis enables adaptive pathfinding in competing chemokine and pore size cues

As migrating cells encounter chemical (e.g., chemokine gradients) as well as mechanical (e.g., varying pore sizes) cues at the same time (Moreau *et al*, 2018; Yamada & Sixt, 2019; Kameritsch & Renkawitz, 2020), our observations suggested that cells may use nucleokinesis to flexibly adapt their path between locally competing guidance cues. To functionally test this hypothesis, we engineered reductionistic cellular path decision points, at which migrating cells encounter two path options with different strengths of chemotactic as well as pore size cues. To provide diverse pore size cues, we generated two differently sized pores at the path junction, with pore sizes ranging from 8 to 2 μm width. According to the previously described mechanism for sensing pore sizes (Renkawitz *et al*, 2019), migrating cells did not differentiate between large 8 and 6 μm pores but when choosing between a small pore (2 or 4 μm) and a large 8 μm pore (Figs 2A and EV1A). Next, to test whether we can selectively guide cells towards a specific path based on a stronger chemokine cue, we engineered one path to be closer to the source of the chemokine than the alternative path, which follows a snake-like pattern and thus is more distant to the chemokine source (Fig 2B). Simulation of the diffusion of the chemotactic gradient over time showed that the snake-like path indeed causes higher chemokine concentrations at the path junction towards the path closer to the chemokine source (Fig EV1B). We confirmed these results experimentally by visualizing the chemotactic gradient by using fluorescent 10 kDa dextran as a proxy for the chemokine CCL19, showing stably higher concentrations over time at the path junction towards the path closer to the chemokine source and lower concentrations towards the path more distant to the chemokine source (Fig 2B).

Next, we investigated cellular decisions upon offering both chemokine and mechanical cues simultaneously at single path junctions (Fig 2C–E). When both paths were composed of almost equally sized large pores at their entrances, exceeding the threshold of the nuclear pore size sensing mechanism, cells showed a strong preference for the path closer to the chemokine source (Fig 2C and F, and Movie EV2). Yet, when we gradually narrowed the entrance pore of chemokine-proximal path, cells increasingly favored the alternative path, which was more distant to the chemokine source but had a larger pore at the path entrance (Fig 2C–H and Movie EV2). In contrast, in the absence of a chemokine source, cells always preferentially selected the longer paths with wider pores (Fig EV1C–E). Thus, these findings reveal that chemokine and pore

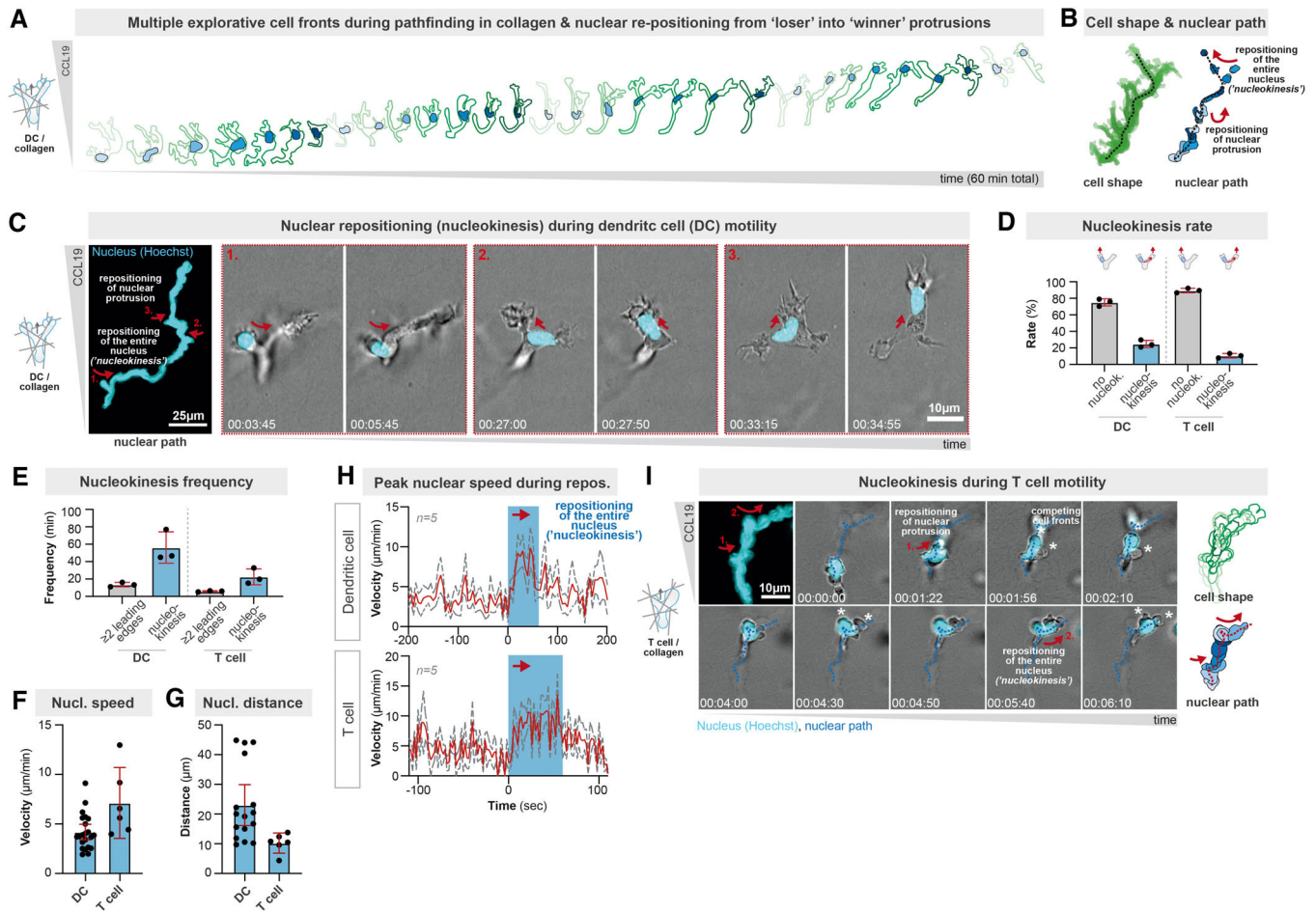


Figure 1. Immune cells employ rapid and long-distance nucleokinesis during amoeboid cell migration.

- A** Cellular outlines (shades of green, time color-coded) of a representative bone marrow-derived mouse dendritic cell (DC) migrating in a three-dimensional collagen matrix along a CCL19 chemokine gradient. The intracellular localization of the DC nucleus during pathfinding is shown in blue (shades of blue, time color-coded). See also Movie EV1.
- B** Projection cellular (green) and nuclear (blue) path of the cell in (A) over 60 min time. Note the two events, in which either only parts of the nucleus (nuclear protrusions) or the entire nucleus deviate from the cellular path, the later requiring full intracellular nuclear repositioning (called "nucleokinesis").
- C** Representative nucleokinesis events in a bone marrow-derived DC migrating through a three-dimensional collagen matrix along a CCL19 chemokine gradient. Highlights in dashed boxes show events of repositioning of the entire nucleus (1., "nucleokinesis") or parts of the nucleus (2. & 3., "nuclear protrusions"). Time in h:min:s.
- D** Quantification of the rate of nucleokinesis events in amoeboid DCs and T cells migrating in a collagen matrix: when the migrating cell has at least two major protrusions, quantification of whether the nucleus locates immediately into the dominant protrusion or first locates into the future retracting protrusion, requiring nucleokinesis into the future dominant protrusion. Data are mean \pm SD. $N = 31$ DCs (3 replicates, 135 events) and 30 T cells (3 replicates, 100 events).
- E** Quantification of how often (frequency) DCs and T cells have multiple simultaneous protrusions and how often they show nucleokinesis events in a collagen matrix: as in (D), but showing the frequency of at least two clearly observable leading edges and nucleokinesis events per minute. Data are mean \pm SD. $N = 31$ DCs (3 replicates, 135 events) and 30 T cells (3 replicates, 100 events).
- F** Quantification of the speed of nuclear movement during full nucleokinesis in DCs and T cells. $N = 16$ DCs (3 replicates), 6 T cells (3 replicates). Data are median \pm 95CI.
- G** Quantification of the intracellular distance of nuclear movement during full nucleokinesis in DCs and T cells. $N = 16$ DCs (3 replicates), 6 T cells (3 replicates). Data are median \pm 95CI.
- H** Measurements of nuclear speed before, during, and after full nucleokinesis events in DCs and T cells. The blue box marks the nucleokinesis event. Data are mean \pm SEM (the mean is shown as a red line and the SEM is shown as dashed gray lines). $N = 5$ cells.
- I** Representative nucleokinesis events in a T cell migrating through a three-dimensional collagen matrix along a CCL19 chemokine gradient. Red arrows highlight events of repositioning of the parts of the nucleus (1., "nuclear protrusions") or the entire nucleus (2., "nucleokinesis"). Time projections of the cellular and nuclear paths are shown in shades of green and blue, respectively. Time in h:min:s.

Source data are available online for this figure.

size cues are competitive and identify thresholds at which chemokine cues overrule pore size cues and vice versa.

To test for the functional relevance of nucleokinesis, we imaged the spatiotemporal dynamics of nuclear behavior during these path decisions. While the nucleus was often immediately positioned in

the future winning protrusion, we also observed frequent nucleokinesis events in which the nucleus was mispositioned far-distantly into the future “wrong” path, necessitating long-distance nucleokinesis to the “winning” protrusion (Fig 2I–L and Movie EV2). Notably, nucleokinesis occurred particularly frequently when the nucleus

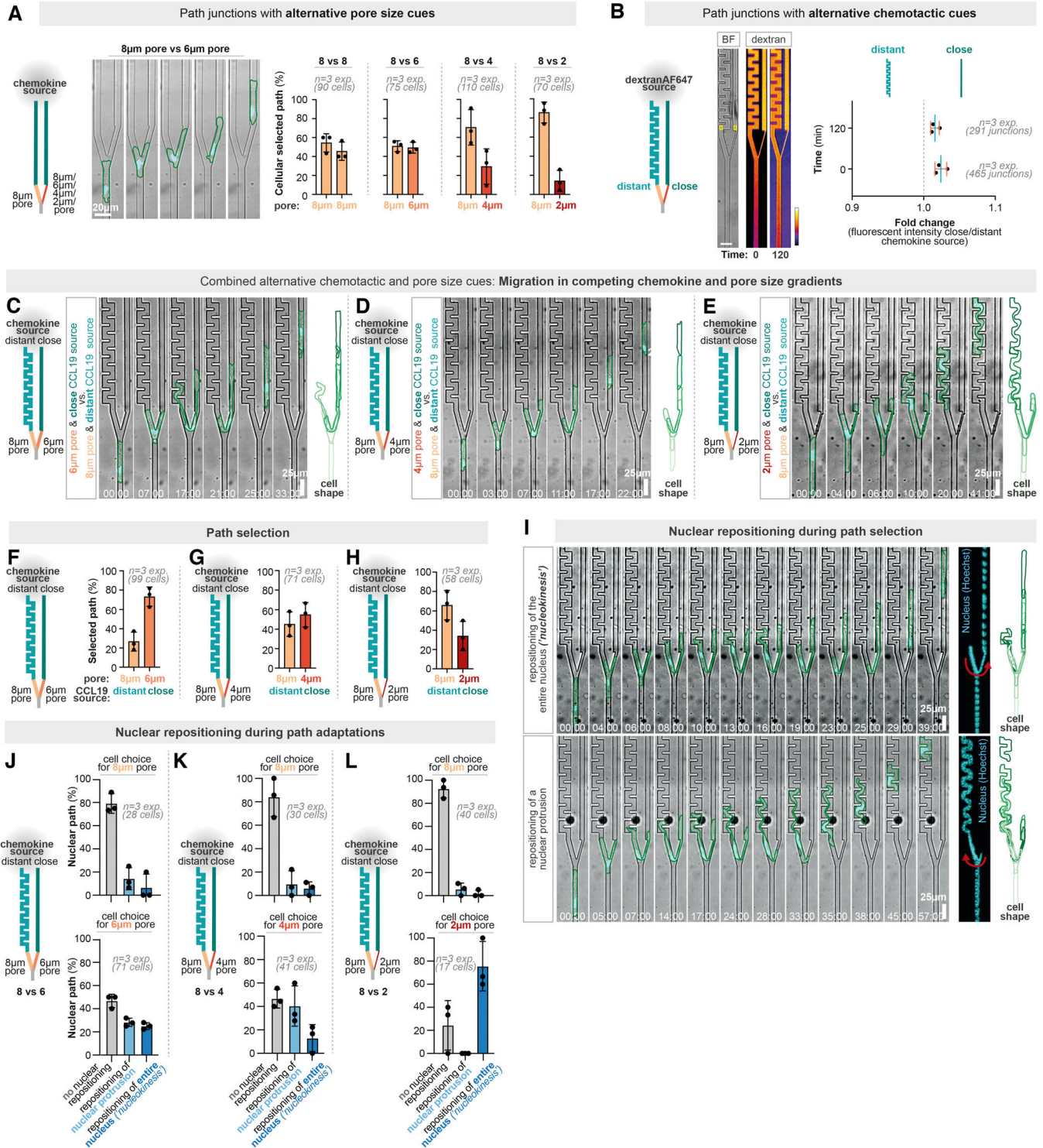


Figure 2.

Figure 2. Nucleokinesis enables adaptive pathfinding in competing chemokine and pore size cues.

- A Left: Representative bone marrow-derived DCs (BMDC) migrating in microchannels with two-way path junctions with different pores but an equally long and symmetric path towards the chemokine source sizes (8 vs. 6 μm shown here; representative examples for 8 vs. 8, 8 vs. 4, or 8 vs. 2 μm are shown in Fig EV1A). The cell shape is outlined in green and the nucleus is visualized by Hoechst (cyan). Right: quantification of cellular path decisions. $N = 3$ replicates (90 cells for 8 vs. 8 μm decisions; 75 cells for 8 vs. 6 μm decisions; 110 cells for 8 vs. 4 μm decisions; 70 cells for 8 vs. 2 μm decisions). Data are Mean \pm SD.
- B Visualization and quantification of 10 kDa dextran-AF647 gradients as a proxy for the similarly sized chemokine CCL19. DextranAF647 (fire-color coded) was added with CCL19 to the loading source hole and its diffusion was visualized by fluorescent microscopy over time. The experiment was performed in the presence of bone-marrow-derived DCs (BMDCs). The yellow rectangles mark the area of quantitative measurements of dextranAF647 concentrations. $N = 3$ replicates (465 and 291 junctions at timepoints 0 and 120, respectively). Timepoint 0 represent the timepoint when the cells started to migrate into PDMS devices. Data are Mean \pm SD.
- C Representative bone marrow-derived dendritic cell (DC) approaching a path junction with two alternative path options and competing chemokine and pore size cues: the left path has an 8- μm wide pore, but is more distantly located to the CCL19 chemokine source. The right path has a 6- μm wide pore and is more closely located to the CCL19 chemokine source. The cell shape is outlined in green and the nucleus is visualized by Hoechst (cyan). Time in min:s.
- D As in (C), but the right path that is closer to the chemokine source has a pore size of only 4 μm .
- E As in (C), but the right path that is closer to the chemokine source has a pore size of only 2 μm .
- F Quantification of cellular path decisions in the microenvironments shown in (C). See also Fig EV1C for controls without a chemokine source. Data are Mean \pm SD. $N = 3$ replicates (99 cells).
- G Quantification of cellular path decisions in the microenvironments shown in (D). See also Fig EV1D for controls without a chemokine source. Data are Mean \pm SD. $N = 3$ replicates (71 cells).
- H Quantification of cellular path decisions in the microenvironments shown in (E). See also Fig EV1E for controls without a chemokine source. Data are Mean \pm SD. $N = 3$ replicates (58 cells).
- I Representative full and partial nucleokinesis events during cellular path decisions in the competing chemokine and pore sizes cues. The cell shape is outlined in green and the nucleus is visualized by Hoechst (cyan). Time in min:s.
- J Quantification of nucleokinesis events in the microenvironments shown in (C), depending on whether the cell finally decides for the larger 8- μm or smaller 6- μm pore. Data are Mean \pm SD. $N = 3$ replicates (40 cells or 17 cells with the final decision either for 8- or 6- μm pore, respectively).
- K Quantification of nucleokinesis events in the microenvironments shown in (D), depending on whether the cell finally decides for the larger 8- μm or smaller 4- μm pore. Data are Mean \pm SD. $N = 3$ replicates (30 cells or 41 cells with the final decision either for 8- or 4- μm pore, respectively).
- L Quantification of nucleokinesis events in the microenvironments shown in (E), depending on whether the cell finally decides for the larger 8- μm or smaller 2- μm pore. Data are Mean \pm SD. $N = 3$ replicates (28 cells or 71 cells with the final decision either for 8- or 2- μm pore, respectively).

Source data are available online for this figure.

was initially positioned into the path bearing a larger pore entrance, but the cell selected the alternative path with a narrow pore entrance with a stronger chemotactic cue (Fig 2J–L). These findings show that cells can overcome the nuclear pore size sensing mechanism by chemotactic inputs and that nucleokinesis is required to adapt the nuclear path to the cellular path along an appearing dominating cue. Thus, nucleokinesis enables adaptive pathfinding during amoeboid cell navigation to flexibly navigate along locally competing mechanochemical guidance cues.

Two-step amoeboid nucleokinesis by consecutive cell polarity switches

It is well established that cytoskeletal forces are able to intracellularly move and position the nucleus in diverse cell types such as neurons, glial cells, muscle cells, and fibroblasts (Gundersen & Worman, 2013; Cadot *et al.*, 2015; Calero-Cuenca *et al.*, 2018). Plotting the speed and distance of nucleokinesis in these cell types in comparison to the here measured parameters revealed an extraordinary efficiency of nucleokinesis in immune cells, being rapid as well as far distant (Appendix Fig S1A). Notably, the intracellular behavior of the immune cell's nucleus was reminiscent of the amoeboid's cell body behavior, meaning that the nucleus moved rapidly, flexibly, and with continuous shape changes (e.g., Fig 1C and Movie EV1). As these parameters are hallmarks of amoeboid cell behavior, we propose to name nucleokinesis in amoeboid cells as "amoeboid nucleokinesis".

To unravel the mechanistic basis of amoeboid nucleokinesis, we next imaged the spatiotemporal dynamics of the centrosome-to-nucleus axis, an important indicator of cell polarity and cytoskeletal forces acting on the nucleus during nuclear movement (Luxton &

Gundersen, 2011). To uncouple nucleokinesis from effects caused by cellular squeezing, we established novel path junctions with equally large pore sizes but one blocked path, causing nucleokinesis events from the blocked to the open path (Fig 3A, Appendix Fig S2A–D, and Movie EV3). Using EB3-mCherry expressing DCs as a marker for the centrosome (also called microtubule-organizing center (MTOC)) and semi-automated imaging analysis (Appendix Fig S2E), we observed two rapid polarity switches in the nucleus-MTOC axis configuration during amoeboid nucleokinesis (Fig 3A and Movie EV3): while DCs migrated with a typical amoeboid nucleus-forward configuration (Renkawitz *et al.*, 2019) before nucleokinesis (Fig 3A–C), the repositioning of the nucleus from the "losing" into the "winning" protrusion coincided with a switch in the nucleus-MTOC axis configuration as the cells moved with the MTOC in front of the nucleus during the first phase of nucleokinesis (Fig 3A–C). When the DCs continued their path of migration after the first phase of nucleokinesis, the nucleus passed again the MTOC to restore the initial nucleus-MTOC axis configuration (Fig 3A–C), showing that the nucleus does not passively stay at the cell rear upon the retraction of the nucleus-containing "losing" protrusion, but actively repositions to its original location forward of the MTOC during the second phase of nucleokinesis (Fig EV2A). Together, these data show that nucleokinesis in migrating amoeboid cells is composed of two phases: in the first phase of nucleokinesis, the nucleus travels intracellularly from the "losing" into the "winning" protrusion. In the second phase of nucleokinesis, the nucleus travels from the rear of the MTOC to the front of the MTOC.

To corroborate these findings, we used the microtubule markers EMTB-mCherry and Spy-tubulin as additional MTOC markers (Fig EV2B and C), as well as manual mapping of the MTOC-to-nucleus axis during nucleokinesis (Fig EV2D–F), confirming both

observed rapid polarity switches (Appendix Fig S3A–F) during the first and second phases of amoeboid nucleokinesis. Similarly, when we investigated the MTOC-to-nucleus axis during DC pathfinding in deformable collagen networks, we observed preferential MTOC-forward configuration during the first phase of nucleokinesis, followed by the restoration of the nucleus-forward configuration during the second phase of nucleokinesis (Fig 3D and E). Together, these findings identify that amoeboid nucleokinesis is characterized by two rapid polarity switches in the MTOC-to-nucleus axis.

Myosin-based forces drive amoeboid nucleokinesis to ensure adaptive pathfinding

When we measured the lengths of “losing” protrusions at path junctions, we observed that “losing” protrusion containing the nucleus were longer (Fig 4A and B) and required more time to retract (Fig 4A and C) compared to those without a nucleus, suggesting that retraction of protrusions containing the nucleus is a particular challenge (Fig 4D). This raised the question of which forces drive nuclear repositioning during amoeboid nucleokinesis. The positioning of the MTOC in front of the nucleus during the first phase of nucleokinesis suggested the possibility that microtubules emanating from the MTOC may couple to the nucleus, and thereby exert forces on the nucleus to pull it from the “losing” protrusion back to the cellular path. Yet surprisingly, when we depolymerized microtubules (Appendix Fig S4A–C), we did not observe any slowdown of amoeboid nucleokinesis (Figs 3F and EV3A–F, and Movie EV4). In contrast, nocodazole-treated cells showed, if at all, rather an accelerated speed of nucleokinesis (Fig EV3A and B) as well as repositioning frontward to the MTOC (Fig 3G and H). As microtubule depolymerization is known to cause increased cellular contractility by releasing microtubule-bound actomyosin regulators like the RhoA guanine nucleotide exchange factor GEF-H1/Lfc1 (Krendel et al, 2002; Bouchet & Akhmanova, 2017; Kopf et al, 2020), this finding raised the possibility that actomyosin contractility could be a driving force of amoeboid nucleokinesis. This notion was supported when we quantified the distance as well as the change of distance between the nucleus and the MTOC (Appendix Fig S3C–F), showing that the nucleus is even more distantly frontward positioned upon microtubule inhibition (Fig EV3E–G), as if the nucleus would be pushed to a frontward localization while the localization of the MTOC remains rather stable along the cell axis. Further, imaging of myosin-IIA localization during amoeboid nucleokinesis using MYH9-GFP encoding dendritic cells revealed an enriched myosin-IIA localization in retracting protrusions closely behind the nucleus (Fig 4E and F, and Movie EV5). Similarly, when we imaged the localization of actin (Lifeact-GFP) and myosin (MYH9-GFP) in the environments with one blocked path that allow the specific observations of nucleokinesis, we observed relocalisation of myosin from the previous cell rear toward the back of the nucleus-containing “losing” protrusion (Fig 4G), as if myosin forces would drive nucleokinesis.

To test whether myosin-IIA indeed provides forces to reposition the nucleus during amoeboid nucleokinesis, we next exposed motile DCs to the myosin-II inhibitor para-nitroblebbistatin (Képiró et al, 2014) (Fig EV4A and B). Cells with inhibited myosin failed to efficiently switch cell polarities during nucleokinesis, showing a random nucleus-to-MTOC axis configuration before, during, and after

nucleokinesis (Figs 4H and I, and EV4C–G, and Movie EV6). To corroborate these results, we analyzed myosin-IIA knockout DCs and also observed delayed reconfiguration of the nucleus-to-MTOC axis during amoeboid nucleokinesis (Appendix Fig S5A–D). Given the concerted action of myosin together with the actin cytoskeleton, we next inhibited the actin cytoskeleton with low-doses of latrunculin, which still enabled migration (Fig EV5A and B) but reduced the rate of cell polarity switching during nuclear repositioning (Figs 4J and EV5C–I). Thus, actomyosin contractility is required for efficient cell polarity switching during amoeboid nucleokinesis.

To test for the functional consequences of impaired amoeboid nucleokinesis, we next measured the speed of nucleokinesis and cellular path adaptations when myosin is nonfunctional. While the cellular speed before nucleokinesis was even mildly increased in the presence of the myosin-II inhibitor para-nitroblebbistatin (Fig EV4E), path adaptations in response to competing chemical and mechanical guidance cues occurred less rapidly (Fig 5A and B) and less frequently (Fig 5C). Notably, “losing” protrusions containing the nucleus were more affected by myosin inhibition than “losing” protrusions without a nucleus (Fig 5B), suggesting that myosin forces are not only required for protrusion retraction but are also particularly required when the protrusion contains a mispositioned nucleus. Similarly, when we analyzed path adaptations in environments completely independent of pore sizes, the repositioning of the nucleus from “dead”-end paths to the selected cellular paths was slowed down upon myosin (Figs 5D, E and G, and EV4D and E) and actin inhibition (Fig EV5E–G), causing a longer duration of nucleokinesis (Fig 5G) and even entire failure to adapt the nucleus to the cellular path, resulting in cells stuck in the wrong path (Fig 5H and Movie EV6). Quantification of the retraction time of “losing” protrusions with and without nucleus showed again that nucleus-containing protrusions are particularly susceptible for myosin inhibition (Fig 5E). To confirm these findings, we employed DCs with a knockout of the myosin regulator GEF-H1 (Lfc in mouse) and found a reduction in the retraction time of nucleus-containing “losing” protrusions, but not in the retraction time of “losing protrusions” without a nucleus and also not during migration in straight channels (Fig 5F and Appendix Fig S6A–F). Together, these findings identify actomyosin forces as a major driving factor of amoeboid nucleokinesis.

Adaptive pathfinding by nucleokinesis in the *Dictyostelium discoideum* amoebae

To explore whether adaptive pathfinding by amoeboid nucleokinesis is a general feature of amoeboid cell migration, we investigated motile single cells of the amoebae *Dictyostelium discoideum*. Comparable to immune cells, *Dictyostelium* cells typically explore their surrounding microenvironment with at least two protrusions (Andrew & Insall, 2007), until they select a path, followed by repeated cycles of protrusion formation, path exploration, and path selection (Fig 6A and Movie EV7). Using a nuclear marker during *Dictyostelium* pathfinding in an environmental maze along a chemotactic folate gradient, we discovered frequent nucleokinesis events from future “losing” into “winning” protrusions (Fig 6A and E), with rapid speeds faster than the cell front (Fig 6B) in the range of 8 to 25 $\mu\text{m}/\text{min}$ (Fig 6C). Given the smaller cell body of *Dictyostelium* cells in comparison to DCs, the nucleokinesis distances of 10 μm

represented far-distant intracellular nuclear re-positioning throughout the cell body (Fig 6D). Thus, the basic parameters of nucleokinesis in *Dictyostelium* cells are highly comparable to nucleokinesis in immune cells (Fig 6C–E, and Appendix Fig S1A–C and Movie EV7). Next, to characterize the configuration of the nucleus-MTOC axis, we employed *Dictyostelium* cells encoding mRFP-histone as a marker for the nucleus and GFP- α -tubulin as a marker for the MTOC

(Fig 6F). Before a nucleokinesis event, *Dictyostelium* cells migrated in the typical amoeboid nucleus-forward configuration (Ishikawa-Ankerhold et al, 2022), but then switched to an MTOC-forward configuration during the first phase of nucleokinesis, followed by the restoration of the nucleus-forward configuration during the second phase (Fig 6F–H and Movie EV8). Notably, as in amoeboid immune cells, this two-step polarity switch is dependent on myosin-II

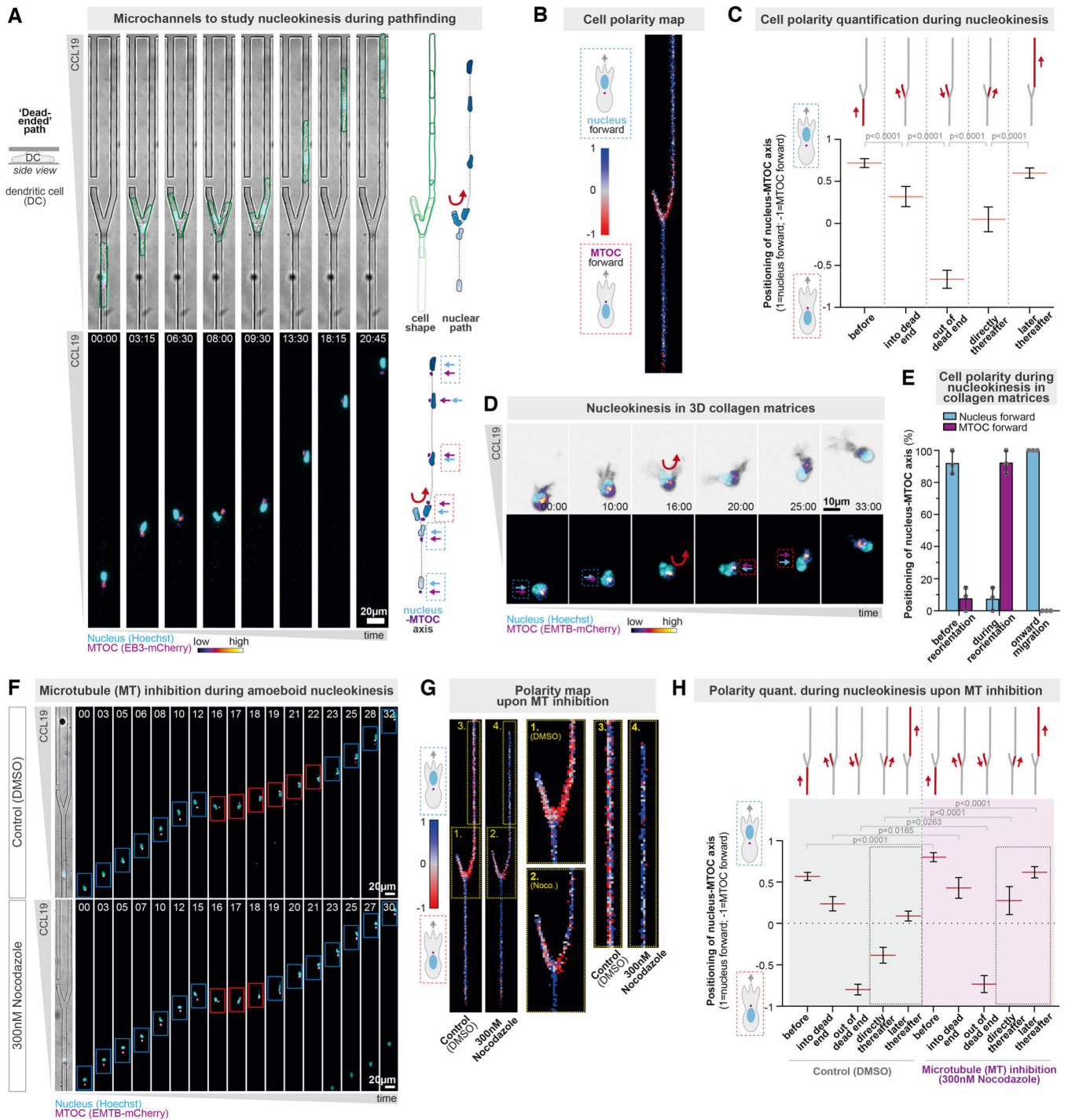


Figure 3.

Figure 3. Two-step amoeboid nucleokinesis by consecutive cell polarity switches.

- A Representative Hoxb8-derived dendritic cell (DC) approaching a path decision with equal pore sizes but one blocked path, frequently causing nucleokinesis from the blocked to the open path. The DC stably encodes the microtubule plus-end marker EB3-mCherry, which also visualizes the microtubule-organizing center (MTOC; in pink). The nucleus is visualized by Hoechst (cyan) and the cell shape is outlined in green. Projections of cellular (green), MTOC (pink) and nuclear (blue) paths are shown on the right. The configuration of the nucleus-MTOC axis is highlighted by dashed boxes (blue = nucleus forward; red = MTOC forward). See also Fig EV1D–G for a detailed characterization of the assay. Time in min:s.
- B Heatmap of the nucleus-MTOC axis configuration during amoeboid nucleokinesis. The frontward positioning of the nucleus is depicted in blue and the frontward positioning of the MTOC is depicted in red. See also Fig EV1H for a more detailed description of the imaging quantification. $N = 6$ replicates, 48 cells.
- C Quantification of the nucleus-MTOC axis configuration before, during, directly after, and later after amoeboid nucleokinesis (1 = all cells position the nucleus in front of the MTOC; -1 = all cells position the MTOC in front of the nucleus). Data are mean \pm 95CI, Mann–Whitney test, $N = 6$ replicates, 48 cells, and 660 (before), 250 (into a dead end), 191 (out of a dead end), 179 (directly thereafter), and 678 (later thereafter) image frames.
- D Representative HoxB8-derived DCs stably encoding EMTB-mCherry (visualizes the MTOC; fire-color coded) and transiently stained with Hoechst (visualizes the nucleus; cyan), migrating in a three-dimensional collagen network along a CCL19 chemokine gradient. The cell shape is shown in black (via high intensity of the EMTB-mCherry channel). Note the nucleokinesis event from the left protrusion into the right protrusion. Time in min:s.
- E Quantification of the nucleus-MTOC axis configuration of DCs (stably encoding EB3-mCherry to visualize the MTOC) migrating in 3D collagen networks and performing nucleokinesis. The nucleus-MTOC axis configuration was analyzed before, during, and after the nucleokinesis event. Data are mean \pm SD. $N = 3$ replicates, 32 cells.
- F Representative HoxB8-derived DCs in the presence of the microtubule inhibitor nocodazole (300 nM) or control (DMSO). The DCs stably encode EMTB-mCherry (to visualize the MTOC; fire-color coded) and is transiently stained with Hoechst (to visualize the nucleus; cyan). The configuration of the nucleus-MTOC axis is highlighted by boxes (blue = nucleus forward; red = MTOC forward). Time in min.
- G Heatmap of the nucleus-MTOC axis configuration during amoeboid nucleokinesis in the presence of the microtubule inhibitor nocodazole (300 nM) or control (DMSO). The yellow-dotted regions 1 (DMSO) and 2 (Nocodazole) are enlarged to depict the cellular behavior during the initial nucleokinesis event, and the yellow-dotted regions 3 (DMSO) and 4 (Nocodazole) are enlarged to depict the cellular behavior during the later nucleokinesis events to reposition the nucleus to the cellular front. $N = 3$ replicates, 96 (DMSO) and 36 (Nocodazole) cells.
- H Quantification of the nucleus-MTOC axis configuration before, during, directly after, and later after amoeboid nucleokinesis in the presence of the microtubule inhibitor nocodazole (300 nM) or control (DMSO) (1 = all cells position the nucleus in front of the MTOC; -1 = all cells position the MTOC in front of the nucleus). Data are mean \pm 95CI, Mann–Whitney test, $N = 3$ replicates, 96 (DMSO) and 36 (Nocodazole) cells, and 1,096 (before; DMSO), 463 (before; nocodazole), 493 (into a dead end, DMSO), 203 (into a dead end, nocodazole), 338 (out of a dead end, DMSO), 172 (out of a dead end, nocodazole), 360 (directly thereafter, DMSO), 127 (directly thereafter, nocodazole), 1,062 (later thereafter, DMSO), and 508 (later thereafter, nocodazole) image frames.

Source data are available online for this figure.

contractility, as the positioning of the nucleus to the front of the cell axis was strongly delayed in the presence of the myosin-II inhibitor para-nitroblebbistatin (Fig 6I, and Appendix Fig S7A and B, and Movie EV9). To corroborate these results, we analyzed *Dictyostelium* cells bearing a well-established myosin-II null mutation (myosin-II deficient (mhcA-null) strain HS2205) (Manstein *et al*, 1989; Bindl *et al*, 2020), as well as genetically encoded markers for the nucleus and the MTOC (mRFP-histone and GFP- α -tubulin), and also observed delayed nuclear relocalization frontward to the MTOC during nucleokinesis (Fig 6J and K, and Movie EV9). Thus, despite the phylogenetic distance between mammalian immune cells and the amoebae *D. discoideum*, the mechanistic principles of amoeboid nucleokinesis during cellular navigation are conserved.

Together, these findings identify amoeboid nucleokinesis as a conserved process in rapid amoeboid migrating cells, comprising a two-step cell polarity switch driven by myosin-II forces, sliding the nucleus from a “losing” to the “winning” protrusion to ensure adaptive pathfinding in complex microenvironments.

Discussion

Cellular organelles are often actively positioned to defined subcellular locations within the cytoplasm (Bornens, 2008). This active positioning includes membrane-surrounded organelles like the nucleus and mitochondria, but also membraneless-organelles like the microtubule-organizing center (MTOC). The active positioning of the genome-carrying nucleus is particularly challenging (Gundersen & Worman, 2013), as it is typically the largest and stiffest organelle (Kalukula *et al*, 2022). Cells solved this challenge by exerting forces

from the cytoskeleton onto the nucleus, leading to its intracellular movement and positioning—a process referred to as nucleokinesis, by which the entire nucleus moves intracellularly in relation to the cell’s shape. For instance, cells in the developing vertebrate neuroepithelium employ forces that are mainly generated by the actomyosin cytoskeleton to move their nuclei basally and apically during the progression of the cell cycle (Norden *et al*, 2009), whereas the movements of female and male pronuclei during fertilization are mainly driven by forces from the microtubule cytoskeleton (Reinsch & Gonczy, 1998).

An additional complexity for nuclear positioning arises when cells are not stationary but motile (Calero-Cuenca *et al*, 2018), adding the challenge of coordinating nuclear positioning with the cellular advance along the migratory path. Key findings showed that motile fibroblasts reposition their nucleus to the cellular rear to start their movement into cell-free tissue wounds (Luxton *et al*, 2010; Zhu *et al*, 2018). Mechanistically, this rearward nuclear positioning is driven by an actin cortex composed of actin cables that are coupled to the nucleus and move against the direction of cellular movement (Luxton *et al*, 2010). Fibroblasts are mesenchymally migrating cells that adhere to their extracellular environments and migrate with velocities in the range of tens of micrometers per hour. Thus, the principles and mechanisms of nuclear positioning in stationary and slowly moving cells are increasingly well understood. However, how extremely fast migrating cells coordinate the intracellular positioning of the nucleus with their migration path remained entirely unknown. The high velocities of fast migrating cells, which are typically around 10 $\mu\text{m}/\text{min}$, even raised the question of whether nuclear movement can be at all faster than the cellular speed—a prerequisite for active nuclear repositioning in relation to the movement of the cell body.

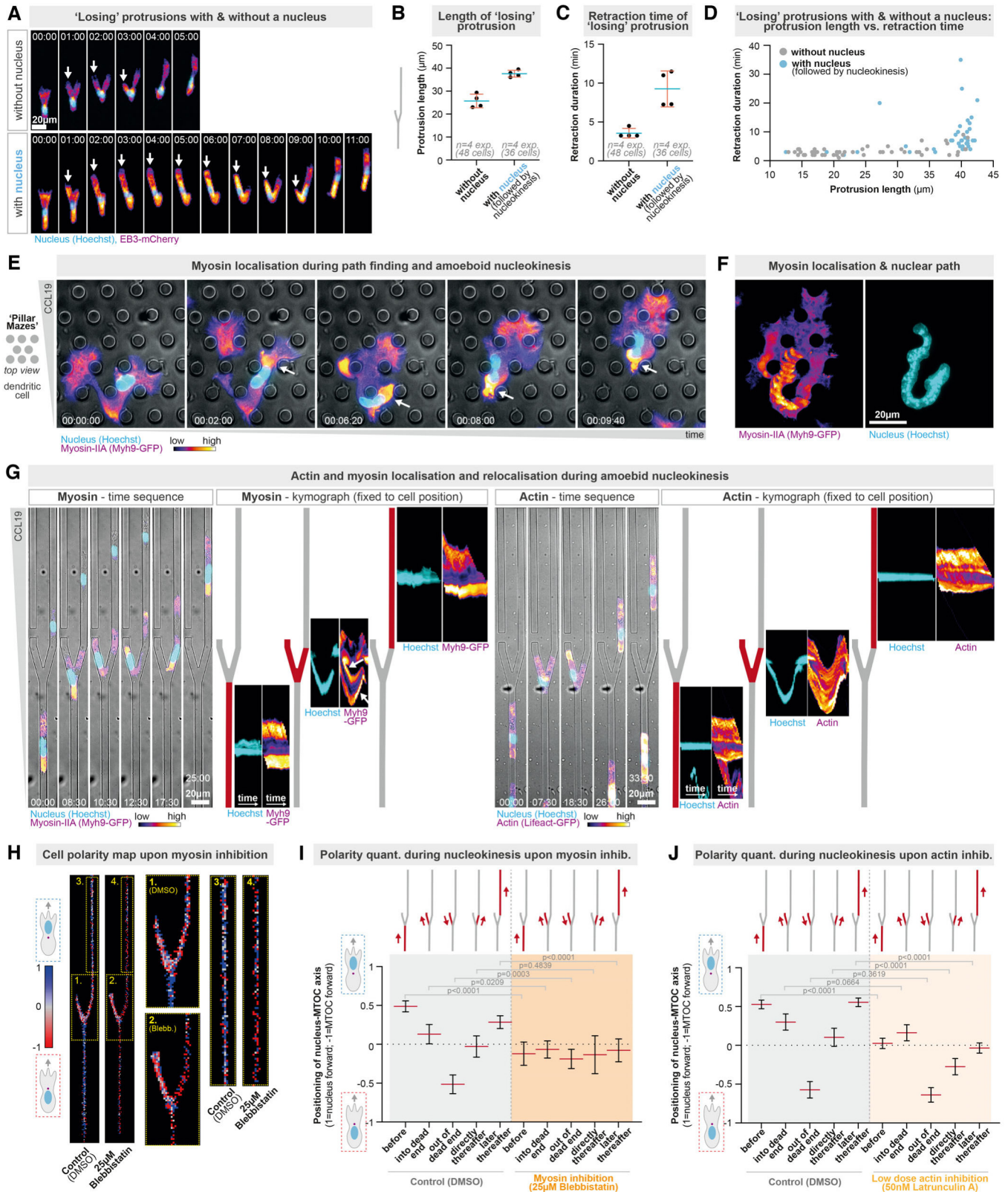


Figure 4.

Figure 4. Cell polarity switches during amoeboid nucleokinesis require a functional actomyosin cytoskeleton.

- A Protusion lengths of representative EB3-mCherry encoding DCs approaching a path decision with equal pore sizes but one blocked path, either with or without nucleus in the “losing” protusion. The nucleus (Hoechst) is shown in cyan. Time in mins.
- B Quantification of the lengths of “losing” protusions, comparing “losing” protusions without a nucleus and with a nucleus. Data are Mean \pm SD. $N = 4$ replicates (48 cells and 36 cells). Note that “losing” protusions with a nucleus are longer than “losing” protusions without a nucleus. See also (D) for a direct comparison of the retraction time of long “losing” protusions with and without a nucleus.
- C Quantification of the retraction time of “losing” protusions, comparing “losing” protusions without a nucleus and with a nucleus. Data are Mean \pm SD. $N = 4$ replicates (48 and 36 cells).
- D Protusion length vs. retraction time. $N = 4$ replicates.
- E Representative HoxB8-derived Myh9-GFP expressing DC migrating through a porous maze-like microenvironment composed of pillars interconnecting two surfaces below and above the migrating cell. Myh9-GFP localization is fire color-coded and the nuclear localization is shown in cyan (transient Hoechst label). Time in h:mins.
- F Time projection of Myh9-GFP and nuclear localization of the cell shown in (E).
- G Representative HoxB8-derived Myh9-GFP (left) and Lifeact-GFP (right) expressing DCs migrating through a path decision junction with equal pore sizes but one blocked path. The Myh9-GFP and Lifeact-GFP signal is fire color-coded and the nuclear localization is shown in cyan (transient Hoechst label). The kymographs show the signals over time and are depicted by fixing the position of the cell (see Materials and Methods for details) to better compare the signal distribution over time. Note the re-localization of the major Myh9-GFP signal from the back of the cell towards the back of the “losing” protusion during nucleokinesis (white arrows).
- H Heatmap of the nucleus-MTOC axis configuration during amoeboid nucleokinesis in the presence of the myosin-II inhibitor para-nitroblebbistatin (25 μ M) or control (DMSO). The yellow-dotted regions 1 (DMSO) and 2 (para-nitroblebbistatin) are enlarged to depict the cellular behavior during the initial nucleokinesis event, and the yellow-dotted regions 3 (DMSO) and 4 (para-nitroblebbistatin) are enlarged to depict the cellular behavior during the later nucleokinesis events to reposition the nucleus to the cellular front $N = 4$ replicates, 37 (DMSO) and 13 (para-nitroblebbistatin) cells.
- I Quantification of the nucleus-MTOC axis configuration before, during, directly after, and later after amoeboid nucleokinesis in the presence of the myosin-II inhibitor para-nitroblebbistatin (25 μ M) or control (DMSO) (1 = all cells position the nucleus in front of the MTOC; -1 = all cells position the MTOC in front of the nucleus). Data are mean \pm 95CI, Mann-Whitney test, $N = 4$ replicates, 37 (DMSO) and 13 (para-nitroblebbistatin) cells, and 582 (before; DMSO), 173 (before; para-nitroblebbistatin), 246 (into a dead end, DMSO), 315 (into a dead end, para-nitroblebbistatin), 198 (out of a dead end, DMSO), 244 (out of a dead end, para-nitroblebbistatin), 208 (directly thereafter, DMSO), 67 (directly thereafter, para-nitroblebbistatin), 523 (later thereafter, DMSO), and 180 (later thereafter, para-nitroblebbistatin) image frames.
- J Quantification of the nucleus-MTOC axis configuration before, during, directly after, and later after amoeboid nucleokinesis in the presence of the actin inhibitor LatrunculinA (50 nM) or control (DMSO) (1 = all cells position the nucleus in front of the MTOC; -1 = all cells position the MTOC in front of the nucleus). Data are mean \pm 95CI, Mann-Whitney test, $N = 3$ replicates, 78 (DMSO) and 13 (LatrunculinA) cells, and 900 (before; DMSO), 866 (before; LatrunculinA), 323 (into a dead end, DMSO), 351 (into a dead end, LatrunculinA), 234 (out of a dead end, DMSO), 265 (out of a dead end, LatrunculinA), 281 (directly thereafter, DMSO), 328 (directly thereafter, LatrunculinA), 902 (later thereafter, DMSO), and 899 (later thereafter, LatrunculinA) image frames.

Source data are available online for this figure.

On top of this speed challenge, rapidly migrating cells also provide a morphological challenge: the fastest migrating cells are typically amoeboid cells, including many immune cells, which have complex, ramified cell shapes that dynamically and constantly change during navigation along the migration path, raising the question whether and how nuclear positioning is coordinated with these highly dynamic changes in cell shape.

Here, we investigated major cellular models of fast amoeboid migrating cells, including immune cells (dendritic cells and T cells) and the single-cell amoeba *D. discoideum*, and discovered that motile amoeboid cells actively move and reposition their nuclei during pathfinding. Nuclear movement in amoeboid cells is extraordinarily efficient and frequent, functioning in a very rapid manner over long intracellular distances. Given the similarity of this type of nuclear movement to the movement properties of entire amoeboid cells, we name this newly described mode of nuclear movement as “amoeboid nucleokinesis.” Amoeboid nucleokinesis appears to function independently of a direct role of the microtubule cytoskeleton, as microtubule depolymerization did not impair the speed of nuclear repositioning. Instead, our findings show that amoeboid nucleokinesis requires forces from the actomyosin cytoskeleton. While forces from actin and myosin are well known to be important for the advance and retraction of individual protrusions and the entire cell body, as well as for the squeezing of the cell body and the nucleus (Lämmermann et al, 2008; Thiam et al, 2016; Barbier et al, 2019), our reductionistic microchannel approach enabled us to investigate the principles of amoeboid nucleokinesis independent of squeezing and general migration or retraction defects. This approach revealed

that the retraction of a “losing” protusion containing the nucleus is a particular challenge, requiring myosin forces to reposition the nucleus towards the “winning” protusion during the first phase of nucleokinesis and into an intracellular location ahead of the MTOC during the second phase. Given the rapid temporal scale of nuclear repositioning and the two rapid switches in the nucleus-MTOC axis configuration, it will be interesting to investigate whether amoeboid nucleokinesis may involve a tight anchorage between the actomyosin cytoskeleton and the nucleus, or may function through an anchorage-independent mechanism driven by myosin forces located at the rear of the nucleus. Considering the accumulation of myosin behind the nucleus, it is tempting to speculate that myosin pushes the nucleus during amoeboid nucleokinesis. Alternatively, myosin may also pull the nucleus from the front, which though would likely require tight anchorage between actomyosin filaments and the nucleus, and adhesive cellular contacts with the microenvironment to stably attach the pulling force, the latter being less typical for non- or low-adhesive amoeboid migrating cells.

Functionally, we discover that amoeboid nucleokinesis is required for amoeboid cell migration in complex mechanochemical microenvironments. Specifically, amoeboid nucleokinesis allows cells to adapt their path flexibly when a dominant guidance cue emerges, in particular when the nucleus follows initially the path of least resistance through a larger pore but then the cell decides to migrate along the path of another, alternative protusion along a dominating chemotactic cue. When amoeboid nucleokinesis is impaired, cells are less efficient to adapt their path and may become trapped. Tissue microenvironments typically present a variety of

chemical and mechanical cues, including differently sized pores. These microenvironmental pores can be very heterogenous in size, typically in the range of 2–10 μm, and are thus considerably

smaller than the cellular diameter (Wolf et al, 2009; Weigel et al, 2012; Kameritsch & Renkawitz, 2020). While motile amoeboid cells can use their nucleus as a gauge to probe the pore

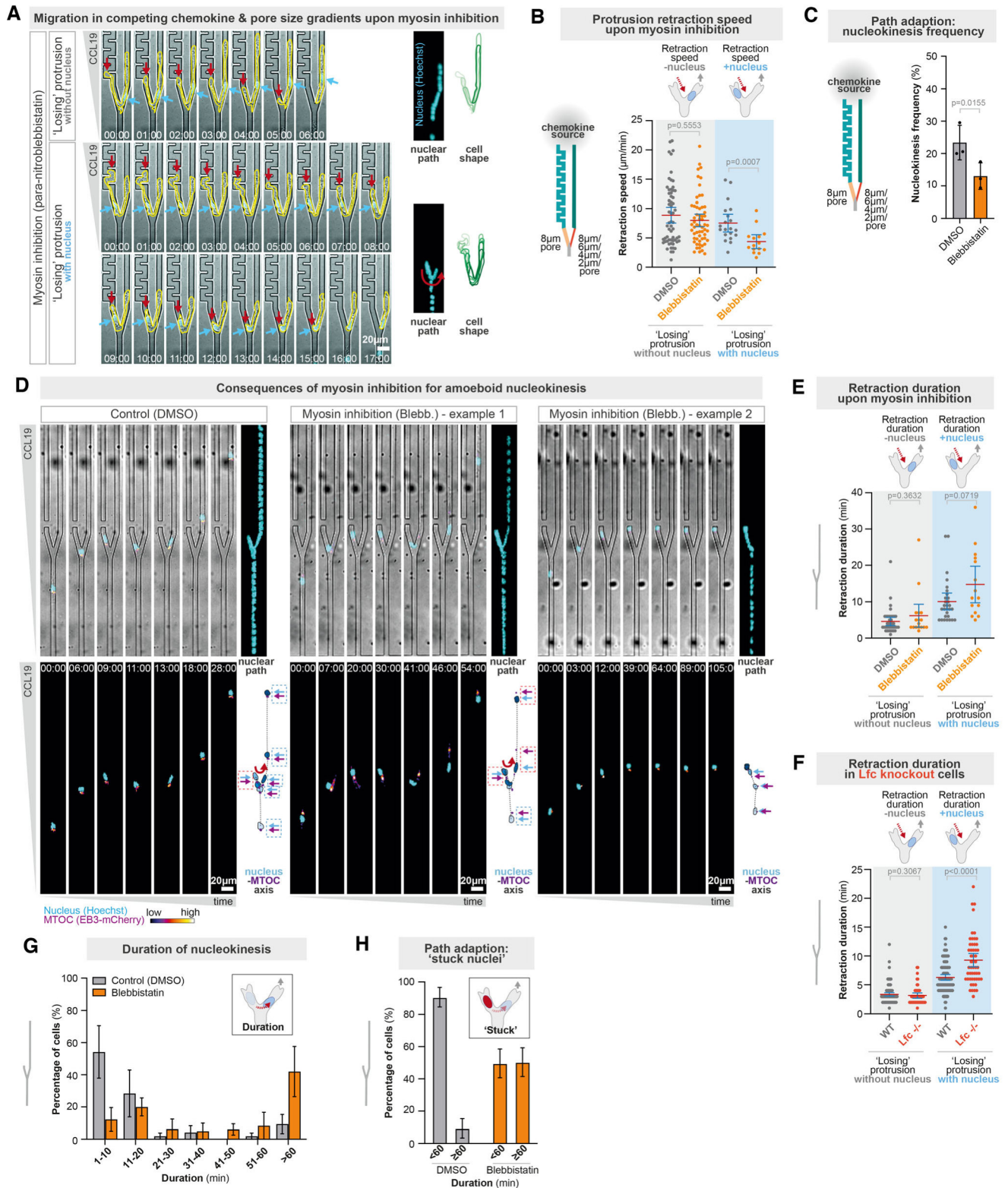


Figure 5.

Figure 5. Myosin-based forces drive amoeboid nucleokinesis to ensure adaptive pathfinding.

- A Representative bone-marrow derived DCs migrating through path decision with competing chemokine and pore size gradients in the presence of the myosin-II inhibitor para-nitroblebbistatin (25 μ M), showing representative cells with and without the nucleus in the 'losing' protrusion. The cell shape is outlined in yellow, and the red arrow highlights the retraction of the "losing" protrusion. The nucleus is shown in cyan (Hoechst) and highlighted by cyan arrows.
- B Quantification of (A), measuring the retracting speed of "losing" protrusions in the presence of the myosin-II inhibitor para-nitroblebbistatin (25 μ M) or control (DMSO), depending on whether the "losing" protrusion contains the nucleus or not. Data are Mean \pm 95CI, Mann-Whitney test, $N = 3$ replicates, 61 (DMSO, without nucleus), 59 (para-nitroblebbistatin, without nucleus), 20 (DMSO, with nucleus), and 15 (para-nitroblebbistatin, with nucleus) cells.
- C Quantification of (A), measuring the frequency of how often the cell adapts its path by nuclear reorientation from a "losing" towards a "winning protrusions in the microenvironments described in Fig 2. Data are Mean \pm SD, paired t test, $N = 3$ replicates, 182 (DMSO), and 136 (para-nitroblebbistatin) cells.
- D Representative HoxB8-derived DCs in the presence of the myosin-II inhibitor para-nitroblebbistatin (25 μ M) or control (DMSO). The DCs stably encode EB3-mCherry (to visualize the MTOC; fire color-coded) and are transiently stained with Hoechst (to visualize the nucleus; cyan). The left panel shows a representative control cell, the middle panel a representative myosin-inhibited cell with delayed nuclear repositioning to the front of the cell, and the right panel a representative myosin-inhibited cell that entirely fails to reposition to the productive open path. The configuration of the nucleus-MTOC axis is highlighted by dashed boxes (blue = nucleus forward; red = MTOC forward). Time in min:s.
- E Quantification of the retracting speed of "losing" protrusions in the presence of the myosin-II inhibitor para-nitroblebbistatin (25 μ M) or control (DMSO), depending on whether the "losing" protrusion contains the nucleus or not. Data are Mean \pm 95CI, Mann-Whitney test, $N = 4$ replicates, 60 (DMSO) and 25 (para-nitroblebbistatin) cells.
- F Quantification of the retracting speed of "losing" protrusions in control (WT) or $Lfc^{-/-}$ DCs, depending on whether the "losing" protrusion contains the nucleus or not. Data are Mean \pm 95CI, Mann-Whitney test, $N = 4$ replicates, 226 (WT) and 104 ($Lfc^{-/-}$) cells.
- G Quantification of the duration of nucleokinesis in the presence of the myosin-II inhibitor para-nitroblebbistatin (25 μ M) or control (DMSO). Data are mean \pm SEM. $N = 3$ replicates, 50 (DMSO) and 38 (para-nitroblebbistatin) cells.
- H Quantification of the percentage of cells that have a nucleus stuck in the blocked path for at least 60 min (myosin-II inhibitor para-nitroblebbistatin (25 μ M) vs. control (DMSO)). Data are mean \pm SEM. $N = 3$ replicates, 50 (DMSO) and 38 (para-nitroblebbistatin) cells.

Source data are available online for this figure.

size to select migration routes along larger, less detrimental pores (Renkawitz *et al.*, 2019), cells should be able to flexibly redirect their migration path upon the emergence of other cues. Here we showed this flexibility in microenvironments of competing chemokine and pores size cues, identifying that high chemokine concentrations can overrule pore size cues. Such a behavior appears to be highly relevant in physiological situations when cells are directed by chemotactic cues into dense or narrow tissue

microenvironments, such as when mature dendritic cells have to squeeze themselves through tiny openings of lymph capillaries during their travel to the lymph node (Pflücke & Sixt, 2009). Considering that virtually all motile cells simultaneously encounter a variety of chemical and mechanical signals in their immediate local microenvironment, our findings suggest that nucleokinesis plays a universally crucial role in the navigation of migrating cells.

Figure 6. Adaptive pathfinding by nucleokinesis in *Dictyostelium discoideum* amoebae.

- A Representative *Dictyostelium discoideum* cell migrating through a porous maze-like microenvironment composed of pillars interconnecting two surfaces below and above the migrating cell. The *Dictyostelium* cell stably expresses mRFP-histone (to visualize the nucleus; cyan) and the cell shape is outlined in green. Time projections of the cellular and nuclear paths are shown in shades of green and blue, respectively. Time in h:min:s.
- B Quantification of the speed of nuclear and cell front movement during nucleokinesis in *Dictyostelium* cells. Independent speeds of nucleus and cell front are shown on the left. Nuclear speed normalized to the cell front speed (fold change) is shown on the right. Data are mean \pm SD. $N = 3$ replicates, 25 cells.
- C Quantification of the speed of nuclear movement during nucleokinesis in DCs and *Dictyostelium* cells migrating in pillar mazes (DCs in pillars mazes with 9 μ m pores sizes, and *Dictyostelium* cells in pillar mazes with 5 μ m pore sizes). Data are median \pm 95CI. $N = 3$ replicates, 25 (*Dictyostelium*) and 30 (DCs) cells.
- D Quantification of the intracellular distance of nuclear movement during nucleokinesis in DCs and *Dictyostelium* cells migrating in pillar mazes. Data are median \pm 95CI. $N = 3$ replicates, 25 (*Dictyostelium*) and 30 (DCs) cells.
- E Quantification of the rate (left) and frequency (right) of nucleokinesis events in amoeboid migrating *Dictyostelium* cells and DCs. Rate: when the migrating cell has at least two major protrusions, quantification of whether the nucleus locates immediately into the dominant protrusion or first locates into the future retracting protrusion, requiring nucleokinesis into the future dominant protrusion. Frequency: showing the frequency of at least two leading edges and nucleokinesis events per minute. Data are mean \pm SD. $N = 3$ replicates, 25 (*Dictyostelium*) and 30 (DCs) cells.
- F Representative *Dictyostelium* cell migrating in a pillar maze. The *Dictyostelium* cell stably encodes GFP- α -tubulin, which also visualizes the microtubule-organizing center (MTOC; in pink) and mRFP-histone, which visualizes the nucleus (in cyan). The cell shape is outlined in green. Projections of cellular (green), MTOC (pink) and nuclear (blue) paths are shown on the right. Red arrows highlight full and partial nucleokinesis events. Time in min:s.
- G Quantification of the nucleus-MTOC axis configuration before and during nucleokinesis. Data are mean \pm SD. $N = 3$ replicates, 25 cells.
- H Quantification of the nucleus-MTOC axis configuration after nucleokinesis. The x-axis indicates the number of pillar crossings after nucleokinesis. Data are mean \pm SD. $N = 3$ replicates, 25 cells.
- I Quantification of the nucleus-MTOC axis configuration before, during, and after nucleokinesis upon myosin inhibition. Data are mean \pm SD. $N = 3$ replicates, 30 (DMSO) and 27 (para-nitroblebbistatin) cells.
- J Representative *Dictyostelium* cells (WT: top, HS2205 myosin mutant: bottom) migrating in a pillar maze. The *Dictyostelium* cells stably encode GFP- α -tubulin, which also visualizes the microtubule-organizing center (MTOC; in pink) and mRFP-histone, which visualizes the nucleus (in cyan). The cell shape is outlined in green. Projections of cellular (green), MTOC (pink) and nuclear (blue) paths are shown on the right. Red arrows highlight full and partial nucleokinesis events. Time in min:s.
- K Quantification of the nucleus-MTOC axis configuration before, during, and after nucleokinesis upon myosin mutation. Data are mean \pm SD. $N = 3$ replicates, 25 (WT) and 26 (HS2205; myosin mutant) cells.

Source data are available online for this figure.

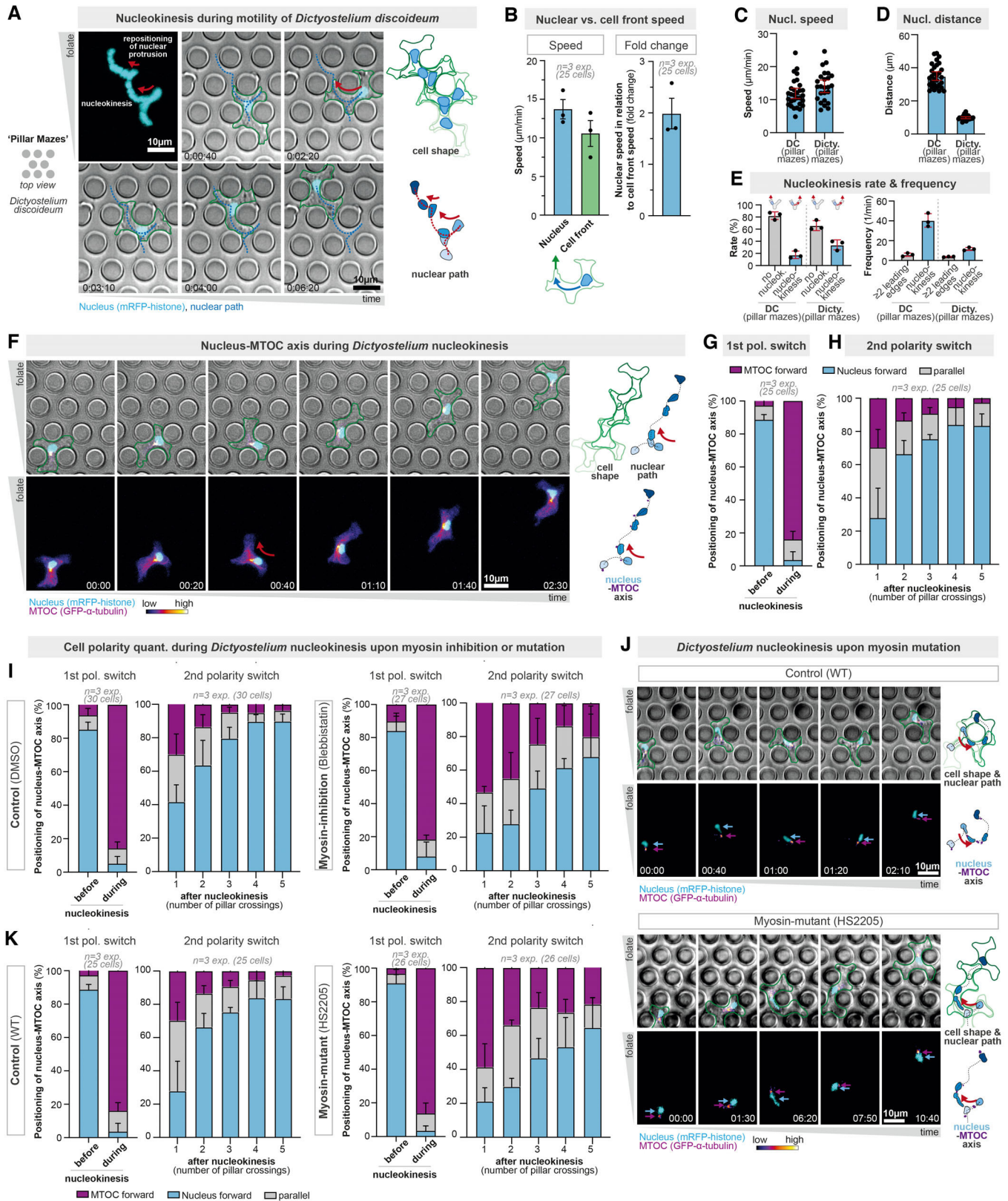


Figure 6.

Materials and Methods

Cell culture

Mammalian cell culture

All cells were kept at 37°C in a humidified incubator with 5% CO₂. DCs were differentiated either from the bone marrow of male C57B16/J wildtype mice (aged 8–12 weeks), male or female MyoIIA-Flox*CD11c-Cre mice (aged 8–11 weeks), or from Hoxb8 precursor lines (EB3-mCherry, EMTB-mCherry, Lifeact-GFP, Myh9-GFP, *Lfc*^{+/+} (WT control) and *Lfc*^{-/-} (KO)). Cells were differentiated in R10 medium (RPMI 1640 supplemented with 10% fetal calf serum (FCS), 2 mM L-glutamine, 100 U/ml penicillin, 100 mg/ml streptomycin, and 0.1 mM 2-mercaptoethanol; all Gibco) supplemented with 10% granulocyte-macrophage colony-stimulating factor (GM-CSF) hybridoma supernatant. Fresh medium was added on differentiation days 3 and 6. To induce maturation, either fresh or thawed DCs (differentiation day 8) were stimulated for 24 h with 200 ng/ml lipopolysaccharide (LPS; *E. coli* O26:B6, Sigma-Aldrich) and used for experiments on day 9. DCs derived from bone marrow from MyoIIA-Flox*CD11c-Cre mice were additionally differentiated for two more days (to enable longer Cre expression under the control of CD11c): additional fresh medium was added at day 8 and the cells were frozen at day 10, followed by stimulation with LPS upon thawing, and usage of the cells for experiments on day 11.

T cells were isolated from the spleen of male or female C57BL/6J mice (aged 6–12 weeks) using the EasySep mouse naive T cell isolation Kit (Stemcell). Cells were seeded onto cell culture plates coated with 1 µg/ml CD3 antibody and 1 µg/ml CD28 antibody and either used for experiments between differentiation days 3 and 6 or frozen at day 6 and thawed for experiments.

Dictyostelium discoideum

Cells of the *D. discoideum* strain AX2-214 (here designated as wild type), and the myosin-II deficient (*mhcA*-null) strain HS2205 derived from it (Manstein *et al*, 1989) were used. Nuclei and microtubules in both strains were visualized by expression of GFP- α -tubulin (*tubA1*; DDB0191380|DDB_G0287689) and mRFP-histone (*H2Bv3*; DDB0231622|DDB_G0286509) (Bindl *et al*, 2020; Ishikawa-Ankerhold *et al*, 2022). Cells were cultured in polystyrene Petri dishes containing HL5 medium (Formedium, Hunstanton, Norfolk, UK) supplemented with 10 µg/ml of blasticidin S (Gibco, Fisher Scientific GmbH, Schwerte, Germany), 20 µg/ml of geneticin (Sigma-Aldrich, Sigma-Aldrich Chemie GmbH, Taufkirchen, Germany), or 33 µg/ml hygromycin B (EMD Millipore Corp., Billerica, MA, USA) at 22°C. While the myosin-II-deficient mutant has been reported to have cytokinesis defects causing multinucleation, our adhesive cell culture conditions mostly resulted in single-nucleated cells and for analysis we only included those single-nucleated cells.

Mice

Wild-type animals were housed in the Core Facility Animal Models at the Biomedical Centre (Ludwig-Maximilians-Universität), and animal procedures and experiments were in accordance with the ministry of animal welfare of the region of Oberbayern and with the German law of animal welfare.

Flow cytometry analysis

DCs were routinely checked for surface marker expression using antibodies for CD11c (17-0114-82, Invitrogen) and MHCII (48-5321-82, Invitrogen). After Fc receptor blockage using an antibody for CD16/32 (14-0161-85, Invitrogen), stainings were performed in FACS buffer (1% BSA, 2 mM EDTA in PBS). Cells were analyzed using a Cytoflex S flow cytometer (Beckmann-Coulter).

Microfabricated devices

Microfabricated devices were generated as described previously (Renkawitz *et al*, 2018; Kroll *et al*, 2022). In brief, wafers produced by photolithography or epoxy replicates thereof were used as templates for micro-structures with defined lengths, widths, and heights. Micro-channels had a width of 8 µm. For analysis of adaptive pathfinding in competing chemokine and pore-size cues, pores were 2, 4, or 6 µm wide. Pore sizes in pillar forests were 5 and 9 µm for *D. discoideum* and DC migration, respectively. The height of the micro-structures ranged from 4 to 5 µm to ensure cell confinement from all sides.

Polydimethylsiloxane (PDMS; 10:1 mixture of Sylgard 184, Dow) was cast on the template micro-structures. PDMS was mixed in a Thinky mixer, and air bubbles were removed in a desiccator. After curing at 80°C overnight, PDMS was removed from the template and cut into single devices. Holes were punched on each side of the micro-structures to enable cell and chemokine loading. Subsequently, PDMS pieces were bonded to cleaned coverslips using a plasma cleaner. PDMS devices were placed at 120°C for 10 min and at 80°C overnight to ensure permanent bonding.

Simulation of chemokine diffusion

The geometry of an exemplary channel of the microchannel design was traced from a transmitted light image in Fiji and subsequently exported. A 2D model of the channel was generated from this data, and time-dependent diffusion was simulated using MATLAB's "solvepde" function. The boundary condition at the channel interface with the chemokine source was set to c_0 , and at the interface with the drain, it was set to 0 (Dirichlet boundary conditions). We used a diffusion constant of 1.3e-10 m²/s for CCL19, as previously described (Schwarz *et al*, 2016).

Live-cell migration assays

To visualize the nucleus for live-cell migration assays, cells were incubated with 1 drop of NucBlue (Invitrogen) in 1 ml of cell/media mixture for at least 30 min. SPY555-tubulin (Spirochrome) was used according to the manufacturer's protocol to visualize the MTOC. For pharmacological inhibition experiments, cells were treated with final concentrations of 50 nM Latrunculin A (Sigma-Aldrich), 25 µM para-nitroblebbistatin (Motorpharma; dissolved in DMSO), or 300 nM or 10 µM Nocodazole (Sigma-Aldrich). Control samples were treated with the respective DMSO dilution.

Microchannel migration assays

PDMS devices were flushed with phenol-free R10 medium supplemented with 50 µM L-ascorbic acid (Sigma-Aldrich) and pharmacological inhibitors if applicable for the experimental setup. Devices were

incubated at 37°C, 5% CO₂ for at least 1 h before the experiment. Subsequently, 0.625 µg/ml CCL19 (DCs) or 100 µM folate (*Dictyostelium*) were loaded into the chemokine loading hole to establish a gradient. Finally, 0.1–1 × 10⁵ cells were added into the opposite loading hole. When performing experiments with *Dictyostelium* cells in microchannels using either folate or cAMP as chemotactic cue, we rarely observed cells reaching the path decision points, as the microchannel designs included a long straight path before the path decision point. Thus, when investigating nucleokinesis in *Dictyostelium* cells, we loaded *Dictyostelium* into pillar forests, in which the cells immediately encounter a microenvironment with alternative path options on their migration path, enabling the investigation of nucleokinesis.

Visualization of chemokine gradient

For indirect visualization of the CCL19 gradient in the microchannels with competing chemokine and pore size gradients, 200 µg/ml dextran (10 kDa) coupled to Alexa Fluor™ 647 (Invitrogen) with a molecular weight and hydrodynamic radius comparable to CCL19 (Schwarz et al, 2016; Frick et al, 2018) was added to the chemokine loading hole.

Collagen migration assays

Collagen migration assays were performed as described previously (Kroll et al, 2022). Briefly, for DC or T cell migration in collagen, 1× minimum essential medium (MEM, Gibco), 0.4% sodium bicarbonate (Sigma-Aldrich), and Nutragen bovine collagen (Advanced BioMatrix) were mixed with 3–5 × 10⁵ cells in R10 medium at a 2:1 ratio, resulting in a final collagen density of 3.3 mg/ml. The collagen-cell solution was added into custom-made migration chambers (appr. 17 mm in width and 1 mm in height). After 75 min polymerization at 37°C, 5% CO₂, gels were overlaid with 80 µl CCL19 (0.625 µg/ml). For pharmacological inhibition experiments, inhibitors were added to the chemokine solution as well as the collagen-cell solution.

Under-agarose migration assays

Under-agarose migration assays were performed as described previously (Clausen et al, 2022). In brief, 4% UltraPure agarose (Invitrogen) in sterile water was mixed with 55°C prewarmed phenol-free RPMI-1640 (Gibco) supplemented with 20% FCS and 1× Hanks buffered salt solution pH 7.3 in a 1:3 ratio resulting in a final agarose concentration of 1%. The 1% agarose mixture was allowed to cool to 37°C before introducing the inhibitor to the respective final concentration. 300 µl of the agarose mixture were poured into each well of imaging-suitable 8-well slides (Ibidi). The under-agarose migration assay was left at room temperature for 1 h to polymerize and was subsequently transferred to an incubator (37°C, 5% CO₂) for another hour to equilibrate. After equilibration, four 2 mm holes were punched in each well using tissue biopsy punchers. 2.5 µg/ml CCL19 in phenol-free R10 were loaded into two adjacent loading holes. Finally, 1.5 × 10⁵ cells were loaded into each of the two opposite loading holes. The under-agarose migration assay was placed in the incubator for 4–5 h to let cells migrate under the agarose layer toward the chemokine source.

Immunofluorescence stainings

For immunofluorescence stainings, under-agarose migration assays were prepared as described above. Subsequently, cells were fixed

by adding prewarmed 3.7% paraformaldehyde (PFA, diluted in PBS) on top of the agarose. After 1 h of fixation at 37°C, 5% CO₂, PFA, and the agarose block were carefully removed, and cells were washed 3 times with PBS. Permeabilization was conducted with 1× SAPO buffer (0.2% BSA + 0.05% saponin diluted in PBS) for 30 min, followed by blocking with 5% BSA (diluted in 1× SAPO) for another 30 min. Primary antibodies were incubated at 4°C overnight (rat anti- α -tubulin: 1 µg/ml, MA1-80017, Invitrogen; diluted in 1× SAPO). Following washing of the cells with PBS (3 times), samples were stained with secondary antibodies (goat anti-rat Alexa Fluor™ Plus 647: 4 µg/ml, A48265, Invitrogen; diluted in 1× SAPO) and DAPI (1:1,000, Thermo Fisher Scientific) at room temperature for 1 h. Following washing with PBS (3 times), samples were mounted using Fluoromount-G (Invitrogen).

Imaging

Live-cell imaging of dendritic cells and T cells was performed at 37°C and with 5% CO₂ in a humidified chamber. Live-cell imaging of *D. discoideum* was conducted at room temperature (22°C). Data were recorded using inverted DMi8 microscopes (Leica) with HC PL FLUOTAR 4×/0.5 PH0 air, HC PL APO 20×/0.80 PH2 air, or HC PL APO 40×/0.95 CORR air objectives. Additionally, the microscope was equipped with an LED5 (Leica) or pE-4000 (CoolLED) light source, an incubation chamber, a heated stage, and a CO₂ mixer (Pecan). Immunofluorescence stainings were imaged on an inverted wide-field DMi8 microscope (Leica) with an HC PL APO 100×/1.47 oil objective. Imaging data presented in Figs 1 and 4 are available in the external repository “BioImage Archive” EMBL-EBI via “BioStudies” (Sarkans et al, 2018) under the accession number S-BIAD901.

Image analysis

Fiji/ImageJ (Schindelin et al, 2012) and Imaris (Bitplane) were used for image processing. Generally, only single, noninteracting cells were used for quantification to exclude the influence of neighboring cells on cell path, speed, pore size decision, or the nucleus—MTOC axis. We defined nucleokinesis as intracellular movement of the nucleus for at least one nuclear length relative to cell body, moving from a “losing” protrusion toward a “winning” protrusion.

The overall speed of cells in collagen matrices was analyzed using a custom-made cell tracking tool for ImageJ (Kiermaier et al, 2016). In brief, image sequences were background corrected, and particle filtering was used to exclude objects larger or smaller than cells. Each image of the sequence was matched with the optimal overlap in its lateral displacement to the previous frame. Finally, migration velocity was calculated from the y-displacement and the time between two consecutive frames. Speed and distance of nucleus and MTOC in single migrating DCs, T cells, and *Dictyostelium* cells in collagen matrices as well as in pillar forests were analyzed using the manual tracking plugin in Fiji (v2.1.1). Orientation of nucleus and MTOC, as well as nuclear repositioning (whole nuclear body located in losing protrusion followed by full repositioning into winning protrusion), was quantified manually in Fiji.

For the analysis of cells migrating in 1x dead end-channels, the nuclei were tracked using the tracking function of Imaris v9.7.2 with the following settings: object diameter 10 µm, manually adjusted quality threshold, autoregressive motion tracking algorithm (max.

distance 20 μm , gap size = 1). MTOC signals were either tracked manually in Imaris (SPY555-tubulin and EMTB-mCherry) or segmented in ilastik 1.4.0 (Berg *et al*, 2019) (EB3-mCherry) and then tracked using the tracking function of Imaris v9.7.2 with the following settings: object diameter 3 μm , manually adjusted quality threshold, autoregressive motion tracking algorithm (max. distance 25 μm , gap size = 3). Subsequently, all automated tracking was manually evaluated for errors. The cell rear was tracked manually in Imaris. Position data for nuclei and MTOCs were exported and analyzed by a custom-made Matlab script. To accurately associate MTOC tracks with corresponding nuclei, track pairing is achieved by minimizing the convex hull volume between their points. For each nuclear track, the motion direction is calculated, followed by determining the MTOC's distance and orientation relative to the nucleus. To categorize distinct zones within the 1 \times dead end-channels, their x/y coordinates, and orientations are initially computed using template matching. Subsequently, data from all tracks is consolidated, and maps depicting speed, orientation, and MTOC distance are generated for in-depth analysis.

To analyze retraction dynamics of protrusions with or without nucleus in cells migrating in the 1 \times dead-end-channels, retraction length, and duration were quantified manually in Imaris.

To measure fluorescence intensities of dextran (10 kDa) coupled to Alexa Fluor™ 647 in the microchannels with competing chemokine and pore size gradients, a rectangular ROI (region of interest) of a defined size was selected on each side of the bifurcation (as indicated in Fig 2B) and the mean intensity was measured over multiple channels. Finally, the fold change was calculated by dividing the mean fluorescence intensity in the “close” channel part by the mean fluorescence intensity in the “distant” channel part.

To visualize the actin and myosin distribution of cells migrating in 1 \times dead-end-channels, polyline regions of interest were manually drawn on each y -channel separately. The Fiji plug-in kymoreslice-wide was then used to create kymographs that show the average of the myosin/actin associated fluorescence over the full width of the microfluidics channels. These kymographs were subsequently transformed from the lab frame of reference to co-moving kymographs. To this end, the cell nuclei were tracked separately with Imaris. The exported center of mass coordinates were used to laterally shift each line of the raw kymographs, so that the nucleus stayed fixed, hence stabilizing the kymograph and yielding the co-moving kymographs of the cells.

Statistics

All replicates were validated independently and represent biological replicates. Samples that did not show migrating cells were excluded. Statistical analysis was conducted using GraphPad Prism using the appropriate tests according to normal or non-normal data distribution as stated in the figure legends. Error bars are defined in the figure legends. No blinding, randomization, and samples size estimations were performed.

Data availability

Imaging data presented in Figs 1 and 4 are available in the external repository “BioImage Archive” EMBL-EBI via “BioStudies” under

the accession number S-BIAD901 (<https://www.ebi.ac.uk/biostudies/bioimages/studies/S-BIAD901>). Computational image analysis scripts are available upon request.

Expanded View for this article is available [online](#).

Acknowledgements

We thank Christoph Mayr and Bingzhi Wang for initial experiments on amoeboid nucleokinesis, Ana-Maria Lennon-Duménil and Aline Yatim for bone marrow from MyoIIA-Flox*CD11c-Cre mice, Michael Sixt and Aglaja Kopf for EMTB-mCherry, EB3-mCherry, Lifeact-GFP, Lfc knockout, and Myh9-GFP expressing HoxB8 cells, Malte Benjamin Braun, Mauricio Ruiz, and Madeleine T. Schmitt for critical reading of the manuscript, and the Core Facility Bioimaging, the Core Facility Flow Cytometry, and the Animal Core Facility of the Biomedical Center (BMC) for excellent support. This study was supported by the Peter Hans Hofschneider Professorship of the foundation “Stiftung Experimentelle Biomedizin” (to JR), the LMU Institutional Strategy LMU-Excellent within the framework of the German Excellence Initiative (to JR), and the Deutsche Forschungsgemeinschaft (DFG; German Research Foundation; SFB914 project A12, to JR), and the CZI grant DAF2020-225401 (<https://doi.org/10.37921/120055ratwvi>) from the Chan Zuckerberg Initiative DAF (to RH; an advised fund of Silicon Valley Community Foundation (funder <https://doi.org/10.13039/100014989>)). Open Access funding enabled and organized by Projekt DEAL

Author contributions

Janina Kroll: Conceptualization; investigation; methodology; writing – original draft; writing – review and editing. **Robert Hauschild:** Software; writing – review and editing. **Artur Kuznetsov:** Investigation; writing – review and editing. **Kasia Stefanowski:** Investigation; writing – review and editing. **Monika D Hermann:** Investigation; writing – review and editing. **Jack Merrin:** Methodology; writing – review and editing. **Lubuna Shafeek:** Methodology; writing – review and editing. **Annette Müller-Taubenberger:** Resources; writing – review and editing. **Jörg Renkawitz:** Conceptualization; supervision; funding acquisition; investigation; writing – original draft; project administration; writing – review and editing.

Disclosure and competing interests statement

The authors declare that they have no conflict of interest.

References

- Andrew N, Insall RH (2007) Chemotaxis in shallow gradients is mediated independently of PtdIns 3-kinase by biased choices between random protrusions. *Nat Cell Biol* 9: 193–200
- Barbier L, Sáez PJ, Attia R, Lennon-Duménil A-M, Lavi I, Piel M, Vargas P (2019) Myosin II activity is selectively needed for migration in highly confined microenvironments in mature dendritic cells. *Front Immunol* 10: 747
- Berg S, Kutra D, Kroeger T, Straehle CN, Kausler BX, Haubold C, Schiegg M, Ales J, Beier T, Rudy M *et al* (2019) ilastik: interactive machine learning for (bio)image analysis. *Nat Methods* 16: 1226–1232
- Bindl J, Molnar ES, Ecke M, Prassler J, Müller-Taubenberger A, Gerisch G (2020) Unilateral cleavage furrows in multinucleate cells. *Cells* 9: 1493
- Bornens M (2008) Organelle positioning and cell polarity. *Nat Rev Mol Cell Biol* 9: 874–886
- Bouchet BP, Akhmanova A (2017) Microtubules in 3D cell motility. *J Cell Sci* 130: 39–50

- Cadot B, Gache V, Gomes ER (2015) Moving and positioning the nucleus in skeletal muscle – one step at a time. *Nucleus* 6: 373–381
- Calero-Cuenca FJ, Janota CS, Gomes ER (2018) Dealing with the nucleus during cell migration. *Curr Opin Cell Biol* 50: 35–41
- Charras G, Sahai E (2014) Physical influences of the extracellular environment on cell migration. *Nat Rev Mol Cell Biol* 15: 813–824
- Clausen BE, Amon L, Backer RA, Berod L, Bopp T, Brand A, Burgdorf S, Chen L, Da M, Distler U et al (2022) Guidelines for mouse and human DC functional assays. *Eur J Immunol* <https://doi.org/10.1002/eji.202249925>
- Devreotes PN, Bhattacharya S, Edwards M, Iglesias PA, Lampert T, Miao Y (2017) Excitable signal transduction networks in directed cell migration. *Annu Rev Cell Dev Biol* 33: 103–125
- Driscoll MK, Welf ES, Jamieson AR, Dean KM, Isogai T, Fiolka R, Danuser G (2019) Robust and automated detection of subcellular morphological motifs in 3D microscopy images. *Nat Methods* 14: 1–8
- Frick C, Dettinger P, Renkawitz J, Jauch A, Berger CT, Recher M, Schroeder T, Mehling M (2018) Nano-scale microfluidics to study 3D chemotaxis at the single cell level. *PLoS ONE* 13: e0198330
- Fritz-Laylin LK, Riel-Mehan M, Chen B-C, Lord SJ, Goddard TD, Ferrin TE, Nicholson-Dykstra SM, Higgs H, Johnson GT, Betzig E et al (2017) Actin-based protrusions of migrating neutrophils are intrinsically lamellar and facilitate direction changes. *Elife* 6: e26990
- Gerisch G, Keller HU (1981) Chemotactic reorientation of granulocytes stimulated with micropipettes containing fMet-Leu-Phe. *J Cell Sci* 52: 1–10
- Gundersen GG, Worman HJ (2013) Nuclear positioning. *Cell* 152: 1376–1389
- Hadjitheodorou A, Bell GRR, Ellett F, Shastry S, Irimia D, Collins SR, Theriot JA (2021) Directional reorientation of migrating neutrophils is limited by suppression of receptor input signaling at the cell rear through myosin II activity. *Nat Commun* 12: 6619
- Hadjitheodorou A, Bell GRR, Ellett F, Irimia D, Tibshirani R, Collins SR, Theriot JA (2023) Leading edge competition promotes context-dependent responses to receptor inputs to resolve directional dilemmas in neutrophil migration. *Cell Syst* 14: 196–209
- Hauser MA, Schaeuble K, Kindinger I, Impellizzeri D, Krueger WA, Hauck CR, Boyman O, Legler DF (2016) Inflammation-induced CCR7 oligomers form scaffolds to integrate distinct signaling pathways for efficient cell migration. *Immunity* 44: 59–72
- Ishikawa-Ankerhold H, Kroll J, van den Heuvel D, Renkawitz J, Müller-Taubenberger A (2022) Centrosome positioning in migrating dictyostelium cells. *Cells* 11: 1776
- Kalukula Y, Stephens AD, Lammerding J, Gabriele S (2022) Mechanics and functional consequences of nuclear deformations. *Nat Rev Mol Cell Biol* 23: 583–602
- Kameritsch P, Renkawitz J (2020) Principles of leukocyte migration strategies. *Trends Cell Biol* 30: 818–832
- Kay RR, Langridge P, Traynor D, Hoeller O (2008) Changing directions in the study of chemotaxis. *Nat Rev Mol Cell Biol* 9: 455–463
- Képiró M, Várkuti BH, Végner L, Vörös G, Hegyi G, Varga M, Málnási-Csizmadia A (2014) para-nitroblebbistatin, the non-cytotoxic and photostable myosin II inhibitor. *Angew Chem Int Ed* 53: 8211–8215
- Kiermaier E, Moussion C, Veldkamp CT, Gerardy-Schahn R, de Vries I, Williams LG, Chaffee GR, Phillips AJ, Freiberger F, Imre R et al (2016) Polysialylation controls dendritic cell trafficking by regulating chemokine recognition. *Science* 351: 186–190
- Kopf A, Renkawitz J, Hauschild R, Girkontaite I, Tedford K, Merrin J, Thorn-Seshold O, Trauner D, Häcker H, Fischer K-D et al (2020) Microtubules control cellular shape and coherence in amoeboid migrating cells. *J Cell Biol* 219: e201907154
- Krendel M, Zenke FT, Bokoch GM (2002) Nucleotide exchange factor GEF-H1 mediates cross-talk between microtubules and the Actin cytoskeleton. *Nat Cell Biol* 4: 294–301
- Kroll J, Ruiz-Fernandez MJA, Braun MB, Merrin J, Renkawitz J (2022) Quantifying the probing and selection of microenvironmental pores by motile immune cells. *Curr Protoc* 2: e407
- Lämmermann T, Bader BL, Monkley SJ, Worbs T, Wedlich-Söldner R, Hirsch K, Keller M, Förster R, Critchley DR, Fässler R et al (2008) Rapid leukocyte migration by integrin-independent flowing and squeezing. *Nature* 453: 51–55
- Leithner A, Eichner A, Müller J, Reversat A, Brown M, Schwarz J, Merrin J, de Gorter DJJ, Schur F, Bayerl J et al (2016) Diversified Actin protrusions promote environmental exploration but are dispensable for locomotion of leukocytes. *Nat Cell Biol* 18: 1253–1259
- Lomakin AJ, Cattin CJ, Cuvelier D, Alraies Z, Molina M, Nader GPF, Srivastava N, Sáez PJ, Garcia-Arcos JM, Zhitnyak IY et al (2020) The nucleus acts as a ruler tailoring cell responses to spatial constraints. *Science* 370: eaba2894
- Luxton GG, Gundersen GG (2011) Orientation and function of the nuclear-centrosomal axis during cell migration. *Curr Opin Cell Biol* 23: 579–588
- Luxton GWG, Gomes ER, Folker ES, Vintinner E, Gundersen GG (2010) Linear arrays of nuclear envelope proteins harness retrograde actin flow for nuclear movement. *Science* 329: 956–959
- Manstein DJ, Titus MA, Lozanne AD, Spudich JA (1989) Gene replacement in dictyostelium: generation of myosin null mutants. *EMBO J* 8: 923–932
- Moreau HD, Piel M, Voituriez R, Lennon-Duménil A-M (2018) Integrating physical and molecular insights on immune cell migration. *Trends Immunol* 39: 632–643
- Norden C, Young S, Link BA, Harris WA (2009) Actomyosin is the main driver of interkinetic nuclear migration in the retina. *Cell* 138: 1195–1208
- Nourshargh S, Alon R (2014) Leukocyte migration into inflamed tissues. *Immunity* 41: 694–707
- Pflicke H, Sixt M (2009) Preformed portals facilitate dendritic cell entry into afferent lymphatic vessels. *J Exp Med* 206: 2925–2935
- Reinsch S, Gonczy P (1998) Mechanisms of nuclear positioning. *J Cell Sci* 111: 2283–2295
- Renkawitz J, Reversat A, Leithner A, Merrin J, Sixt M (2018) Micro-engineered “pillar forests” to study cell migration in complex but controlled 3D environments. *Methods Cell Biol* 147: 79–91
- Renkawitz J, Kopf A, Stopp J, de Vries I, Driscoll MK, Merrin J, Hauschild R, Welf ES, Danuser G, Fiolka R et al (2019) Nuclear positioning facilitates amoeboid migration along the path of least resistance. *Nature* 568: 546–550
- Sarkans U, Gostev M, Athar A, Behranghi E, Melnichuk O, Ali A, Minguet J, Rada JC, Snow C, Tikhonov A et al (2018) The BioStudies database—one stop shop for all data supporting a life sciences study. *Nucleic Acids Res* 46: D1266–D1270
- Schindelin J, Arganda-Carreras I, Frise E, Kaynig V, Longair M, Pietzsch T, Preibisch S, Rueden C, Saalfeld S, Schmid B et al (2012) Fiji: an open-source platform for biological-image analysis. *Nat Methods* 9: 676–682
- Schwarz J, Bierbaum V, Merrin J, Frank T, Hauschild R, Bollenbach T, Tay S, Sixt M, Mehling M (2016) A microfluidic device for measuring cell migration towards substrate-bound and soluble chemokine gradients. *Sci Rep* 6: 36440
- Schwarz J, Bierbaum V, Vahtomeri K, Hauschild R, Brown M, de Vries I, Leithner A, Reversat A, Merrin J, Tarrant T et al (2017) Dendritic cells interpret haptotactic chemokine gradients in a manner governed by signal-to-noise ratio and dependent on GRK6. *Curr Biol* 27: 1314–1325
- Swanson JA, Taylor DL (1982) Local and spatially coordinated movements in *Dictyostelium discoideum* amoebae during chemotaxis. *Cell* 28: 225–232
- Thiam H-R, Vargas P, Carpi N, Crespo CL, Raab M, Terriac E, King MC, Jacobelli J, Alberts AS, Stradal T et al (2016) Perinuclear Arp2/3-driven Actin

- polymerization enables nuclear deformation to facilitate cell migration through complex environments. *Nat Commun* 7: 10997
- Tsai L-H, Gleeson JG (2005) Nucleokinesis in neuronal migration. *Neuron* 46: 383–388
- van Helvert S, Storm C, Friedl P (2018) Mechanoreciprocity in cell migration. *Nat Cell Biol* 20: 8–20
- Venturini V, Pezzano F, Castro FC, Häkkinen H-M, Jiménez-Delgado S, Colomer-Rosell M, Marro M, Tolosa-Ramon Q, Paz-López S, Valverde MA et al (2020) The nucleus measures shape changes for cellular proprioception to control dynamic cell behavior. *Science* 370: eaba2644
- Weigel B, Bakker G-J, Friedl P (2012) Intravital third harmonic generation microscopy of collective melanoma cell invasion. *Intravital* 1: 32–43
- Wolf K, Alexander S, Alexander S, Schacht V, Schacht V, Coussens LM, Coussens LM, von Andrian UH, van Rheenen J, van Rheenen J et al (2009) Collagen-based cell migration models in vitro and in vivo. *Semin Cell Dev Biol* 20: 931–941
- Wolf K, Lindert M t, Krause M, Alexander S, Riet J t, Willis AL, Hoffman RM, Figdor CG, Weiss SJ, Friedl P (2013) Physical limits of cell migration: control by ECM space and nuclear deformation and tuning by proteolysis and traction force. *J Cell Biol* 201: 1069–1084
- Worbs T, Hammerschmidt SI, Förster R (2017) Dendritic cell migration in health and disease. *Nat Rev Immunol* 17: 30–48
- Yamada KM, Sixt M (2019) Mechanisms of 3D cell migration. *Nat Rev Mol Cell Biol* 20: 738–752
- Zhu R, Liu C, Gundersen GG (2018) Nuclear positioning in migrating fibroblasts. *Semin Cell Dev Biol* 82: 41–50



License: This is an open access article under the terms of the [Creative Commons Attribution-NonCommercial-NoDerivs](https://creativecommons.org/licenses/by-nc-nd/4.0/) License, which permits use and distribution in any medium, provided the original work is properly cited, the use is non-commercial and no modifications or adaptations are made.

Expanded View Figures

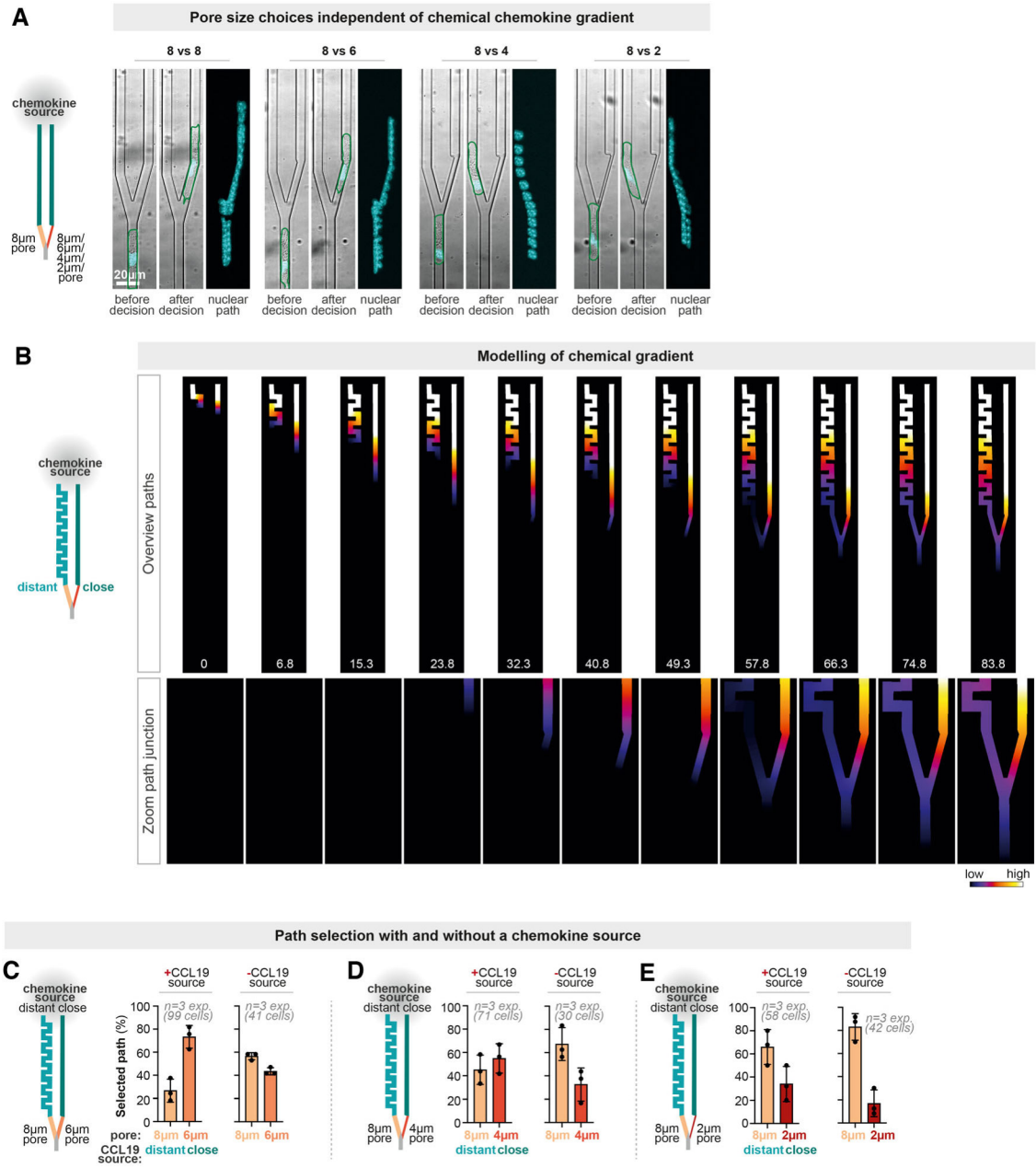


Figure EV1.

Figure EV1. Novel reductionistic assays to characterize cellular path choices in competing chemokine and pore size gradients.

- A Representative bone marrow-derived DCs (BMDC) migrating in microchannels with two-way path junctions with different pore sizes (8 vs. 8; 8 vs. 6; 8 vs. 4; or 8 vs. 2 μm) but an equally long and symmetric path towards the chemokine source. The cell shape is outlined in green and the nucleus is visualized by Hoechst (cyan). See Fig 2A for quantification.
- B Time-dependent simulation of CCL19 diffusion at a two-way path junction (with a diffusion constant of $1.3\text{e-}10 \text{ m}^2/\text{s}$), at one path is closer to the source of the chemokine than the alternative path, which follows a snake-like pattern and thus is more distant to the chemokine source. Time in seconds.
- C Quantification of cellular path decisions in microenvironments of competing chemokine and pore size gradients (as shown in Fig 2C) with and without chemokines source. $N = 3$ replicates (99 cells +CCL19; 41 cells without CCL19). Note that the comparative dataset of cells with CCL19 is the same data as in main Fig 2F. Data are Mean \pm SD.
- D Quantification of cellular path decisions in microenvironments of competing chemokine and pore size gradients (as shown in Fig 2D) with and without chemokines source. $N = 3$ replicates (71 cells +CCL19; 30 cells without CCL19). Note that the comparative dataset of cells with CCL19 is the same data as in main Fig 2G. Data are Mean \pm SD.
- E Quantification of cellular path decisions in microenvironments of competing chemokine and pore size gradients (as shown in Fig 2E) with and without chemokines source. $N = 3$ replicates (58 cells +CCL19; 42 cells without CCL19). Note that the comparative dataset of cells with CCL19 is the same data as in main Fig 2H. Data are Mean \pm SD.

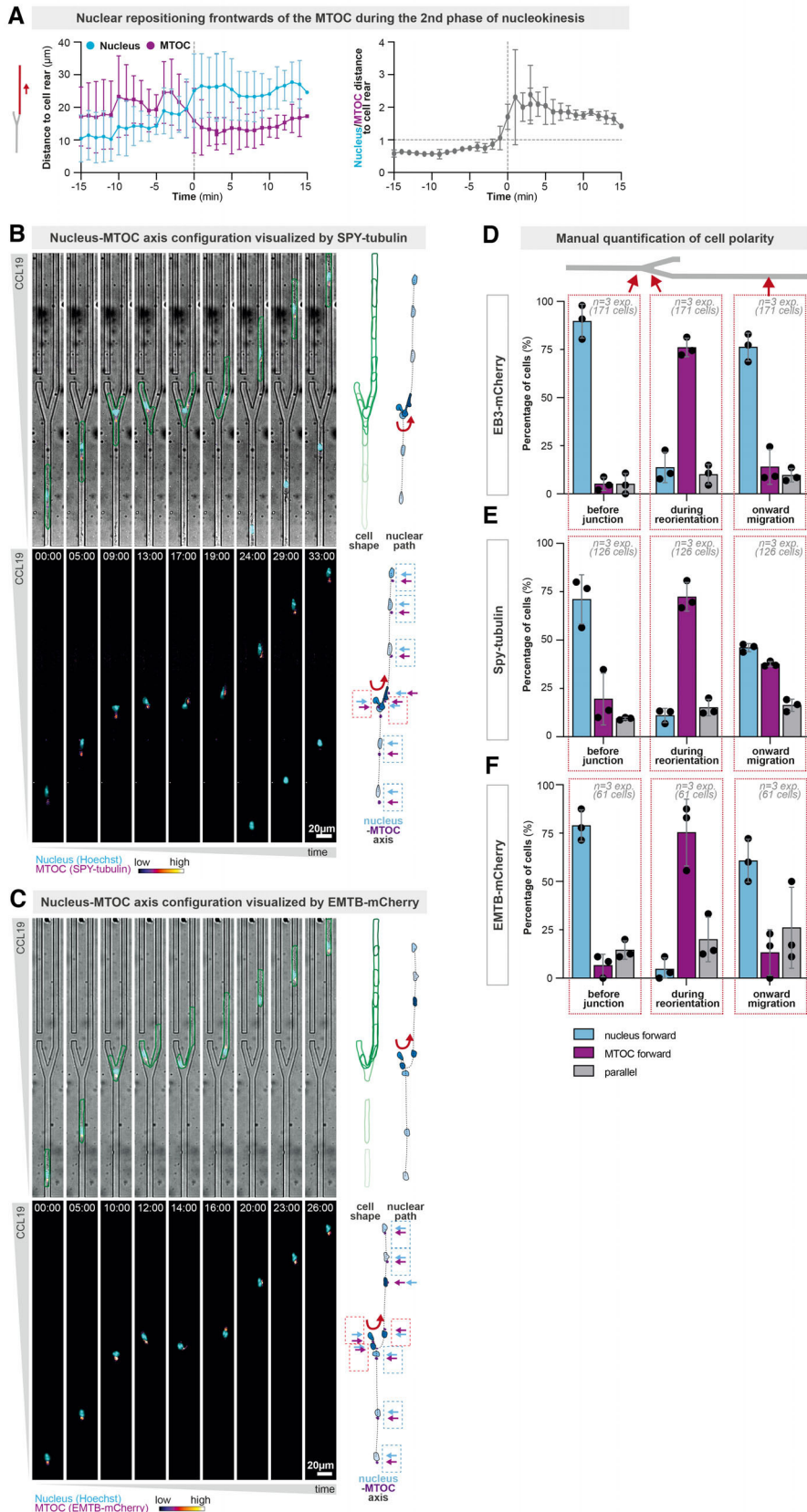


Figure EV2. Quantification of re-orientations in the configuration of the nucleus-MTOC axis during amoeboid nucleokinesis.

A Quantification of the distance of the nucleus and MTOC to the cell rear during the second phase of nucleokinesis, showing that the nucleus moves intracellularly into the front of the MTOC (left panel); the right panel shows the same data but plotting the ratios of nucleus and MTOC distances to the cell rear, highlighting that the nucleus increases its distance to the cell rear during the second phase of nucleokinesis. Data are mean \pm SD. $N = 5$ replicates, 8 cells.

B Representative Hoxb8-derived dendritic cell (DC) approaching a path decision with equal pores sizes but one blocked path, frequently causing nucleokinesis from the blocked to the open path. The DC is stained with SPY-tubulin, which also visualizes the microtubule-organizing center (MTOC; in pink). The nucleus is visualized by Hoechst (cyan) and the cell shape is outlined in green. Projections of cellular (green), MTOC (pink) and nuclear (blue) paths are shown on the right. The configuration of the nucleus-MTOC axis is highlighted by dashed boxes (blue = nucleus forward; red = MTOC forward). Time in mins.

C As in (B), but using DCs that stably encode EMTB-mCherry, which visualizes the microtubule-organizing center.

D Manual quantification of the nucleus-MTOC axis configuration in EB3-mCherry expressing Hoxb8-derived dendritic cells before, during, and after nucleokinesis. The nucleus-MTOC axis configuration was assessed at the channel regions indicated by the red arrows. $N = 3$ replicates, 171 cells. Data are mean \pm SD.

E Manual quantification of the nucleus-MTOC axis configuration in SPY-tubulin stained Hoxb8-derived dendritic cells before, during, and after nucleokinesis. The nucleus-MTOC axis configuration was assessed at the channel regions indicated by the red arrows. $N = 3$ replicates, 126 cells. Data are mean \pm SD.

F Manual quantification of the nucleus-MTOC axis configuration in EMTB-mCherry expressing Hoxb8-derived dendritic cells before, during, and after nucleokinesis. The nucleus-MTOC axis configuration was assessed at the channel regions indicated by the red arrows. $N = 3$ replicates, 61 cells. Data are mean \pm SD.

Figure EV3. Amoeboid nucleokinesis remains largely unaffected when microtubules are depolymerized.

- A Heatmap of nuclear speed during amoeboid nucleokinesis in the presence of the microtubule inhibitor nocodazole (300 nM) or control (DMSO). The yellow-dotted regions 1 (DMSO) and 2 (Nocodazole) are enlarged to depict the cellular behavior during the initial nucleokinesis event. $N = 3$ replicates, 96 (DMSO) and 38 (Nocodazole) cells.
- B Quantification of nuclear speed during amoeboid nucleokinesis upon microtubule inhibition with 300 nM nocodazole (Nocod.): EMTB-mCherry expressing HoxB8-derived DCs, migrating through a path junction with one blocked path. The data show tracked nuclear velocities (visualized by Hoechst) of DCs that reposition their nucleus from the blocked to the open path by nucleokinesis. $N = 3$ replicates, 96 (DMSO) and 38 (Nocodazole), total analyzed events per column (from 1st to last column): 859, 417, 235, 45, 305, 145, 188, 58, 34, 23, 304, 149, 111, 81, 249, 46, 577, 505, 484, 97; mean \pm 95CI, Mann-Whitney test.
- C As in (A), but in the presence of 10 μ M nocodazole. $N = 4$ replicates, 71 (DMSO) and 48 (Nocodazole) cells.
- D As in (B), but in the presence of 10 μ M nocodazole. $N = 4$ replicates, 71 (DMSO) and 48 (Nocodazole) cells, total analyzed events per column (from 1st to last column): 1140, 671, 426, 292, 263, 231, 297, 180, 997, 768; mean \pm 95CI, Mann-Whitney test.
- E Heatmap of distance between nucleus and MTOC during amoeboid nucleokinesis in the presence of the microtubule inhibitor nocodazole (300 nM) or control (DMSO). The yellow-dotted regions 1 (DMSO) and 2 (Nocodazole) are enlarged to depict the cellular behavior during the initial nucleokinesis event. $N = 3$ replicates, 96 (DMSO) and 38 (Nocodazole) cells.
- F Distances between the MTOC and the nucleus during nucleokinesis in representative EMTB-mCherry expressing Hoxb8-derived dendritic cells in control (DMSO) and microtubule inhibited (300 nM nocodazole) samples. See (E) and (G) for quantification of the distance between MTOC and nucleus during the different phases of nucleokinesis. Some of the categories (MTOC in front in same channel parts) occurred rarely at the channel entrance, preventing representative images.
- G Quantification of the distance between nucleus and MTOC during amoeboid nucleokinesis upon microtubule inhibition with 300 nM nocodazole (Nocod.): EMTB-mCherry expressing HoxB8-derived DCs, migrating through a path junction with one blocked path. The data show the distances between the center of the nucleus (visualized by Hoechst) and the center of the MTOC (visualized by EMTB-mCherry) in DCs that reposition their nucleus from the blocked to the open path by nucleokinesis. The red dashed boxes highlight the reduced distance between nucleus and MTOC upon microtubule inhibition, when the MTOC is positioned frontward. $N = 3$ replicates, 96 (DMSO) and 38 (Nocodazole), total analyzed events per column (from 1st to last column): 859, 417, 237, 46, 305, 145, 188, 58, 34, 23, 304, 149, 111, 81, 249, 46, 578, 508, 484, 97; mean \pm 95CI; Mann-Whitney test.

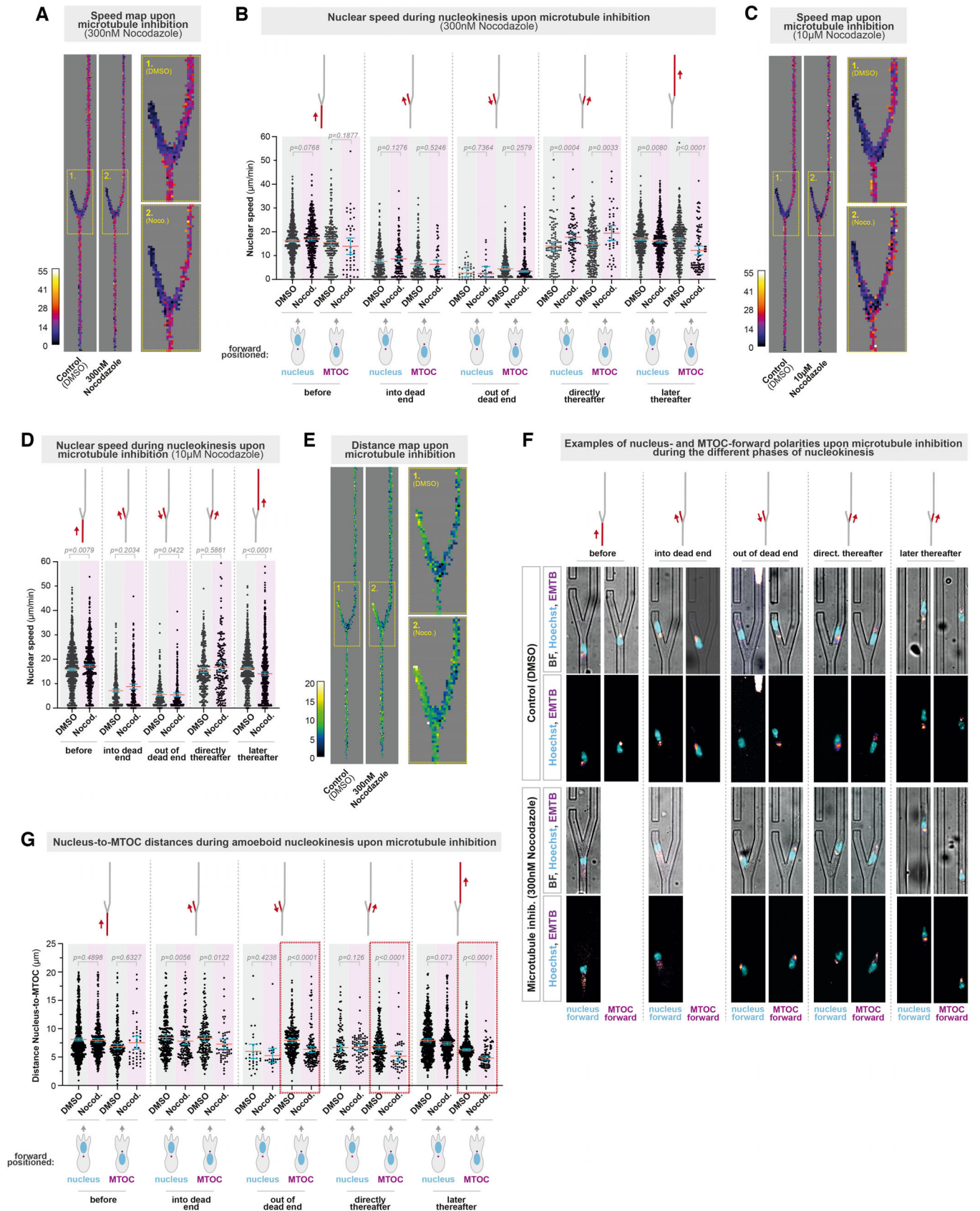


Figure EV3.

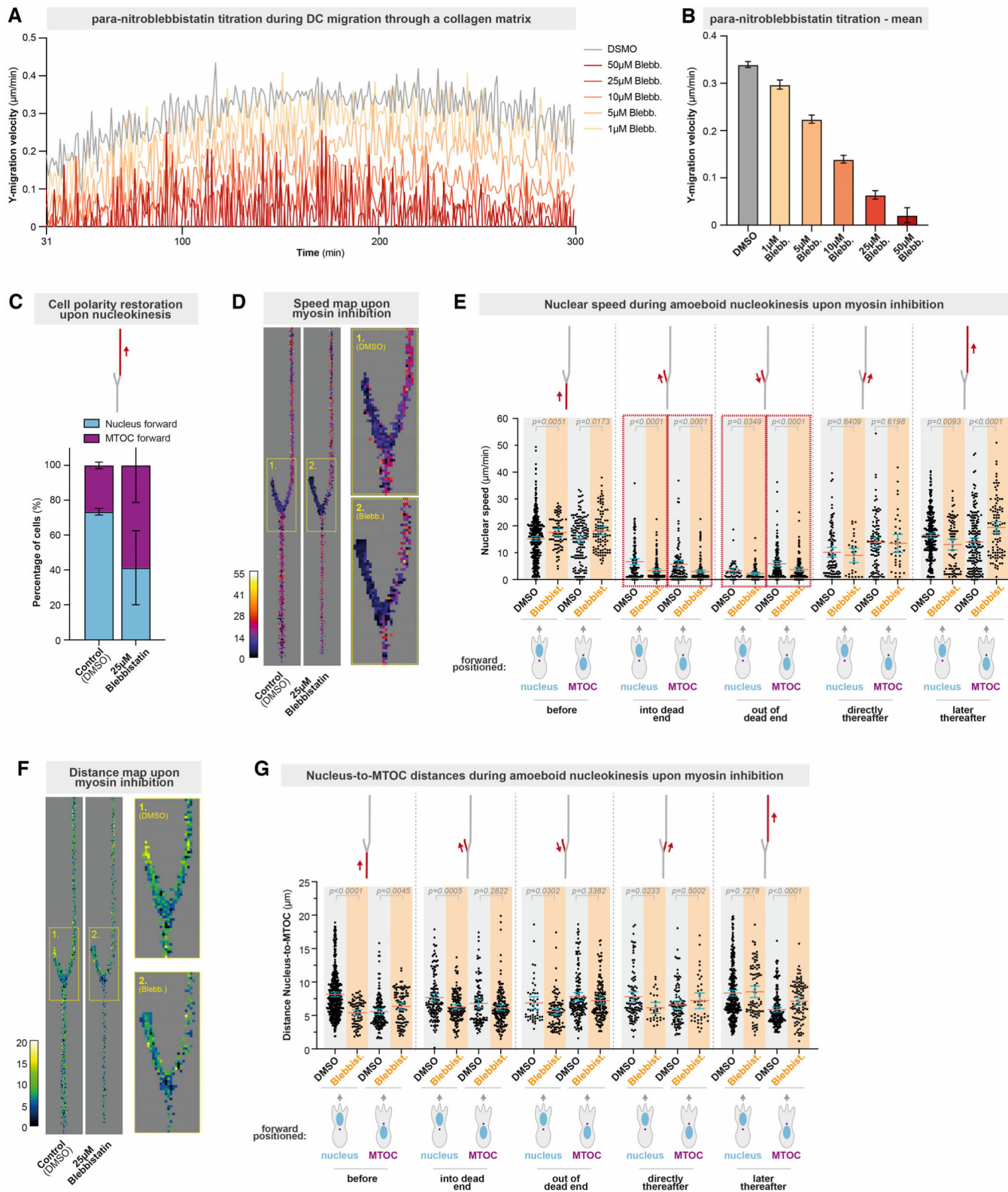


Figure EV4.

Figure EV4. Reduced amoeboid nucleokinesis speed and cell polarity switching upon myosin inhibition.

- A Bone marrow-derived dendritic cell migration in three-dimensional (3D) collagen matrices (3.3 mg/ml) along a CCL19 chemokine gradient in the presence of different concentrations of para-nitroblebbistatin (myosin inhibitor) or DMSO (control). $N = 3$ replicates. Data are mean.
- B Mean migration velocity between 150 and 250 min of cells shown in (A). $N = 3$ replicates. Data are mean \pm 95CI.
- C Quantification of the cell polarity after nucleokinesis at the channel exit in the presence of the myosin inhibitor para-nitroblebbistatin (25 μ M) or control (DMSO). $N = 4$ replicates, 37 (DMSO) and 13 (para-nitroblebbistatin) cells. Data are mean \pm SEM.
- D Heatmap of nuclear speed during amoeboid nucleokinesis in the presence of the myosin inhibitor para-nitroblebbistatin (25 μ M) or control (DMSO). The yellow-dotted regions 1 (DMSO) and 2 (para-nitroblebbistatin) are enlarged to depict the cellular behavior during the initial nucleokinesis event. $N = 4$ replicates, 37 (DMSO) and 13 (Blebbist.) cells.
- E Quantification of nuclear speed during amoeboid nucleokinesis upon myosin inhibition with 25 μ M para-nitroblebbistatin (Blebbist.): EB3-mCherry expressing HoxB8-derived DCs, migrating through a path junction with one blocked path. The data show tracked nuclear velocities (visualized by Hoechst) of DCs that reposition their nucleus from the blocked to the open path by nucleokinesis. The red dashed boxes highlight the decelerated nuclear speed upon myosin inhibition during repositioning of the nucleus from the blocked path. $N = 4$ replicates, 37 (DMSO) and 13 (Blebbist.) cells; total analyzed events per column (from 1st to last column): 433, 76, 146, 97, 139, 147, 107, 168, 48, 99, 150, 145, 101, 29, 107, 38, 330, 83, 184, 97; mean \pm 95CI, Mann-Whitney test.
- F Heatmap of distance between nucleus and MTOC during amoeboid nucleokinesis in the presence of the myosin inhibitor para-nitroblebbistatin (25 μ M) or control (DMSO). The yellow-dotted regions 1 (DMSO) and 2 (Blebbist.) are enlarged to depict the cellular behavior during the initial nucleokinesis event. $N = 4$ replicates, 37 (DMSO) and 13 (Blebbist.) cells.
- G Quantification of the distance between nucleus and MTOC during amoeboid nucleokinesis upon myosin inhibition with 25 μ M para-nitroblebbistatin (Blebbist.): EB3-mCherry expressing HoxB8-derived DCs, migrating through a path junction with one blocked path. The data show the distances between the center of the nucleus (visualized by Hoechst) and the center of the MTOC (visualized by EB3-mCherry) in DCs that reposition their nucleus from the blocked to the open path by nucleokinesis. $N = 4$ replicates, 37 (DMSO) and 13 (Blebbist.) cells, total analyzed events per column (from 1st to last column): 433, 76, 146, 97, 139, 147, 107, 168, 48, 99, 150, 145, 101, 29, 107, 38, 330, 83, 184, 97; mean \pm 95CI, Mann-Whitney test.

Figure EV5. Delayed cell polarity switching and amoeboid nucleokinesis upon low-dose actin inhibition.

- A Bone marrow-derived dendritic cell migration in three-dimensional (3D) collagen matrices (3.3 mg/ml) along a CCL19 chemokine gradient in the presence of different concentrations of Latrunculin A (actin inhibitor) or DMSO (control). $N = 3$ replicates. Data are mean.
- B Mean migration velocity between 150 and 250 min of cells shown in (A). $N = 3$ replicates. Data are mean \pm 95CI.
- C Heatmap of the nucleus-MTOC axis configuration during amoeboid nucleokinesis in the presence of the actin inhibitor Latrunculin A (50 nM) or control (DMSO). The yellow-dotted regions 1 (DMSO) and 2 (Latrunculin A) are enlarged to depict the cellular behavior during the initial nucleokinesis event, and the yellow-dotted regions 3 (DMSO) and 4 (Latrunculin A) are enlarged to depict the cellular behavior during the later nucleokinesis events to reposition the nucleus to the cellular front. $N = 3$ replicates, 78 (DMSO) and 67 (Latrunculin A) cells.
- D Quantification of the cell polarity after nucleokinesis at the channel exit in the presence of the actin inhibitor Latrunculin A (50 nM) or control (DMSO). $N = 3$ replicates, 78 (DMSO) and 66 (Latrunculin A) cells. Data are mean \pm SEM.
- E Quantification of the duration of nucleokinesis in the presence of the actin inhibitor Latrunculin A (50 nM) or control (DMSO). $N = 3$ replicates, 101 (DMSO) and 93 (Latrunculin A) cells. Data are mean \pm SEM.
- F Heatmap of nuclear speed during amoeboid nucleokinesis in the presence of the actin inhibitor Latrunculin A (50 nM) or control (DMSO). The yellow-dotted regions 1 (DMSO) and 2 (Latrunculin A) are enlarged to depict the cellular behavior during the initial nucleokinesis event. $N = 3$ replicates, 78 (DMSO) and 67 (Latrunculin A) cells.
- G Quantification of nuclear speed during amoeboid nucleokinesis upon actin inhibition with 50 nM Latrunculin A (Latr. A): EB3-mCherry expressing HoxB8-derived DCs, migrating through a path junction with one blocked path. The data show tracked nuclear velocities (visualized by Hoechst) of DCs that reposition their nucleus from the blocked to the open path by nucleokinesis. The red dashed boxes highlight the decelerated nuclear speed upon actin inhibition during repositioning of the nucleus from the blocked path. $N = 3$ replicates, 78 (DMSO) and 67 (Latr. A) cells, total analyzed events per column (from 1st to last column): 684, 444, 206, 413, 210, 204, 113, 147, 50, 48, 184, 217, 155, 119, 127, 209, 700, 434, 201, 465; data are mean \pm 95CI, Mann-Whitney test.
- H Heatmap of distance between nucleus and MTOC during amoeboid nucleokinesis in the presence of the actin inhibitor Latrunculin A (50 nM) or control (DMSO). The yellow-dotted regions 1 (DMSO) and 2 (Latr. A) are enlarged to depict the cellular behavior during the initial nucleokinesis event. $N = 3$ replicates, 78 (DMSO) and 67 (Latr. A) cells.
- I Quantification of the distance between nucleus and MTOC during amoeboid nucleokinesis upon actin inhibition with 50 nM Latrunculin A (Latr. A): EB3-mCherry expressing HoxB8-derived DCs, migrating through a path junction with one blocked path. The data show the distances between the center of the nucleus (visualized by Hoechst) and the center of the MTOC (visualized by EB3-mCherry) in DCs that reposition their nucleus from the blocked to the open path by nucleokinesis. $N = 3$ replicates, 78 (DMSO) and 67 (Latr. A) cells, total analyzed events per column (from 1st to last column): 684, 444, 206, 413, 210, 204, 113, 147, 50, 48, 184, 217, 155, 119, 127, 209, 700, 434, 201, 465; data are mean \pm 95CI, Mann-Whitney test.

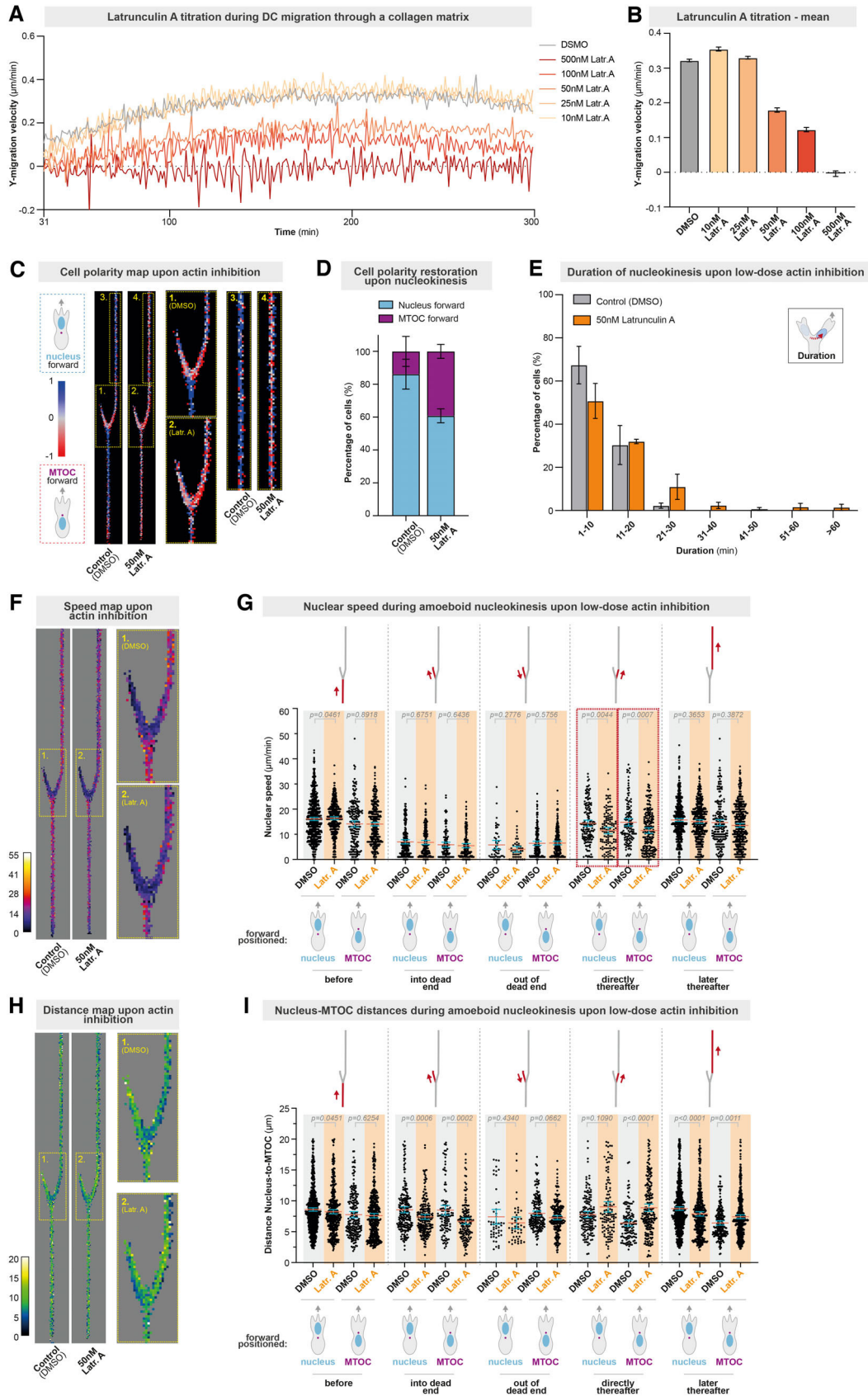


Figure EV5.

Author Query Form

Journal: EMBJ

Article: 2023114557

Dear Author,

During the copyediting of your manuscript the following queries arose.

Please refer to the query reference callout numbers in the page proofs and respond to each by marking the necessary comments using the PDF annotation tools.

Please remember illegible or unclear comments and corrections may delay publication.

Many thanks for your assistance.

AUTHOR: Please note that missing content in references have been updated where we have been able to match the missing elements without ambiguity against a standard citation database, to meet the reference style requirements of the journal. It is your responsibility to check and ensure that all listed references are complete and accurate.

Query reference	Query	Remarks
-----------------	-------	---------

APPENDIX

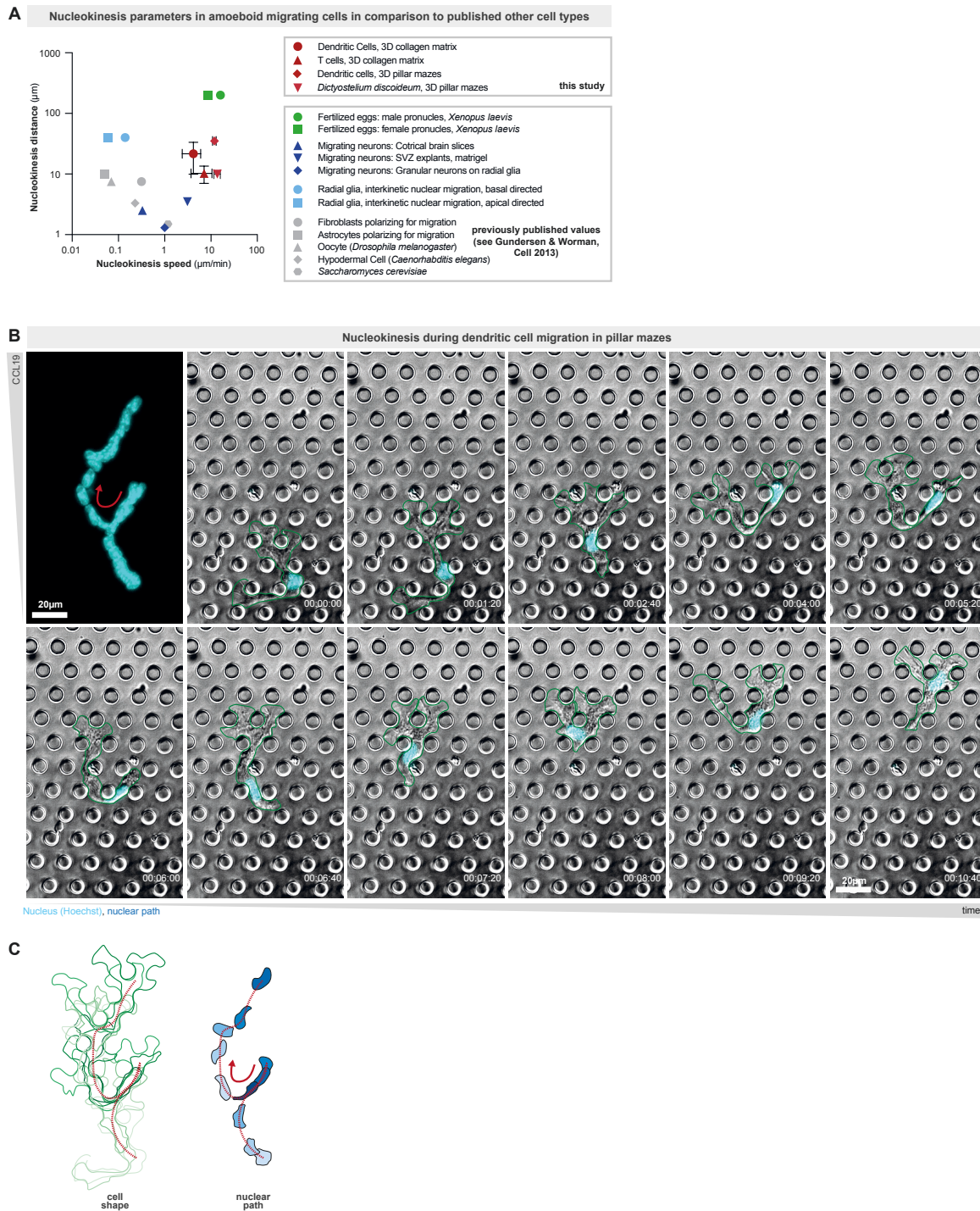
Adaptive Pathfinding by Nucleokinesis during Amoeboid Migration

Authors: Janina Kroll¹, Robert Hauschild², Artur Kuznetsov¹, Kasia Stefanowski¹, Monika D. Hermann¹, Jack Merrin², Lubuna Shafeek², Annette Müller-Taubenberger³, Jörg Renkawitz^{1*}

Table of Contents:

Appendix Figure S1.	Page 2
Figure legend for Appendix Figure S1.	Page 3
Appendix Figure S2.	Page 4
Figure legend for Appendix Figure S2.	Page 5
Appendix Figure S3.	Page 6
Figure legend for Appendix Figure S3.	Page 7
Appendix Figure S4.	Page 8
Figure legend for Appendix Figure S4.	Page 9
Appendix Figure S5.	Page 10
Figure legend for Appendix Figure S5.	Page 11
Appendix Figure S6.	Page 12
Figure legend for Appendix Figure S6.	Page 13
Appendix Figure S7.	Page 14
Figure legend for Appendix Figure S7.	Page 15

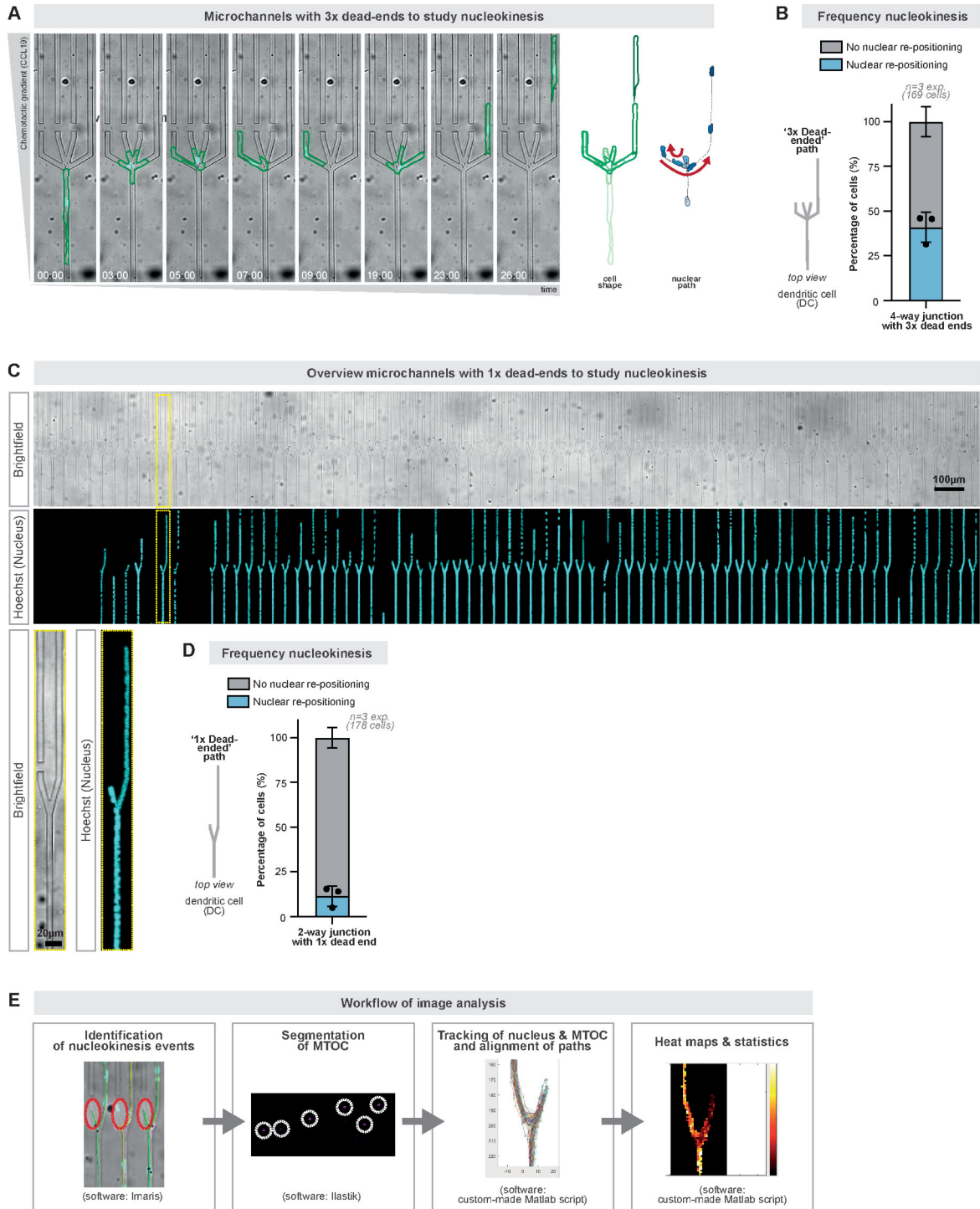
Appendix Figure S1. Comparison of amoeboid nucleokinesis parameters to nucleokinesis in other cell types.



Appendix Figure S1. Comparison of amoeboid nucleokinesis parameters to nucleokinesis in other cell types.

- A.** Speed and distance of amoeboid nucleokinesis in dendritic cells, T cells, and *Dictyostelium discoideum*. Previously published nucleokinesis speeds and distances measured in other cell types are shown as a reference (Gundersen & Worman, Cell 2013). Data from this study are mean \pm SD.
- B.** Representative bone marrow-derived dendritic cell (DC) migrating through a porous maze-like microenvironment composed of pillars interconnecting two surfaces below and above the migrating cell. The cell shape is outlined in green and the nucleus is visualized by Hoechst (cyan). Red arrow highlights nucleokinesis event. Time in hr:min:sec.
- C.** Time projections of the cellular and nuclear paths of the cell in B are shown in shades of green and blue, respectively. Red arrow highlights nucleokinesis event, and the red dashed line shows the nuclear path.

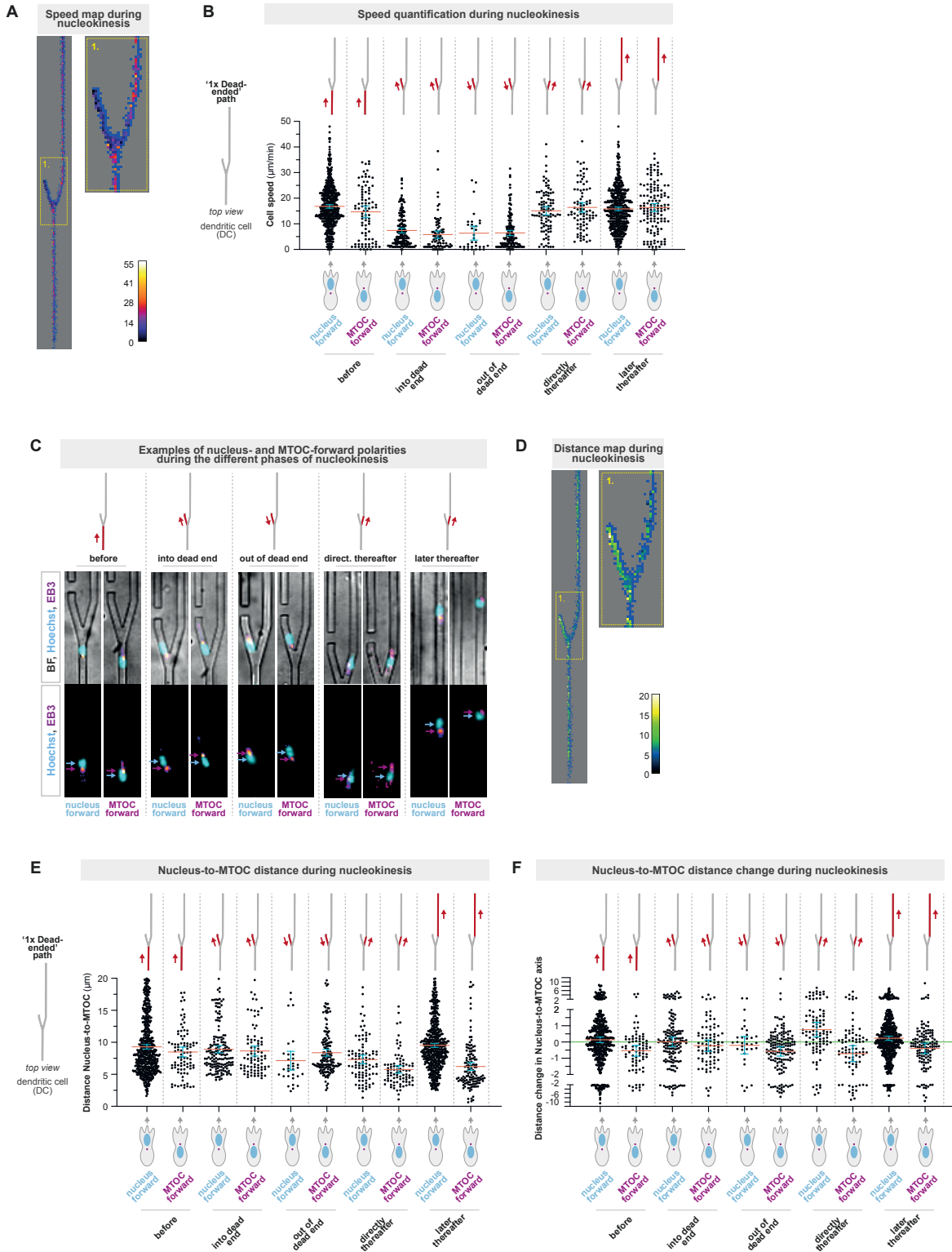
Appendix Figure S2. Novel reductionistic assay to characterize nucleokinesis during cell motility.



Appendix Figure S2. Novel reductionistic assays to characterize nucleokinesis during cell motility.

- A.** Representative bone marrow-derived DC (BMDC) migrating in a microchannel with a path junction that has one open and three blocked paths. Note the high frequency of nucleokinesis (nucleus in cyan; Hoechst) as quantified in B). To quantitatively analyze the detailed spatio-temporal dynamics of nucleokinesis, we analyzed nucleokinesis in even more simple environments, in which cells approach path junctions that are composed of one dead-end path and one open continuous path (see C and D). The cellular shape and the position of the nucleus are outlined over time in shades of green and blue, respectively. Time in min:sec.
- B.** Quantification of the rate of nucleokinesis in a 4-way junction with 3x dead ends. N=3 replicates, 169 cells. Data are mean \pm SD.
- C.** Overview of microchannels with 1x dead-end. Top: Brightfield, bottom: maximum projection of nuclear channel (Hoechst, cyan). The yellow-dotted regions are shown enlarged below.
- D.** Quantification of the rate of nucleokinesis in a 2-way junction with 1x dead end. N=3 replicates, 178 cells. Data are mean \pm SD.
- E.** Workflow of semi-automated image analysis for cells migrating in the 2-junction with 1x dead end. Nucleokinesis events are identified by only selecting nuclear tracks entering a surface drawn manually over the dead end in Imaris. Ilastik is used to segment the MTOC signal. Subsequently, the nucleus and MTOC are tracked in Imaris. Using a custom-made Matlab script, tracks are aligned and heat maps and data on track speed, distance of nucleus and MTOC, and distance changes are generated.

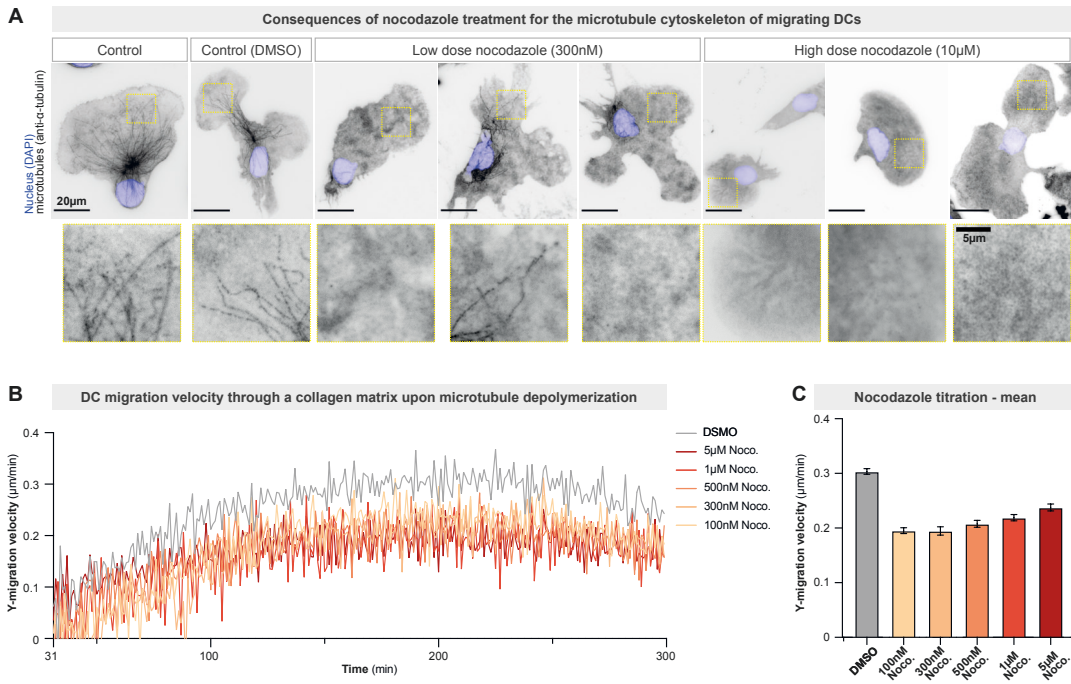
Appendix Figure S3. Nucleus-to-MTOC distances and speeds during amoeboid nucleokinesis.



Appendix Figure S3. Nucleus-to-MTOC distances and speeds during amoeboid nucleokinesis.

- A.** Heatmap of nuclear speed during amoeboid nucleokinesis. The yellow-dotted region 1 is enlarged to depict the cellular behavior during the initial nucleokinesis event. N=6 replicates, 48 cells.
- B.** Quantification of nuclear speed during amoeboid nucleokinesis depending on the nucleus-MTOC axis configuration: EB3-mCherry expressing HoxB8-derived DCs, migrating through a path junction with one blocked path. The data show tracked nuclear velocities (visualized by Hoechst) of DCs that reposition their nucleus from the blocked to the open path by nucleokinesis. N=6 replicates, N=48 cells, total analyzed events per column (from 1st to last column): 566, 90, 165, 85, 32, 159, 96, 85, 541, 136; Data are mean \pm 95CI.
- C.** Distances between the MTOC and the nucleus during nucleokinesis in representative EB3-mCherry expressing Hoxb8-derived dendritic cells. See D) and E) for quantification of the distance, and F) for quantification of the distance change during the different phases of nucleokinesis.
- D.** Heatmap of the distance between nucleus and MTOC during amoeboid nucleokinesis. The yellow-dotted region 1 is enlarged to depict the cellular behavior during the initial nucleokinesis event. N=6 replicates, 48 cells.
- E.** Quantification of the distance between nucleus and MTOC during amoeboid nucleokinesis depending on the nucleus-MTOC axis configuration: EB3-mCherry expressing HoxB8-derived DCs, migrating through a path junction with one blocked path. The data show the distances between the center of the nucleus (visualized by Hoechst) and the center of the MTOC (visualized by EB3-mCherry) in DCs that reposition their nucleus from the blocked to the open path by nucleokinesis. N=6 replicates, N=48 cells, total analyzed events per column (from 1st to last column): 566, 90, 165, 85, 32, 159, 96, 85, 541, 136; Data are mean \pm 95CI.
- F.** Quantification of the nucleus-to-MTOC distance changes during amoeboid nucleokinesis depending on the nucleus-MTOC axis configuration: EB3-mCherry expressing HoxB8-derived DCs, migrating through a path junction with one blocked path. The data show the change of distances between the center of the nucleus (visualized by Hoechst) and the center of the MTOC (visualized by EB3-mCherry) in DCs that reposition their nucleus from the blocked to the open path by nucleokinesis. N=6 replicates, N=48 cells, total analyzed events per column (from 1st to last column): 566, 90, 165, 85, 32, 159, 96, 85, 541, 136; Data are mean \pm 95CI.

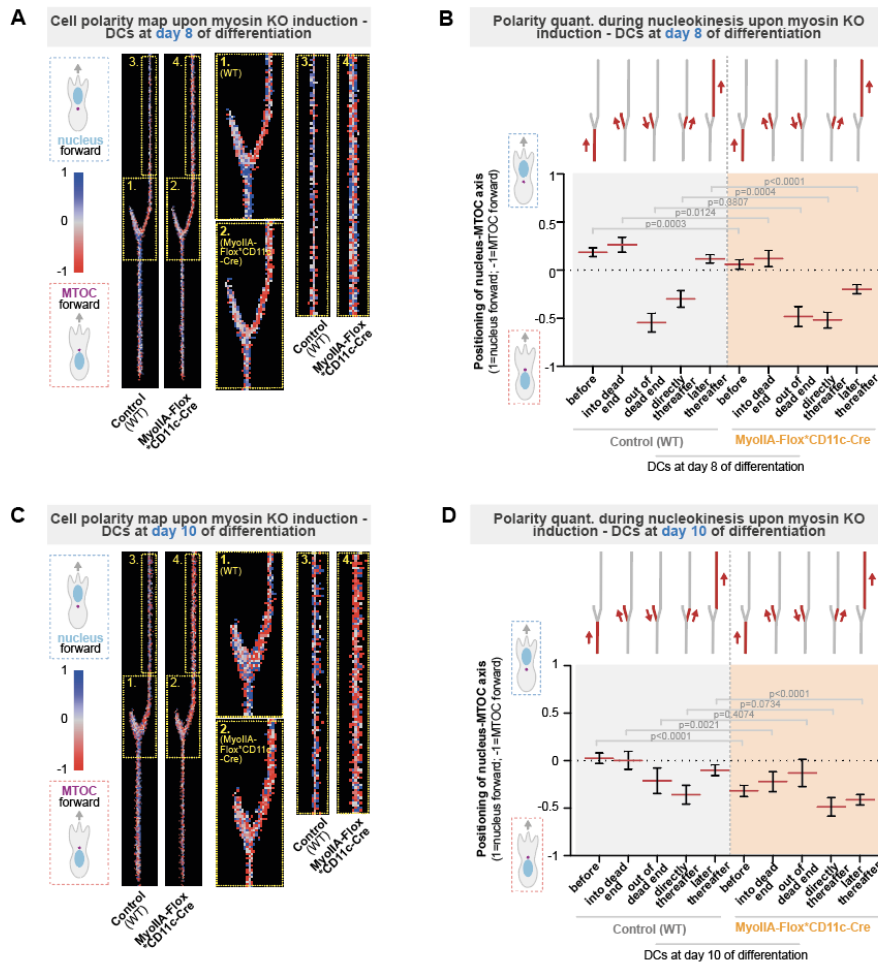
Appendix Figure S4. Consequences of low and high doses of nocodazole for the microtubule cytoskeleton and the velocity of migratory dendritic cells



Appendix Figure S4. Consequences of low and high doses of nocodazole for the microtubule cytoskeleton and the velocity of migrating cells.

- A.** Immunofluorescence staining against alpha-tubulin (black) of DCs migrating in an under-agarose assay (Nucleus/DAPI shown in blue). Note that microtubules typically reach far-distantly into at least one cellular protrusion in control cells (dashed yellow boxes show regions in the protrusions in an enlarged manner), whereas low doses of 300 nM nocodazole largely depolymerize the microtubule cytoskeleton in most cells, and high doses of 10 μ M nocodazole entirely depolymerize the microtubule cytoskeleton.
- B.** Bone marrow-derived dendritic cell migration in three-dimensional (3D) collagen matrices (3.3 mg/ml) along a CCL19 chemokine gradient in the presence of different concentrations of Nocodazole (microtubule inhibitor) or DMSO (control). N=3 replicates. Data are mean.
- C.** Mean migration velocity between 150 and 250 min of cells shown in A. N=3 replicates. Data are mean \pm 95CI.

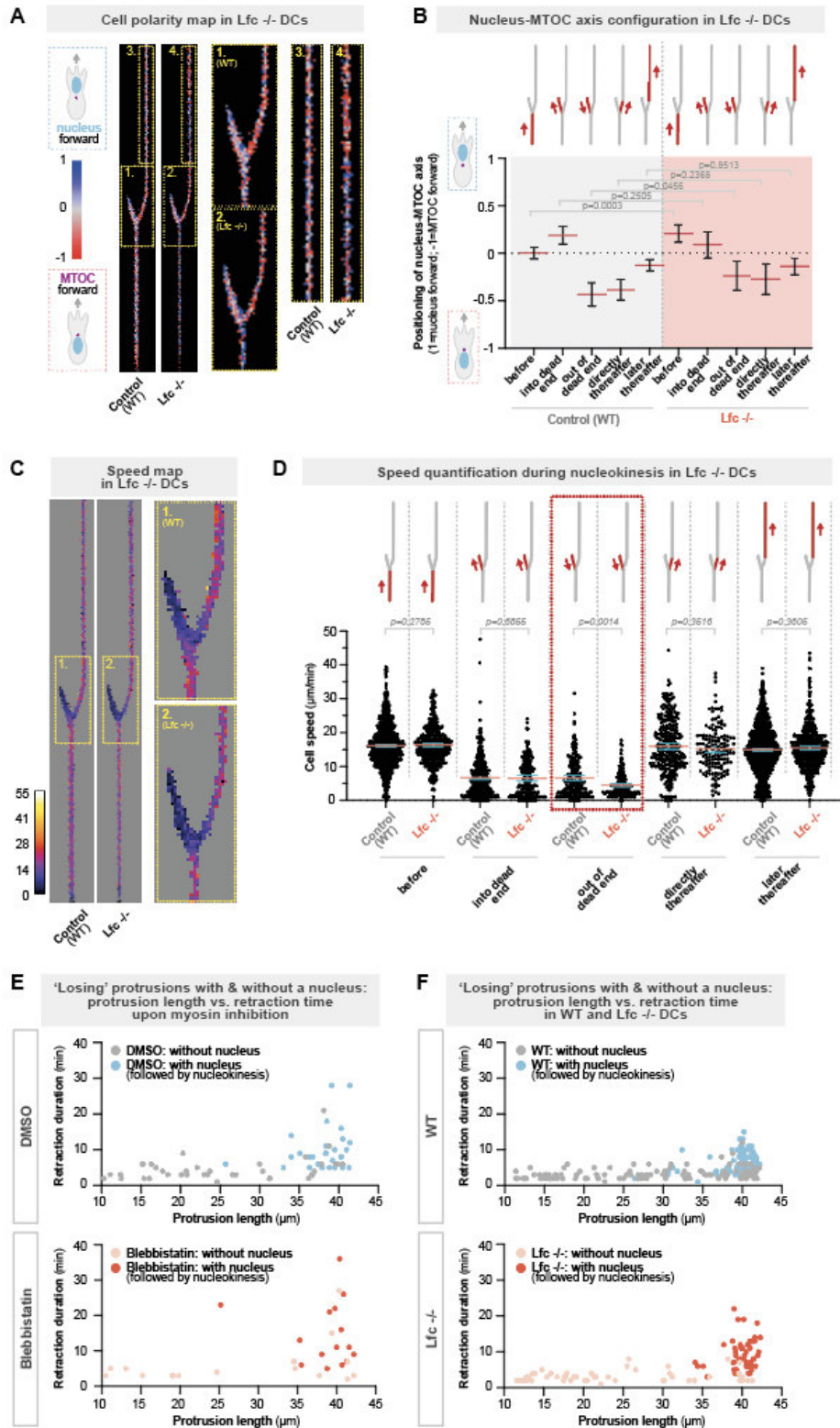
Appendix Figure S5. Reduced cell polarity switching during amoeboid nucleokinesis upon myosin-IIA knockout.



Appendix Figure S5. Reduced cell polarity switching during amoeboid nucleokinesis upon a conditional myosin-IIA knockout.

- A.** Heatmap of the nucleus-MTOC axis configuration during amoeboid nucleokinesis in myosin-IIA KO or control DCs at day 8 of differentiation. The yellow-dotted regions 1 (WT) and 2 (myosin KO) are enlarged to depict the cellular behavior during the initial nucleokinesis event, and the yellow-dotted regions 3 (WT) and 4 (myosin KO) are enlarged to depict the cellular behavior during the later nucleokinesis events to reposition the nucleus to the cellular front. N=3 replicates, 119 (WT) and 94 (myosin KO) cells.
- B.** Quantification of the nucleus-MTOC axis configuration before, during, directly after, and later after amoeboid nucleokinesis in myosin-IIA KO or control DCs at day 8 of differentiation (1=all cells position the nucleus in front of the MTOC; -1= all cells position the MTOC in front of the nucleus). Data are mean \pm 95CI, Mann-Whitney test, N=3 replicates, 119 (control) and 94 (myosin KO) cells, and 1813 (before; control), 1511 (before; KO), 617 (into a dead end, control), 555 (into a dead end, KO), 286 (out of a dead end, control), 282 (out of a dead end, KO), 468 (directly thereafter, control), 411 (directly thereafter, KO), 1953 (later thereafter, control), and 1700 (later thereafter, KO) image frames.
- C.** Heatmap of the nucleus-MTOC axis configuration during amoeboid nucleokinesis in myosin-IIA KO or control DCs at day 10 of differentiation. The yellow-dotted regions 1 (WT) and 2 (myosin KO) are enlarged to depict the cellular behavior during the initial nucleokinesis event, and the yellow-dotted regions 3 (WT) and 4 (myosin KO) are enlarged to depict the cellular behavior during the later nucleokinesis events to reposition the nucleus to the cellular front. N= 3 replicates, 92 (WT) and 49 (myosin KO) cells.
- D.** Quantification of the nucleus-MTOC axis configuration before, during, directly after, and later after amoeboid nucleokinesis in myosin-IIA KO or control DCs at day 10 of differentiation (1=all cells position the nucleus in front of the MTOC; -1= all cells position the MTOC in front of the nucleus). Data are mean \pm 95CI, Mann-Whitney test, N=3 replicates, 92 (control) and 49 (myosin KO) cells, and 1294 (before; control), 1000 (before; KO), 441 (into a dead end, control), 331 (into a dead end, KO), 208 (out of a dead end, control), 186 (out of a dead end, KO), 346 (directly thereafter, control), 311 (directly thereafter, KO), 1233 (later thereafter, control), and 1056 (later thereafter, KO) image frames.

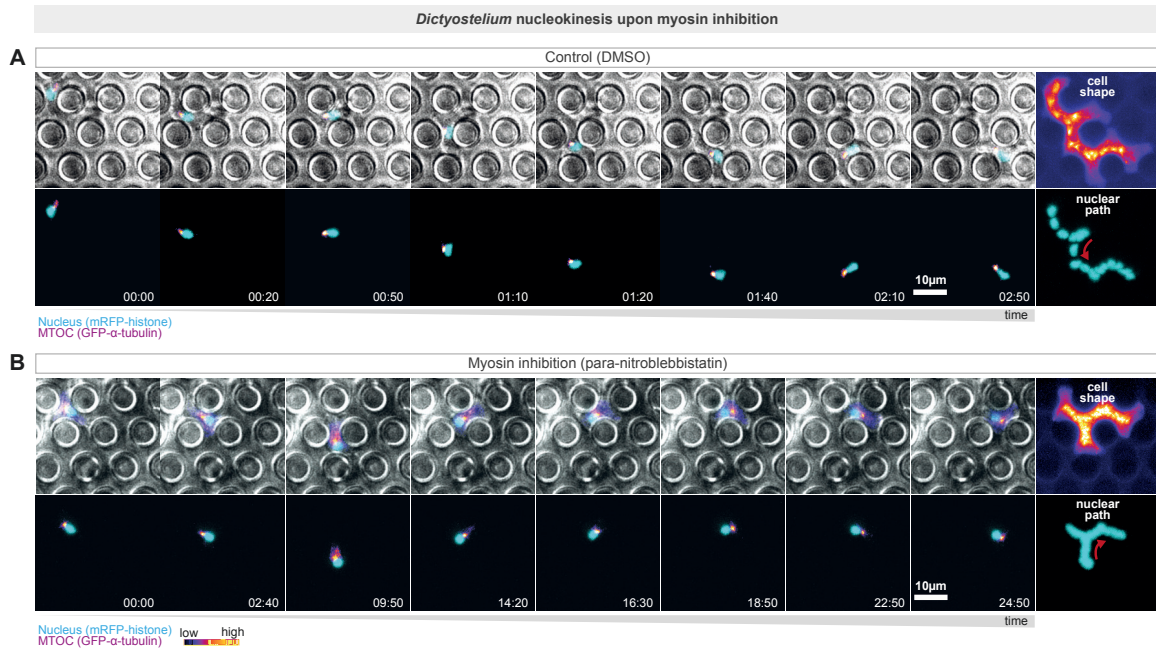
Appendix Figure S6. Slower retractions of nucleus-containing protrusions in *Lfc* knockout DCs.



Appendix Figure S6. Slower retractions of nucleus-containing protrusions in *Lfc* ^{-/-} DCs.

- A.** Comparable nucleus-MTOC axis configuration in *Lfc* knockout cells to WT cells during amoeboid nucleokinesis: the MTOC was visualized by spy-tubulin; Data shows heatmaps of the nucleus-MTOC axis configuration during amoeboid nucleokinesis in WT and *Lfc* ^{-/-} DCs. The yellow-dotted regions 1 (WT) and 2 (*Lfc* ^{-/-}) are enlarged to depict the cellular behavior during the initial nucleokinesis event, and the yellow-dotted regions 3 (WT) and 4 (*Lfc* ^{-/-}) are enlarged to depict the cellular behavior during the later nucleokinesis events to reposition the nucleus to the cellular front. N=4 replicates, 105 (WT) and 42 (*Lfc* ^{-/-}) cells.
- B.** Quantification of A) of the nucleus-MTOC axis configuration before, during, directly after, and later after amoeboid nucleokinesis in *Lfc* ^{-/-} or WT cells (1=all cells position the nucleus in front of the MTOC; -1= all cells position the MTOC in front of the nucleus). Data are mean±95CI, Mann-Whitney test, N=4 replicates, 105 (WT) and 42 (*Lfc* ^{-/-}) cells, and 1029 (before; WT), 439 (before; *Lfc* ^{-/-}), 424 (into a dead end, WT), 198 (into a dead end, *Lfc* ^{-/-}), 212 (out of a dead end, WT), 160 (out of a dead end, *Lfc* ^{-/-}), 290 (directly thereafter, WT), 143 (directly thereafter, *Lfc* ^{-/-}), 1084 (later thereafter, WT), and 480 (later thereafter, *Lfc* ^{-/-}) image frames.
- C.** Heatmap of nuclear speed during amoeboid nucleokinesis in *Lfc* ^{-/-} or WT cells. The yellow-dotted regions 1 (WT) and 2 (*Lfc* ^{-/-}) are enlarged to depict the cellular behavior during the initial nucleokinesis event. N= 4 replicates, 105 (WT) and 42 (*Lfc* ^{-/-}) cells.
- D.** Quantification of C) of the nuclear speed during amoeboid nucleokinesis in *Lfc* ^{-/-} or WT cells. N= 4 replicates, 113 (WT) and 52 (*Lfc* ^{-/-}) cells, total analyzed events per column are 1029 (before; WT), 439 (before; *Lfc* ^{-/-}), 424 (into a dead end, WT), 198 (into a dead end, *Lfc* ^{-/-}), 212 (out of a dead end, WT), 160 (out of a dead end, *Lfc* ^{-/-}), 290 (directly thereafter, WT), 143 (directly thereafter, *Lfc* ^{-/-}), 1084 (later thereafter, WT), and 480 (later thereafter, *Lfc* ^{-/-}); data are mean±95CI, Mann-Whitney test.
- E.** Correlating the retraction time of ‘losing’ protrusions vs their length, comparing ‘losing’ protrusions without a nucleus and with a nucleus upon myosin inhibition by para-nitroblebbistatin vs controls (DMSO). N= 5 replicates, 38 cells (DMSO, without nucleus), 29 (DMSO, with nucleus), 17 cells (blebbistatin, without nucleus) and 29 cells (blebbistatin, with nucleus). See also main figure 5E for quantification of retraction times of ‘losing’ protrusions with and without a nucleus upon myosin inhibition.
- F.** Correlating the retraction time of ‘losing’ protrusions vs their length, comparing ‘losing’ protrusions without a nucleus and with a nucleus in WT and *Lfc* ^{-/-} DCs. N= 4 replicates, 113 cells (WT, without nucleus), 113 (WT, with nucleus), 52 cells (*Lfc* ^{-/-}, without nucleus) and 52 cells (*Lfc* ^{-/-}, with nucleus). See also main figure 5F for quantification of retraction times of ‘losing’ protrusions with and without a nucleus in *Lfc* ^{-/-} DCs.

Appendix Figure S7. Delayed nucleokinesis upon myosin inhibition in *Dictyostelium*.



Appendix Figure S7. Delayed nucleokinesis upon myosin inhibition in *Dictyostelium*.

- A.** Representative *Dictyostelium* cell (control: DMSO) migrating in a pillar maze. The *Dictyostelium* cell stably encodes GFP- α -tubulin, which also visualizes the microtubule-organizing center (MTOC; in pink) and mRFP-histone, which visualizes the nucleus (in cyan). Projections of cellular (fire) and nuclear (blue) paths are shown on the right. The red arrow highlights the nucleokinesis event. Time in min:sec.
- B.** Representative *Dictyostelium* cell migrating in a pillar maze upon myosin inhibition (25 μ M para-nitroblebbistatin). The *Dictyostelium* cell stably encodes GFP- α -tubulin, which also visualizes the microtubule-organizing center (MTOC; in pink) and mRFP-histone, which visualizes the nucleus (in cyan). Projections of cellular (fire) and nuclear (blue) paths are shown on the right. The red arrow highlights the nucleokinesis event. Time in min:sec.

4. Paper II: Centrosome Positioning in Migrating *Dictyostelium* Cells

Hellen Ishikawa-Ankerhold^{1,2}, Janina Kroll³, Dominic van den Heuvel^{1,2}, Jörg Renkawitz³, Annette Müller-Taubenberger⁴

¹ Department of Internal Medicine I, University Hospital, Faculty of Medicine, LMU Munich; Munich, Germany

² Walter-Brendel-Centre of Experimental Medicine, University Hospital, Faculty of Medicine, LMU Munich; Munich, Germany

³ Biomedical Center Munich (BMC), Department of Cardiovascular Physiology and Pathophysiology, Walter-Brendel-Centre of Experimental Medicine, University Hospital, Faculty of Medicine, LMU Munich; Planegg-Martinsried, Germany




⁴ Biomedical Center Munich (BMC), Department of Cell Biology (Anatomy III), Faculty of Medicine, LMU Munich; Planegg-Martinsried, Germany

This article was published in *Cells* 2022, 11, 1776.

DOI: <https://doi.org/10.3390/cells11111776>

I performed all microchannel and -pillar assays shown in Figure 1, Figure 4, Figure S1a-f and Figure S2. I did the analysis for the data shown in Figure S1a-e and Figure S2. I contributed to writing parts of the Materials and Methods Section and parts of the Figure Legends. Additionally, I assisted with reviewing and editing of the draft.

Centrosome Positioning in Migrating *Dictyostelium* Cells

Hellen Ishikawa-Ankerhold ^{1,2} , Janina Kroll ³, Dominic van den Heuvel ^{1,2}, Jörg Renkawitz ³ 
and Annette Müller-Taubenberger ^{4,*} 

¹ Department of Internal Medicine I, University Hospital, Faculty of Medicine, LMU Munich, 81377 Munich, Germany; hellen.ishikawa-ankerhold@med.uni-muenchen.de (H.I.-A.); dominic.van@med.uni-muenchen.de (D.v.d.H.)

² Walter-Brendel-Centre of Experimental Medicine, University Hospital, Faculty of Medicine, LMU Munich, 81377 Munich, Germany

³ Biomedical Center Munich (BMC), Department of Cardiovascular Physiology and Pathophysiology, Walter-Brendel-Centre of Experimental Medicine, University Hospital, Faculty of Medicine, LMU Munich, 82152 Planegg-Martinsried, Germany; janina.kroll@med.uni-muenchen.de (J.K.); joerg.renkawitz@med.uni-muenchen.de (J.R.)

⁴ Biomedical Center Munich (BMC), Department of Cell Biology (Anatomy III), Faculty of Medicine, LMU Munich, 82152 Planegg-Martinsried, Germany

* Correspondence: amueller@bmc.med.lmu.de; Tel.: +49-89-2180-75873

Abstract: Directional cell migration and the establishment of polarity play an important role in development, wound healing, and host cell defense. While actin polymerization provides the driving force at the cell front, the microtubule network assumes a regulatory function, in coordinating front protrusion and rear retraction. By using *Dictyostelium discoideum* cells as a model for amoeboid movement in different 2D and 3D environments, the position of the centrosome relative to the nucleus was analyzed using live-cell microscopy. Our results showed that the centrosome was preferentially located rearward of the nucleus under all conditions tested for directed migration, while the nucleus was oriented toward the expanding front. When cells are hindered from straight movement by obstacles, the centrosome is displaced temporarily from its rearward location to the side of the nucleus, but is reoriented within seconds. This relocalization is supported by the presence of intact microtubules and their contact with the cortex. The data suggest that the centrosome is responsible for coordinating microtubules with respect to the nucleus. In summary, we have analyzed the orientation of the centrosome during different modes of migration in an amoeboid model and present evidence that the basic principles of centrosome positioning and movement are conserved between *Dictyostelium* and human leukocytes.

Keywords: amoeboid cell migration; cAMP; chemotaxis; *Dictyostelium discoideum*; folate; microchannels; micropipette assay; microtubules; 3D matrix



Citation: Ishikawa-Ankerhold, H.; Kroll, J.; Heuvel, D.v.d.; Renkawitz, J.; Müller-Taubenberger, A. Centrosome Positioning in Migrating *Dictyostelium* Cells. *Cells* **2022**, *11*, 1776. <https://doi.org/10.3390/cells11111776>

Academic Editor: Ricardo Escalante

Received: 12 April 2022

Accepted: 26 May 2022

Published: 29 May 2022

Publisher's Note: MDPI stays neutral with regard to jurisdictional claims in published maps and institutional affiliations.



Copyright: © 2022 by the authors. Licensee MDPI, Basel, Switzerland. This article is an open access article distributed under the terms and conditions of the Creative Commons Attribution (CC BY) license (<https://creativecommons.org/licenses/by/4.0/>).

1. Introduction

Cell migration is a complex process and, as such, important for morphogenesis during embryonic development, wound healing, or immune responses. Mechanistically, different types of cell movement can be distinguished: amoeboid, mesenchymal, multicellular streaming, and collective cell migration [1]. Migrating cells are usually characterized by polarity, recognizable by the extension of protrusions at the front or leading edge and retraction of the rear end [2,3].

Individual cells, such as fibroblasts, myoblasts, neural crest cells, and various cancer cells have been shown to migrate in the mesenchymal migration mode, which is characterized by a strong adhesive capacity, mediated by focal adhesions and proteolytic degradation of the surrounding extracellular matrix during interstitial movement. These cells exhibit a rather low migration speed.

In contrast, leukocytes, including neutrophils, T-cells, and dendritic cells, and cells of the model organism *Dictyostelium discoideum* display an amoeboid mode of migration that is characterized by a lack of focal adhesions and stress fibers [4–6]. These cells are rather poorly adhesive, migrate with considerably higher speed, and do not perform proteolytic remodeling of their surrounding matrix when migrating in three-dimensional (3D) environments. Depending on the mechanical constraints, amoeboid cells can switch between F-actin-driven and bleb-based pseudopod formation [1,7–10]. Recent work has shown that both forms of surface extensions can coexist and cooperate during chemotaxis [11,12].

For many years *Dictyostelium* has been used to explore basic principles in cell and developmental biology, and more recently it has emerged as a valuable biomedical model system for studying several human diseases [13,14]. *Dictyostelium* cells are intrinsically motile and serve as an excellent model to analyze cell motility and host defense [13,15,16]. Single *Dictyostelium* cells, just like leukocytes, migrate either randomly or perform directed movement when sensing chemical cues in their microenvironment. During chemotactic migration, the gradient of the extracellular chemoattractant is sensed by the cells through G-protein coupled receptors and transduced into an intracellular signaling cascade, which allows the establishment of cell polarity, expansion of pseudopods, and migration of the cells [17–20]. Depending on the life cycle phase, either folic acid or cyclic AMP can act as chemoattractant for *Dictyostelium*. *Dictyostelium* cells are professional phagocytes that, in their vegetative growth phase, sense bacteria by chemotaxis toward folic acid and ingest them by phagocytosis [21]. Chemotaxis toward the cAMP released by cells is important for development into fruiting bodies [22]. The cAMP receptor, cAR1, was the first chemoattractant G-protein coupled receptor identified in eukaryotic cells [23], whereas the G-protein-coupled receptor for folic acid-mediated signaling was identified more recently [24].

Microtubules are important cytoskeletal structures, essential for cell division, intracellular transport, motion of cilia and flagella, as well as cell migration and establishment of polarity [25]. How microtubules are involved in the mechanism of migration is not yet fully understood and largely depends on the cell type. Most studies have concluded that microtubules play a positive role, by regulating actin polymerization, transporting membrane vesicles to the leading edge, and/or facilitating the turnover of adhesion plaques. Several studies have shown that microtubules regulate cell migration in a cell type-dependent manner [26,27]. To give a few examples, it was shown that their depolymerization can impair cell migration in types of cells such as fibroblasts [26,28], and suppress the polarity and promote motility of neutrophils [29], while their absence had no influence on the migratory properties of fish keratinocytes [30]. In addition, microtubules have been reported to restrain cell movement and to specify directionality [31]. For immune cells, the role of the microtubule cytoskeleton and its importance in cell polarization and directed migration has been recently reviewed [32].

Microtubules nucleate either from basal bodies or microtubule organizing centers (MTOCs). Centrosomes are the major MTOCs, and during migration, their intracellular position seems to depend on the cell type. In slow-moving non-leukocyte cells, the MTOC is often located in front of the nucleus (relative to the direction of cell migration) and microtubules radiate primarily towards the leading edge [33,34]. Similarly, in slow-moving macrophages, the MTOC often locates in front of the nucleus [35,36]. However, in fast-moving leukocytes, such as dendritic cells and T-cells, MTOCs and microtubules have been described to localize behind the nucleus during directional migration [36–39]. This positioning of the nucleus, frontward to the centrosome, enables these fast-migrating cells to use their nucleus as a mechanical gauge to probe for suitable larger pores in the microenvironment [39]. However, in fast migrating neutrophils, the MTOC frequently localizes between the lobes of the segmented nucleus [39–41], but also has been reported to either localize to the back of the nucleus during polarization on 2D surfaces [39], or to localize to the front of the nucleus during migration in living zebrafish [27], suggesting that MTOC positioning might also be influenced by the cellular microenvironment.

The *Dictyostelium* centrosome has been explored in detail in recent years [42,43]. It is structurally different, as it contains no centrioles and shows some differences with respect to centrosome duplication and its regulation. In the interphase, the *Dictyostelium* centrosome remains adjacent to the nucleus, and several proteins have been demonstrated to play a role in connecting centrosomes to nuclei, including a Sun1 homolog [44,45], a centrin B homolog [46], the centrosomal protein CP148 [47], and the kinesin Kif9 [48]. They play either a structural or regulatory role in anchoring microtubule minus ends into the centrosome corona or in linking components at the nuclear envelope [43,48].

In the present study, we investigated the position of the centrosome relative to that of the nucleus, and the proximity of the centrosome to the nucleus during migration of *Dictyostelium* single cells. Although several studies have addressed the position of the centrosome in the past [49–54], a systematic investigation considering different migration conditions has been lacking. Here, we used microfabricated polydimethylsiloxane (PDMS) surfaces and 3D matrices, in addition to standard chemotaxis micropipette assays, to systematically test centrosome positioning in diverse microenvironments and different developmental stages.

2. Materials and Methods

2.1. Cells and Culture Conditions

Cells of the *Dictyostelium discoideum* strain AX2-214 expressing both GFP- α -tubulin (tubA1; DDB0191380 | DDB_G0287689) [52] and mRFP-histone (H2Bv3; DDB0231622 | DDB_G0286509) [55] were cultivated in polystyrene Petri dishes in HL5 medium (Formedium, Hunstanton, Norfolk, UK) supplemented with 20 μ g/mL of Geneticin (Sigma-Aldrich, Sigma-Aldrich Chemie GmbH, Taufkirchen, Germany) and 10 μ g/mL of Blasticidin S (Gibco, Fisher Scientific GmbH, Schwerte, Germany) at 22 °C. To induce aggregation competence and development, cells were washed in phosphate buffer (PB; 17 mM phosphate, pH 6.0), and starved in PB for 8 to 10 h.

2.2. Chemotaxis Conditions

For chemotaxis of growth phase cells versus pterines, a final concentration of 100 μ M folate (Sigma-Aldrich; F8758) was used to set up the gradient in PDMS microfabricated or 3D μ -slide chemotaxis devices (ibidi GmbH, Gräfelfing, Germany) with a VitroGel Hydrogel matrix (TheWell Bioscience Inc., North Brunswick, NJ, USA). For chemotaxis experiments with cells during the aggregation competent stage, cAMP (Sigma-Aldrich; A9501) was used at a final concentration of 10 μ M in micropipette assays, PDMS microfabricated devices, and 3D μ -slide chemotaxis devices (ibidi GmbH, Gräfelfing, Germany) with VitroGel Hydrogel (TheWell Bioscience Inc., North Brunswick, NJ, USA) or rat collagen type I (ibidi GmbH, Gräfelfing, Germany) matrices.

2.3. Micropipette Chemotaxis Assay

For analysis of cell motility in 2D conditions, starved cells or cells treated with 30 μ M of nocodazole for 1 h, were plated in low 35-mm standard-bottom μ -dishes (ibidi GmbH, Gräfelfing, Germany), and migration toward a micropipette (Eppendorf) filled with 10 μ M cyclic AMP was recorded using a confocal laser scanning microscope (LSM 780, Zeiss) with a Plan-Apochromat 63x/1.4 Oil DIC objective. Images were taken at 1.5 s intervals for 30–60 min. Centrosome and nucleus displacement were tracked using the automatic ImarisTrack tool of the Imaris software (Bitplane), followed by manual cell tracking.

2.4. Migration within Microfabricated Polydimethylsiloxane (PDMS)-Based Microchannels or Pillar Arrays

Dictyostelium cells expressing both GFP-tubulin and mRFP-histone were propagated in the growth phase, or the developmental phase as described above (2.1.). Microfabricated PDMS microchannels (8 μ m width, 4.8 μ m height) or pillar arrays (micropillars with a diameter of 7 μ m, positioned with a distance of 10 μ m, and a height of 4.2 μ m to

connect the bottom glass-slide with the PDMS-composed ceiling) were used, as previously described [56,57]. To investigate the chemotaxis of *Dictyostelium* cells in the growth phase, we loaded 100,000 cells and employed a final concentration of 100 μM folate (Sigma-Aldrich, F8758) to set up the gradient. To analyze the chemotactic migration of cells of the developmental stage, 50,000 cells were loaded and 10 μM of cAMP was used to generate the chemoattractant gradient.

2.5. Migration in 3D Hydrogel and Collagen Matrices

To analyze the position of the centrosome in relation to the nucleus during migration in 3D environments, 3D μ -slide chemotaxis devices (ibidi GmbH, Gräfelfing, Germany) were used in combination either with VitroGel Hydrogel (TheWell Bioscience) or rat collagen type I (ibidi GmbH, Gräfelfing, Germany) matrices.

Hydrogel: 100,000 *Dictyostelium* cells of the developmental phase were suspended in PB and mixed with hydrogel (*v/v* 1:2), loaded into a 3D μ -slide chemotaxis chamber (6 μL into the middle channel), and were allowed to settle down for 1 h at RT. To set up a gradient of cAMP, a final concentration of 10 μM cAMP was loaded (65 μL) into one outer compartment of the chamber, the other one was filled with PB (65 μL).

Collagen: 100,000 *Dictyostelium* cells of the developmental stage were suspended in a final volume of 75 μL containing rat tail collagen type I (ibidi GmbH, Gräfelfing, Germany; 1.5 mg/mL) in PB supplemented with 6.7 mM NaOH, 1.2 mM CaCl_2 , and 0.2% NaHCO_3 . The cell–collagen mix was loaded into the 3D μ -slide chemotaxis chamber (6 μL into the middle channel), and was allowed to settle down for 30 min at RT for polymerization [58]. Then, 100 nM cAMP was added to one side (65 μL) to generate a chemoattractant gradient, and the other side was filled with PB (65 μL).

2.6. Live-Cell Imaging of Migrating Cells

Cell migration was recorded using a Zeiss LSM 780 or 880 confocal microscope equipped with a Plan-Apochromat 63x/1.4 Oil DIC objective, image size 512 \times 512 pixels, and a frame interval of 1.26 s. For GFP: ex 488 nm/em filter BP 495–550 nm; for mRFP: ex 561 nm/em filter LP 570 nm.

Cell migration in PDMS microchannels and PDMS pillar arrays was recorded with an inverted Leica DMI8 LED fluorescence microscope using an 40 \times objective, image size 2048 \times 2048 pixels, and a frame interval of 10 s. For GFP: ex 475 nm/em 519 nm; for RFP: ex 560 nm/em 594 nm (DFT51011 for both channels).

2.7. Statistics

Results of the migration experiments were statistically analyzed using Graph Prism v9 with Students' *t* tests (Welch's *t*-test) for Figures 1d, 2d, 3d, 4c,e and S3a, or One-way ANOVA (Brown-Forsythe and Welch ANOVA tests) for Figures 1c,f, 2c, 3c, 4b, S1d and S4. Data shown represent mean values plus or minus SDs. * $p < 0.05$; ** $p < 0.01$; *** $p < 0.001$.

2.8. Determination of Centrosome and Nucleus Distance

Centrosome and nucleus centroids were tracked using an Imaris automatic tool. The track values of each center object (centrosome or nucleus) were subtracted and the difference between the tracks were calculated as the distance of centrosome and nucleus centers (Figure S1f–h). The displayed frames of the trajectory give the values of the nucleus position in relation to the centrosome during oriented migration (Figure S1h).

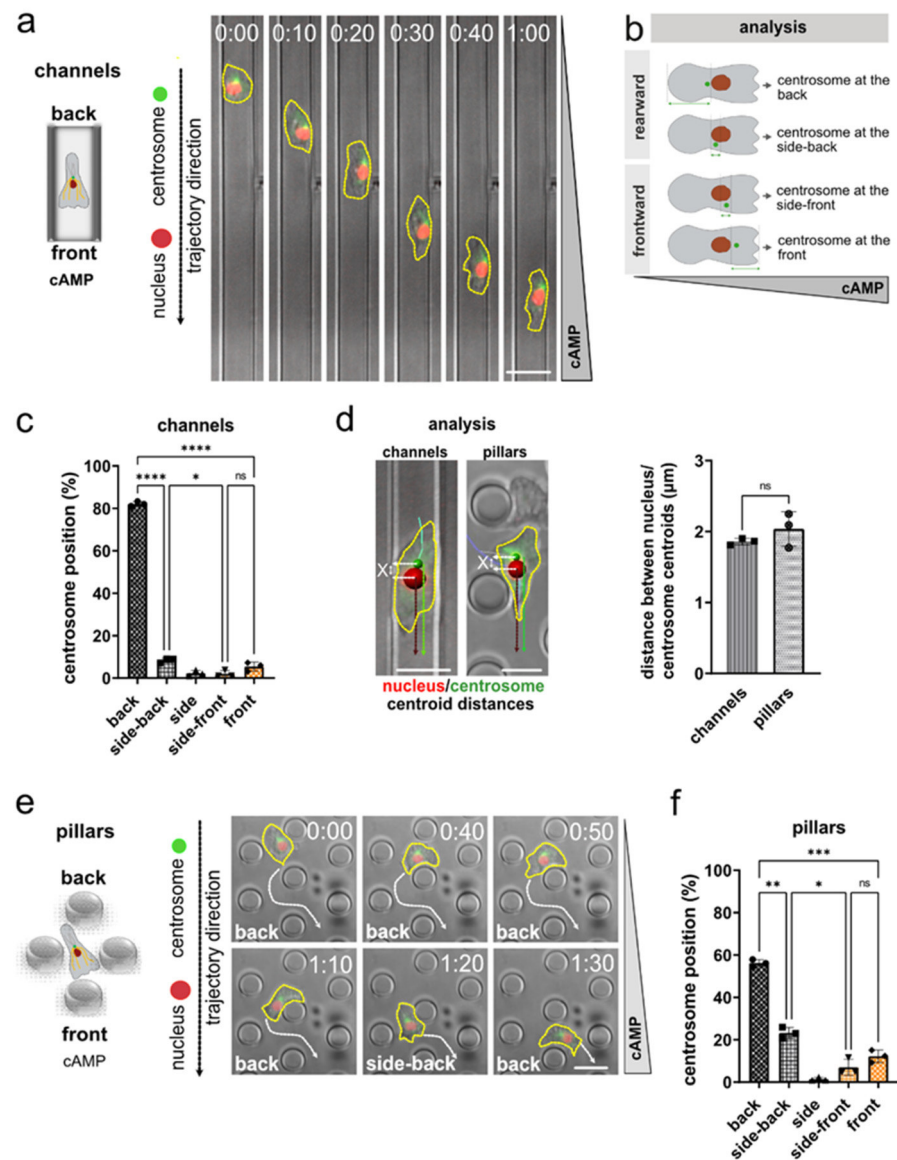


Figure 1. The centrosome of *Dictyostelium* cells migrating in microchannels or micropillar arrays along a cAMP gradient is preferentially located behind the nucleus. (a) Scheme (left) and representative microscopy images (right) of an aggregation competent *Dictyostelium* cell migrating in a microchannel along a gradient of cAMP. The cells express both the nuclear marker mRFP-histone (red), and GFP-tubulin (green) to highlight centrosomes and microtubules. Time is indicated in min and s at the top. The cell shape is highlighted by a yellow dashed line. (b) Principle of quantification. (c) Centrosome position during migration in microchannels within a gradient of cAMP. $N = 3$, number of cells = 32. (d) Representative images of *Dictyostelium* cells showing analysis of nucleus (red) and centrosome (green) centroid distances (indicated by “X”) (left). Histogram (right) displays the quantification of the distances between the nucleus and centrosome centroids during migration in microchannels and micropillar arrays along a cAMP gradient. $N = 3$, number of cells = 30. (e) Scheme (left), and representative microscopy images (right) of a cell migrating in a field of micropillars along a gradient of cAMP gradient, recorded with a time interval of 10 s per frame. The white arrows indicate the trajectory of the cell. The numbers indicate the time in min and s. (f) Quantification of the centrosome position during migration in an micropillar array along a gradient of cAMP. $N = 3$, number of cells = 30. Scale bars are 10 μm . * $p < 0.05$, ** $p < 0.01$, *** $p < 0.001$, **** $p < 0.0001$ are significant, and ns = not significant.

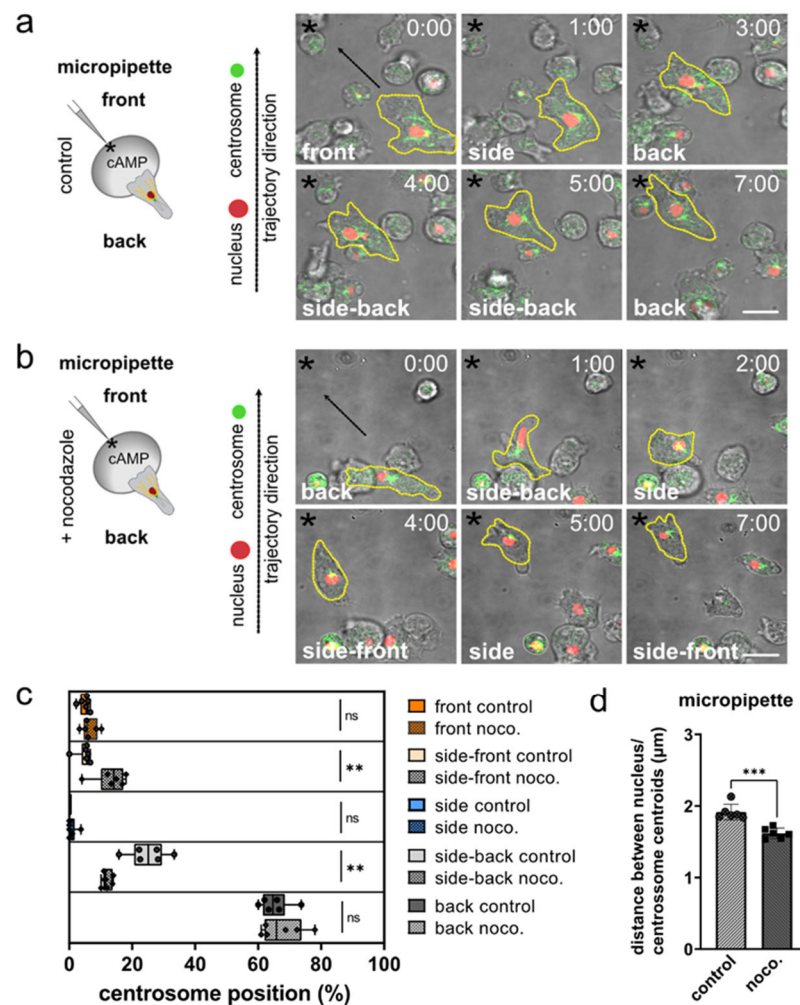


Figure 2. In aggregation-competent *Dictyostelium* cells moving in a gradient of cAMP released from a micropipette, the centrosome is positioned behind the nucleus, but frequently relocates when microtubules are disrupted. **(a,b)** Schemes (left) and representative microscopy images (right) of *Dictyostelium* cells migrating toward a micropipette tip releasing cAMP (indicated by asterisks). The cells express both the nuclear marker mRFP-histone (red), and GFP-tubulin (green) to highlight centrosomes and microtubules. Time is indicated in min and s at the top. The cell shape is highlighted by a yellow dashed line. Images were taken with 10 s-frame intervals. $N = 6$, number of cells = 50 for control; $N = 6$, number of cells = 52 for nocodazole. **(a)** Shows control cells, **(b)** nocodazole-treated cells. **(c)** Analysis of centrosome positions in control and nocodazole-treated (noco.) cells. Note that there were no events for the side control. **(d)** Nocodazole treatment decreases the distance between the center position (centroid) of the nucleus and the center of the centrosome. Scale bars are 10 μm . * $p < 0.05$, ** $p < 0.01$, *** $p < 0.001$ are significant, and ns = not significant.

2.9. Analysis of the Centrosome Position Nucleus/Centrosome Centroids Relative to Cell Center

Manual analysis: Manual analysis of the orientation of the centrosome-to-nucleus axis in linear microchannels (Figure S1a–c) was performed using ImageJ (<https://imagej.net/>) [59]. Seven horizontal lines with equal spacing were added to each image sequence (Figure S1a). Cells that did not cross at least three lines while migrating, were excluded from analysis. Additionally, only single cells migrating directionally along the chemoattractant gradient were analyzed. The nucleus and centrosome length were determined using a line tool from Image J, and the nucleus and centrosome centroids were determined as length/2. The centrosome and nucleus positions, as well as their centroids relative to the cell center, were evaluated for each frame when the nucleus of a cell reached one of the horizontal crossing lines (Figures S1b and S2). To calculate the nucleus and centroid distances to the

cell center, seven crossing lines were drawn in each image and used as reference for the calculation of cell length, the cell centroid, and the distances from the nucleus/centrosome centroid to the cell center (Figure S2a–d). The nucleus/centrosome centroid distances to the cell rear, where divided by the distance of the cell center to the back of the cell; thus, the values closer to 1.0, mean closer to the center of the cell. The evaluation of centroid centrosome/nucleus distance to the cell center of a single cell per frame was calculated for the folate experiments, as displayed in Figure S2e,f.

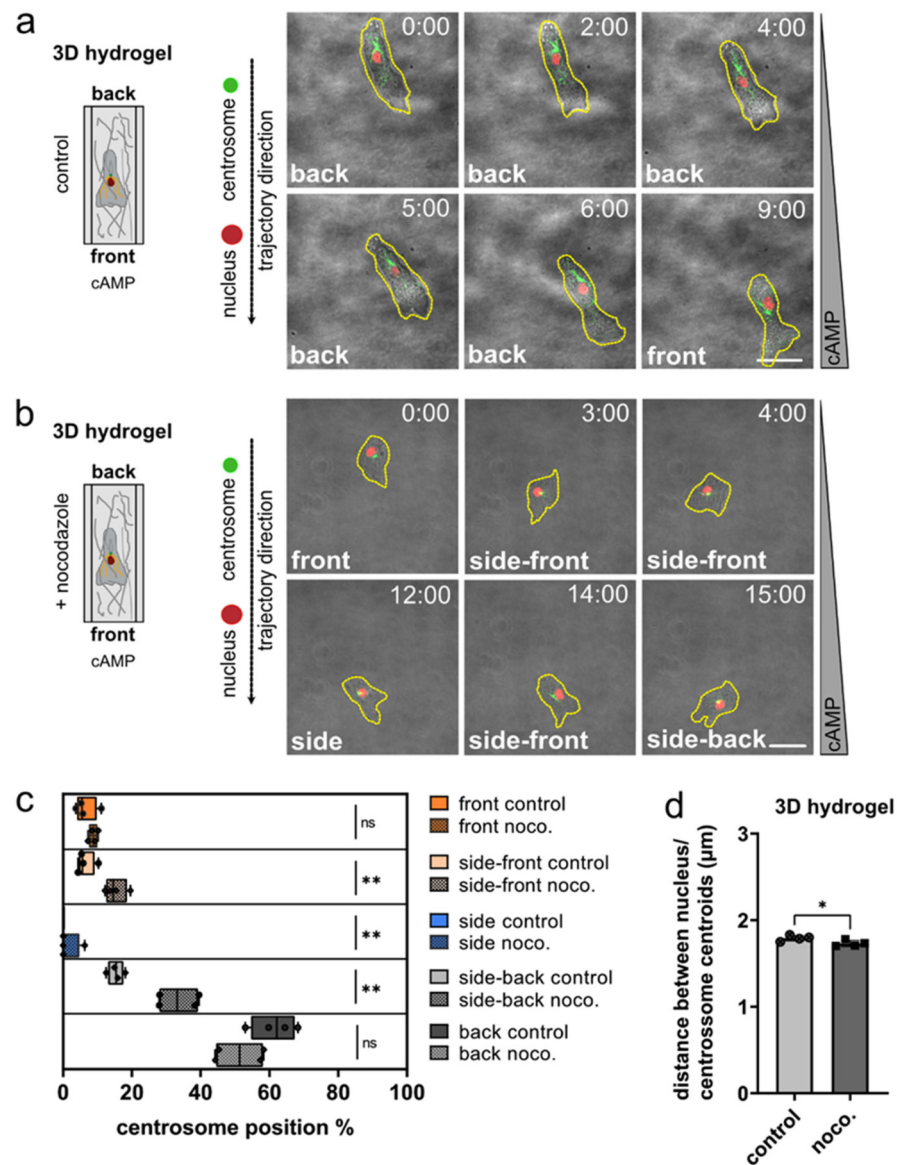


Figure 3. Centrosome positioning in aggregation competent *Dictyostelium* cells moving chemotactically in 3D environments. (a,b) Schemes (left), and representative microscopy images (right) of a *Dictyostelium* cell migrating in a chemotaxis chamber with a 3D hydrogel matrix. The cells express both the nuclear marker mRFP-histone (red), and GFP-tubulin (green) to highlight centrosomes and microtubules. The cell shape is marked by a yellow dashed line. Images were taken with 10 s-frame intervals. Time is indicated in min and s at the top. $N = 4$, number of cells = 40 for control; $N = 4$, number of cells = 40 for nocodazole. (c) Analysis of the position of the centrosome in *Dictyostelium* cells moving chemotactically in 3D hydrogels. Note that there were no events for side control. (d) After nocodazole treatment, in cells moving chemotactically in 3D the distance between the centroid of the nucleus and the centroid of the centrosome was slightly decreased. Scale bars are 10 μm . * $p < 0.05$, ** $p < 0.01$ are considered significant, and ns = not significant.

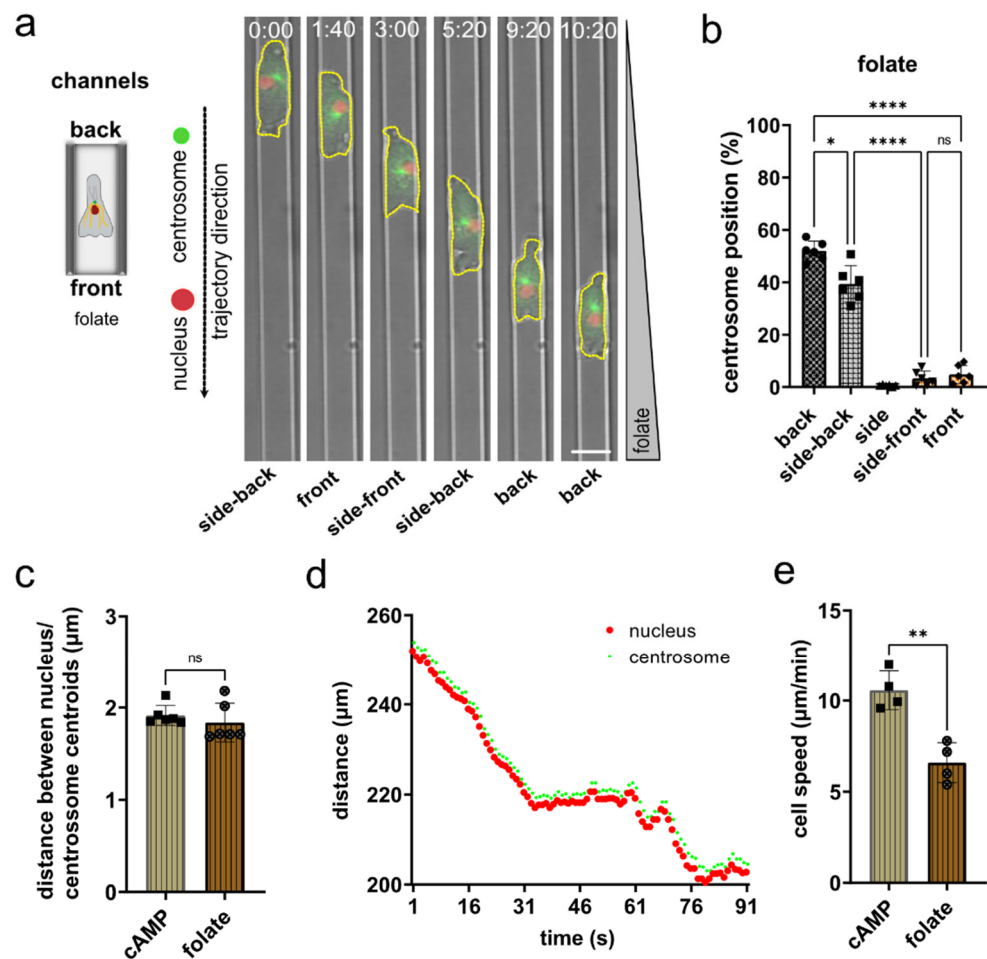


Figure 4. In growth phase *Dictyostelium* cells migrating in microchannels along a gradient of folate, the centrosome is preferentially located behind the nucleus. (a) Scheme (left) and representative microscopy images (right) of a *Dictyostelium* cell migrating in a microchannel along a folate gradient. The cell shape is highlighted by a yellow dashed line. Images were taken with 10 s-frame intervals. Time is indicated in min and s at the top. (b) Quantification of the centrosome position during migration in microchannels along a gradient of folate. $N = 6$, number of cells = 40. (c) Quantification of the distance between nucleus and centrosome of *Dictyostelium* cells migrating in microchannels in a folate gradient ($n = 6$, cells = 40). (d) Displacement of tracks for nucleus (red) and centrosome (green) recorded for one cell over time. (e) Migration speed in microchannels determined for growth phase *Dictyostelium* cells moving along a gradient of folate and for aggregation competent cells moving in a gradient of cAMP. * $p < 0.05$, ** $p < 0.01$, **** $p < 0.0001$ are significant, and ns = not significant.

For cAMP or folate chemotaxis experiments in linear microchannels (Figures S1a,b and S2b,c), the positions of the nucleus and centrosome along the cell axis were manually determined by measuring their distance from the cell rear in relation to the cell length, to calculate their relative intracellular position along the cell axis (Figure S1d). From this dataset, we further calculated the centrosome-to-nucleus distance (Figure S1e) and the nucleus/centrosome centroid relative distance to the cell center (Figure S2).

Automatic analysis: Centrosome and nucleus centroids were tracked using the Imaris automatic tool “Spots creation tool’s automatic generation feature”. After completion of automatic generation, further optimization of tracks was completed manually. The trajectory was determined between a reference point, where the chemoattractant was released, and the centroid of the objects (nucleus and centrosome). The distance from the centrosome centroid minus the distance of the nucleus centroid to a reference chemoattractant point was calculated and used to determine the centrosome position (Figure S1f,g). A spot of 2.0 μm

was set for the nucleus and a spot of 1.0 μm for the centrosome, with centroids determined automatically. The distance of the nucleus centroid to the nucleus border was set to 1.0 μm , and the centrosome centroid distance to the centroid border was 0.5 μm . Thus, all centrosomes with a difference of centrosome centroid distance minus the nucleus centroid larger than +1.5 μm were characterized as having a centrosome position at the ‘back’ of the nucleus. Values smaller than +1.5 μm were characterized as “side-back” position. Positions of the centrosome within differences smaller than $-1.5 \mu\text{m}$ were characterized as “side-front”, and larger than $-1.5 \mu\text{m}$ as “front” (Figure S1g,h).

3. Results

3.1. Nucleus and Centrosome Positioning in *Dictyostelium* Cells Migrating in Confined Environments

To study centrosome and nucleus positioning in migrating *Dictyostelium discoideum*, we employed cells in the early developmental stage, stably encoding both the nuclear marker mRFP-histone and GFP-tubulin as a marker for the microtubules and centrosomes, and performed live-cell imaging in linear microchannels with a gradient of cAMP as chemoattractant. In this confined environment, *Dictyostelium* cells migrate highly directionally and persistently along straight paths (Figure 1a; Video S1). This setup allows the precise quantification of the orientation of the centrosome–nucleus axis with an accurate centrosome positioning classification (Figures 1b and S1), as well as the determination of the nucleus and centrosome centroids relative to the cell center (Figure S2). Automated tracking (Figure S1g,h) and quantification, which we controlled by manual analysis (Figure S1b–d), revealed a preferential positioning of the centrosome behind the nucleus (Figure 1c). While we also observed positioning of the centrosome to the sideward and front of the nucleus (Figure 1c), and dynamic re-positioning of the centrosome closer to the cell center in individual cells (Figures S1e and S2; Video S1), we found a strong preference of the centrosome to be positioned in very close proximity, behind the nucleus (Figure 1c,d).

We next imaged mRFP-histone and GFP-tubulin expressing *Dictyostelium* cells migrating along a cAMP gradient in between arrays of micropillars, as this environment requires *Dictyostelium* to deviate from entirely straight paths, by performing turns around individual micropillars. Notably, we observed that during reorientation of the centrosome–nucleus, the position of the nucleus within the cells stays relatively unchanged, while the centrosome dynamically repositions between a forward and rearward localization in relation to the nucleus (Figure 1e; Video S2). Again, we noted a close proximity of the centrosome and the nucleus, and a strong preference of the centrosome to be positioned at the back and side-back of the nucleus (Figure 1f).

To corroborate these results, we investigated the orientation of the centrosome–nucleus axis while *Dictyostelium* migrates within a gradient of cAMP released from a micropipette (Figure 2a,b). The repositioning of the micropipette filled with cAMP, causes a local change within the gradient, which is sensed by the cells and causes reorientation towards the pipette tip within seconds [60]. While *Dictyostelium* cells migrated in this experiment on a two-dimensional surface, their path was not dictated by the microenvironment and, thus, allowed non-straight migration, such as between micropillars (Video S3). Moreover, in this experimental setting, we observed a non-random orientation of the centrosome–nucleus axis, with the centrosome located behind the nucleus (Figure 2c).

3.2. The Role of Microtubules for Centrosome Positioning in *Dictyostelium* Cells Migrating in 2D Confined Environments

To investigate the role of the microtubule cytoskeleton in centrosome positioning, we tested the orientation of the centrosome–nucleus axis after application of the microtubule-depolymerizing drug nocodazole. Nocodazole interferes with the polymerization of microtubules, and though it is known to be less efficient in *Dictyostelium* than in other eukaryotes, it causes massive shortening of microtubules, visible as short stumps radiating from the centrosome [61]. Live-cell imaging of migration to a cAMP-containing micropipette still revealed a preferential positioning of the centrosome behind the nucleus in the presence

of nocodazole, yet with a more frequently inverted orientation, in which the centrosome is positioned frontward of the nucleus (Figure 2c). In the presence of nocodazole, *Dictyostelium* cells migrate with reduced velocity (Figure S3a) and show a higher mobility of the centrosome when the microtubule cytoskeleton is non-functional, leading to a reduction of the distance between nucleus-centrosome centroids (Figure 2d). Nocodazole treatment abolishes the contact of long microtubules that typically span through the cell body toward cortical areas, whereas short microtubules in the direct vicinity of the centrosome remain present (Figure S3b; Video S4). Thus, this suggests that the remaining short microtubules mechanically connect the centrosome with the nucleus.

These findings show that a functional microtubule cytoskeleton contributes to the correct orientation of the centrosome–nucleus axis in motile *Dictyostelium*.

3.3. Nucleus and Centrosome Positioning in *Dictyostelium* Cells Migrating in 3D Confined Environments

We then tested whether the observed configuration of the centrosome-to-nucleus axis can be characterized as well in three-dimensional matrices, which represent a close proxy of natural environments. To this end, we imaged chemotactic migration of *Dictyostelium* in hydrogel, as well as collagen matrices (Figure 3; Figure S4). As in 2D migration, *Dictyostelium* cells moving in 3D showed a strong preference to position the centrosome behind the nucleus (Figure 3a; Video S5). This location was altered upon depolymerization of microtubules (Figure 3b; Video S6), which resulted in the centrosome being found much more frequently on the side or front-ward of the nucleus (Figure 3c). It should also be noted that, in nocodazole-treated cells, the distance between the centrosome and the nucleus was slightly reduced (Figure 3d).

In summary, we found that the centrosome and the nucleus are non-randomly positioned in motile *Dictyostelium* cells. This non-random configuration positions the nucleus in front of the centrosome, with respect to the direction of migration. This orientation is clearly preferred in motile *Dictyostelium* cells at the developmental stage, occurring on flat two-dimensional substrates, in confining microchannels, in between micropillars, as well as in three-dimensional matrices.

3.4. Nucleus and Centrosome Positioning in *Dictyostelium* Cells Migrating in Confined Environments toward Folate

To test whether the orientation of the “centrosome-nucleus in front” axis is the generally preferred position at the different developmental stages of *Dictyostelium*, we imaged cells at the growth phase migrating chemotactically along a folate gradient in linear microchannels (Figure 4a; Video S7). Subsequent analysis revealed a strong preference to position the centrosome behind or side-back of the nucleus (Figure 4b). The determination of the distance between the centroids of the nucleus and the centrosome revealed no fundamental differences between cells migrating in folate or cAMP gradients (Figure 4c). The plot of an exemplary track shows how the centrosome follows the nucleus (Figure 4d). In 2D microchannels, growth phase *Dictyostelium* cells migrate more slowly toward folate than cells of the early aggregation state toward cAMP as chemoattractant (Figure 4e). A similar difference has been shown previously for other conditions.

Altogether, our data show that *Dictyostelium* cells position their centrosome and the nucleus in a non-random orientation during motility at different developmental stages, with the preferred position of the centrosome always at the back of the nucleus. This positioning is reinforced by microtubules that emanate from the centrosome and extend to the front cortex. Changes in the direction of a cell caused by a change in the chemoattractant gradient results in a transient displacement of the centrosome from the pseudopod-nucleus-centrosome axis.

4. Discussion

The positioning of organelles inside cells is non-random, and this non-random positioning is functionally important [62]. The nucleus — the largest and stiffest cell or-

ganelle [63] — and the centrosome — the major microtubule organizing center [25] — are typically positioned in close proximity in a particular orientation [33]. Many motile cells, such as fibroblasts and neurons, preferentially position their centrosome frontward of the nucleus [34], e.g., during polarized fibroblast migration into cell-free wound areas [64]. This particular alignment of the centrosome-to-nucleus axis is established by linking the nucleus with the cytoskeleton [65], and supports local release of proteases for extracellular matrix proteolysis at constricting pores [66], and the pulling of the nucleus through narrow pores [67].

Whereas the cellular microenvironment (e.g., degree of confinement) also appears to influence the orientation of the centrosome-to-nucleus axis [33,68], the general concept emerges that slowly migrating mesenchymal-like cells preferentially position their centrosome in front of the nucleus. In contrast, recent findings have shown that fast amoeboid-like migrating immune cells, such as dendritic cells, preferentially position their centrosome to the rear of the nucleus [38,39]. This unexpected positioning of the nucleus frontward to the centrosome [32,39], and closely behind the cellular leading edge [39,69], supports these fast migrating cells in using their nucleus as a mechanical gauge to probe for suitable larger pores in the microenvironment along their paths of migration [39].

Here, we investigated the positioning of the centrosome-to-nucleus axis in motile *Dictyostelium discoideum* cells. *Dictyostelium* represents a long-standing cellular model to discover general concepts in cell motility [19,20,70–73]. Surprisingly, the positioning of the centrosome in relation to the nucleus in this traditional model for amoeboid migration was initially analyzed only by evaluating electron micrographs [50]. The authors came to the conclusion that the centrosome shows no preferential position anterior or posterior to the nucleus; rather, its position correlates with the type of migration and perhaps with the nature of cell–cell adhesion [50].

Another early study previously showed that the centrosome does not bias the cell, as it was observed that after formation of a new pseudopod, the centrosome reorients within an average of 12 s [51]. Thus, they concluded that the centrosome does not determine the alignment of the movement [51]. However, it has been consistently discussed that the centrosome may also be located anterior to the nucleus relative to the direction of movement, depending on the developmental stage or the conditions of migration. In summary, a systematic analysis that investigated the position of the centrosome during migration was lacking.

To close this knowledge gap, we investigated two major motile states of *Dictyostelium*: single-cell migration in the growth phase along a folate gradient, and single-cell migration in the developmental stage along a cAMP gradient. We found that the centrosome is positioned in both states close to the cell center, and that the nucleus is positioned frontward of the centrosome. Furthermore, by extensively investigating *Dictyostelium* migration in diverse microenvironments, ranging from two-dimensional substrates and confining microchannels to three-dimensional extracellular matrices, we discovered that this specific orientation of the centrosome-to-nucleus axis is a general feature of migrating *Dictyostelium* cells. Thus, amoeboid migrating *Dictyostelium* cells position the nucleus frontward of the centrosome, similarly to amoeboid migrating immune cells, suggesting evolutionary conservation of centrosome-to-nucleus positioning in motile amoeboid cells.

The extension of a pseudopod in a new direction causes the reorientation of the centrosome. A crucial question that remains to be solved is how these processes are coupled. The present study was not designed to answer this general question. However, our findings are in agreement with the assumption that reorientation of the centrosome and microtubules extending toward the front reinforce the direction of movement. Thus, the active balancing of the pseudopod-nucleus-centrosome axis is a critical component. Our results with nocodazole-treated cells strongly support this notion.

Our findings suggest a general concept, in which fast moving amoeboid-like cells position their nucleus in front of the centrosome, whereas slow mesenchymal-like cells position their nucleus behind the centrosome. In future, it will be interesting to further

elucidate what other functional significance this configuration and positioning of the centrosome–nucleus axis has for amoeboid migration. Moreover, our findings highlight the relevance of the genetically accessible amoeba *Dictyostelium* as a cellular model to discover mechanisms of cell migration. This approach will also help to transfer well established techniques in *Dictyostelium* to the leukocyte model system, and thus may yield new insights into principles of directional cell migration and polarity, as important elements in host defense, wound healing, and development.

Supplementary Materials: The following supporting information can be downloaded at: <https://www.mdpi.com/article/10.3390/cells11111776/s1>, Figure S1. Microchannel setup and manual/automatic analysis of centrosome positioning. Figure S2. Position of nucleus and centrosome centroids in relation to the cell center. Figure S3. Nocodazole treatment results in decrease of cell speed and shorter microtubules in *Dictyostelium* cells. Figure S4. Positioning of the centrosome relative to the nucleus in aggregation competent *Dictyostelium* cells migrating chemotactically in 3D hydrogel or collagen type I matrices. Video S1. The centrosome of *Dictyostelium* cells migrating in microchannels along a cAMP gradient preferentially locates rearward of the nucleus. Video S2. The centrosome of *Dictyostelium* cells migrating in a micropillar array along a cAMP gradient preferentially locates rearward of the nucleus. Video S3. The preferential position of the centrosome of *Dictyostelium* cells during migration toward cAMP released from a micropipette is rearward of the nucleus. Video S4. In *Dictyostelium* cells with disrupted microtubules, the position of the centrosome changes frequently from the back to sides and front of the nucleus during migration in a gradient of cAMP released from a micropipette. Video S5. The centrosome of *Dictyostelium* cells is predominantly located behind the nucleus during migration in 3D environments. Video S6. In *Dictyostelium* cells moving in 3D environments, the position of the centrosome is more variable relative to the nucleus when microtubules are disrupted. Video S7. The centrosome of *Dictyostelium* cells migrating in microchannels along a folate gradient preferentially locates rearward of the nucleus.

Author Contributions: Conceptualization, H.I.-A., J.R. and A.M.-T.; methodology, H.I.-A., J.K., J.R. and A.M.-T.; validation, H.I.-A., J.K., D.v.d.H., J.R. and A.M.-T.; formal analysis, H.I.-A., J.K. and D.v.d.H.; resources, H.I.-A., J.R. and A.M.-T.; writing, review, and editing, H.I.-A., J.K., J.R. and A.M.-T.; supervision, A.M.-T.; funding acquisition, H.I.-A., J.R. and A.M.-T. All authors have read and agreed to the published version of the manuscript.

Funding: We gratefully acknowledge financial support from the DFG (Collaborative Research Center SFB914, projects A07E to A.M.-T., A12 to J.R., and Z01 to H. I.-A.), the Peter Hans Hofschneider Professorship of the Stiftung Experimentelle Biomedizin (to J.R.), and froy LMU-Excellent within the framework of the German Excellence Initiative (to J.R.).

Institutional Review Board Statement: Not applicable.

Informed Consent Statement: Not applicable.

Data Availability Statement: If not contained within the article or Supplementary Material of this publication, data are available from the corresponding author.

Acknowledgments: We thank the Core Facility Bioimaging of the Biomedical Center (BMC) and the Core Facility Bioimaging of the Walter Brendel Center for experimental Medicine of the Ludwig Maximilian University Munich for excellent support, and Daniela Rieger (Cell Biology, BMC) for technical help.

Conflicts of Interest: The authors declare no conflict of interest.

References

1. Friedl, P.; Wolf, K. Plasticity of cell migration: A multiscale tuning model. *J. Cell Biol.* **2010**, *188*, 11–19. [[CrossRef](#)] [[PubMed](#)]
2. Ridley, A.J.; Schwartz, M.A.; Burridge, K.; Firtel, R.A.; Ginsberg, M.H.; Borisy, G.; Parsons, J.T.; Horwitz, A.R. Cell migration: Integrating signals from front to back. *Science* **2003**, *302*, 1704–1709. [[CrossRef](#)] [[PubMed](#)]
3. SenGupta, S.; Parent, C.A.; Bear, J.E. The principles of directed cell migration. *Nat. Rev. Mol. Cell Biol.* **2021**, *22*, 529–547. [[CrossRef](#)] [[PubMed](#)]
4. Artemenko, Y.; Lampert, T.J.; Devreotes, P.N. Moving towards a paradigm: Common mechanisms of chemotactic signaling in *Dictyostelium* and mammalian leukocytes. *Cell Mol. Life Sci.* **2014**, *71*, 3711–3747. [[CrossRef](#)]

5. Yamada, K.M.; Sixt, M. Mechanisms of 3D cell migration. *Nat. Rev. Mol. Cell Biol.* **2019**, *20*, 738–752. [[CrossRef](#)]
6. Kameritsch, P.; Renkawitz, J. Principles of Leukocyte Migration Strategies. *Trends Cell Biol.* **2020**, *30*, 818–832. [[CrossRef](#)]
7. Lämmermann, T.; Bader, B.L.; Monkley, S.J.; Worbs, T.; Wedlich-Söldner, R.; Hirsch, K.; Keller, M.; Förster, R.; Critchley, D.R.; Fässler, R.; et al. Rapid leukocyte migration by integrin-independent flowing and squeezing. *Nature* **2008**, *453*, 51–55. [[CrossRef](#)]
8. Zatulovskiy, E.; Tyson, R.; Bretschneider, T.; Kay, R.R. Bleb-driven chemotaxis of Dictyostelium cells. *J. Cell Biol.* **2014**, *204*, 1027–1044. [[CrossRef](#)]
9. Yoshida, K.; Soldati, T. Dissection of amoeboid movement into two mechanically distinct modes. *J. Cell Sci.* **2006**, *119*, 3833–3844. [[CrossRef](#)]
10. Renkawitz, J.; Schumann, K.; Weber, M.; Lämmermann, T.; Pflücke, H.; Piel, M.; Polleux, J.; Spatz, J.P.; Sixt, M. Adaptive force transmission in amoeboid cell migration. *Nat. Cell Biol.* **2009**, *11*, 1438–1443. [[CrossRef](#)]
11. Tyson, R.A.; Zatulovskiy, E.; Kay, R.R.; Bretschneider, T. How blebs and pseudopods cooperate during chemotaxis. *Proc. Natl. Acad. Sci. USA* **2014**, *111*, 11703–11708. [[CrossRef](#)] [[PubMed](#)]
12. Srivastava, N.; Traynor, D.; Piel, M.; Kabla, A.J.; Kay, R.R. Pressure sensing through Piezo channels controls whether cells migrate with blebs or pseudopods. *Proc. Natl. Acad. Sci. USA* **2020**, *117*, 2506–2512. [[CrossRef](#)] [[PubMed](#)]
13. Müller-Taubenberger, A.; Kortholt, A.; Eichinger, L. Simple system-substantial share: The use of Dictyostelium in cell biology and molecular medicine. *Eur. J. Cell Biol.* **2013**, *92*, 45–53. [[CrossRef](#)]
14. Storey, C.L.; Williams, R.S.B.; Fisher, P.R.; Annesley, S.J. Dictyostelium discoideum: A Model System for Neurological Disorders. *Cells* **2022**, *11*, 463. [[CrossRef](#)] [[PubMed](#)]
15. Jin, T.; Xu, X.; Fang, J.; Isik, N.; Yan, J.; Brzostowski, J.A.; Hereld, D. How human leukocytes track down and destroy pathogens: Lessons learned from the model organism Dictyostelium discoideum. *Immunol. Res.* **2009**, *43*, 118–127. [[CrossRef](#)] [[PubMed](#)]
16. Devreotes, P.N.; Zigmond, S.H. Chemotaxis in eukaryotic cells: A focus on leukocytes and Dictyostelium. *Annu. Rev. Cell Biol.* **1988**, *4*, 649–686. [[CrossRef](#)]
17. Swaney, K.F.; Huang, C.H.; Devreotes, P.N. Eukaryotic chemotaxis: A network of signaling pathways controls motility, directional sensing, and polarity. *Annu. Rev. Biophys.* **2010**, *39*, 265–289. [[CrossRef](#)]
18. Cai, H.; Devreotes, P.N. Moving in the right direction: How eukaryotic cells migrate along chemical gradients. *Semin Cell Dev Biol* **2011**, *22*, 834–841. [[CrossRef](#)]
19. Van Haastert, P.J.; Devreotes, P.N. Chemotaxis: Signalling the way forward. *Nat. Rev. Mol. Cell Biol.* **2004**, *5*, 626–634. [[CrossRef](#)]
20. Insall, R.H. Understanding eukaryotic chemotaxis: A pseudopod-centred view. *Nat. Rev. Mol. Cell Biol.* **2010**, *11*, 453–458. [[CrossRef](#)]
21. Pan, P.; Hall, E.M.; Bonner, J.T. Folic acid as second chemotactic substance in the cellular slime moulds. *Nat. New Biol.* **1972**, *237*, 181–182. [[CrossRef](#)] [[PubMed](#)]
22. Konijn, T.M.; Van De Meene, J.G.; Bonner, J.T.; Barkley, D.S. The acrasin activity of adenosine-3',5'-cyclic phosphate. *Proc. Natl. Acad. Sci. USA* **1967**, *58*, 1152–1154. [[CrossRef](#)] [[PubMed](#)]
23. Klein, P.S.; Sun, T.J.; Saxe, C.L., 3rd; Kimmel, A.R.; Johnson, R.L.; Devreotes, P.N. A chemoattractant receptor controls development in Dictyostelium discoideum. *Science* **1988**, *241*, 1467–1472. [[CrossRef](#)] [[PubMed](#)]
24. Pan, M.; Xu, X.; Chen, Y.; Jin, T. Identification of a Chemoattractant G-Protein-Coupled Receptor for Folic Acid that Controls Both Chemotaxis and Phagocytosis. *Dev. Cell* **2016**, *36*, 428–439. [[CrossRef](#)]
25. Akhmanova, A.; Kapitein, L.C. Mechanisms of microtubule organization in differentiated animal cells. *Nat. Rev. Mol. Cell Biol.* **2022**, 1–18. [[CrossRef](#)]
26. Kaverina, I.; Straube, A. Regulation of cell migration by dynamic microtubules. *Semin. Cell Dev. Biol.* **2011**, *22*, 968–974. [[CrossRef](#)]
27. Yoo, S.K.; Lam, P.Y.; Eichelberg, M.R.; Zasadil, L.; Bement, W.M.; Huttenlocher, A. The role of microtubules in neutrophil polarity and migration in live zebrafish. *J. Cell Sci.* **2012**, *125*, 5702–5710. [[CrossRef](#)]
28. Etienne-Manneville, S. Actin and microtubules in cell motility: Which one is in control? *Traffic* **2004**, *5*, 470–477. [[CrossRef](#)]
29. Xu, J.; Wang, F.; Van Keymeulen, A.; Rentel, M.; Bourne, H.R. Neutrophil microtubules suppress polarity and enhance directional migration. *Proc. Natl. Acad. Sci. USA* **2005**, *102*, 6884–6889. [[CrossRef](#)]
30. Euteneuer, U.; Schliwa, M. Persistent, directional motility of cells and cytoplasmic fragments in the absence of microtubules. *Nature* **1984**, *310*, 58–61. [[CrossRef](#)]
31. Ganguly, A.; Yang, H.; Sharma, R.; Patel, K.D.; Cabral, F. The role of microtubules and their dynamics in cell migration. *J. Biol. Chem.* **2012**, *287*, 43359–43369. [[CrossRef](#)] [[PubMed](#)]
32. Kopf, A.; Kiermaier, E. Dynamic Microtubule Arrays in Leukocytes and Their Role in Cell Migration and Immune Synapse Formation. *Front. Cell Dev. Biol.* **2021**, *9*, 635511. [[CrossRef](#)] [[PubMed](#)]
33. Luxton, G.W.; Gundersen, G.G. Orientation and function of the nuclear-centrosomal axis during cell migration. *Curr. Opin. Cell Biol.* **2011**, *23*, 579–588. [[CrossRef](#)] [[PubMed](#)]
34. Gundersen, G.G.; Worman, H.J. Nuclear positioning. *Cell* **2013**, *152*, 1376–1389. [[CrossRef](#)] [[PubMed](#)]
35. Barros-Becker, F.; Lam, P.Y.; Fisher, R.; Huttenlocher, A. Live imaging reveals distinct modes of neutrophil and macrophage migration within interstitial tissues. *J. Cell Sci.* **2017**, *130*, 3801–3808. [[CrossRef](#)] [[PubMed](#)]
36. Gudima, G.O.; Vorobjev, I.A.; Chentsov Yu, S. Centriolar location during blood cell spreading and motion in vitro: An ultrastructural analysis. *J. Cell Sci.* **1988**, *89*, 225–241. [[CrossRef](#)]

37. Gudima, G.O.; Vorob'ev, I.A.; Chentsov Iu, S. Cell center of macrophages, granulocytes and lymphocytes during in vitro cell spreading, polarization and movement. *Tsitologiya* **1984**, *26*, 1002–1007.
38. Kopf, A.; Renkawitz, J.; Hauschild, R.; Girkontaite, I.; Tedford, K.; Merrin, J.; Thorn-Seshold, O.; Trauner, D.; Hacker, H.; Fischer, K.D.; et al. Microtubules control cellular shape and coherence in amoeboid migrating cells. *J. Cell Biol.* **2020**, *219*. [[CrossRef](#)]
39. Renkawitz, J.; Kopf, A.; Stopp, J.; de Vries, I.; Driscoll, M.K.; Merrin, J.; Hauschild, R.; Welf, E.S.; Danuser, G.; Fiolka, R.; et al. Nuclear positioning facilitates amoeboid migration along the path of least resistance. *Nature* **2019**, *568*, 546–550. [[CrossRef](#)]
40. Uzbekov, R.E.; Vorob'ev, I.A.; Drachev, V.A. The effect of the laser microirradiation of the cell center on neutrophil motility. *Tsitologiya* **1989**, *31*, 874–881.
41. Eddy, R.J.; Pierini, L.M.; Maxfield, F.R. Microtubule asymmetry during neutrophil polarization and migration. *Mol. Biol. Cell* **2002**, *13*, 4470–4483. [[CrossRef](#)]
42. Gräf, R.; Batsios, P.; Meyer, I. Evolution of centrosomes and the nuclear lamina: Amoebozoan assets. *Eur. J. Cell Biol.* **2015**, *94*, 249–256. [[CrossRef](#)] [[PubMed](#)]
43. Gräf, R.; Grafe, M.; Meyer, I.; Mitic, K.; Pitzten, V. The Dictyostelium Centrosome. *Cells* **2021**, *10*, 2657. [[CrossRef](#)] [[PubMed](#)]
44. Schulz, I.; Baumann, O.; Samereier, M.; Zoglmeier, C.; Gräf, R. Dictyostelium Sun1 is a dynamic membrane protein of both nuclear membranes and required for centrosomal association with clustered centromeres. *Eur. J. Cell Biol.* **2009**, *88*, 621–638. [[CrossRef](#)] [[PubMed](#)]
45. Xiong, H.; Rivero, F.; Euteneuer, U.; Mondal, S.; Mana-Capelli, S.; Larochelle, D.; Vogel, A.; Gassen, B.; Noegel, A.A. Dictyostelium Sun-1 connects the centrosome to chromatin and ensures genome stability. *Traffic* **2008**, *9*, 708–724. [[CrossRef](#)]
46. Mana-Capelli, S.; Gräf, R.; Larochelle, D.A. Dictyostelium discoideum CenB is a bona fide centrin essential for nuclear architecture and centrosome stability. *Eukaryot Cell* **2009**, *8*, 1106–1117. [[CrossRef](#)]
47. Kuhnert, O.; Baumann, O.; Meyer, I.; Gräf, R. Functional characterization of CP148, a novel key component for centrosome integrity in Dictyostelium. *Cell Mol. Life Sci.* **2012**, *69*, 1875–1888. [[CrossRef](#)]
48. Tikhonenko, I.; Magidson, V.; Gräf, R.; Khodjakov, A.; Koonce, M.P. A kinesin-mediated mechanism that couples centrosomes to nuclei. *Cell Mol. Life Sci.* **2013**, *70*, 1285–1296. [[CrossRef](#)]
49. Sameshima, M. The orientation of nucleus, nucleus-associated body and protruding nucleolus in aggregating Dictyostelium discoideum. *Exp. Cell Res.* **1985**, *156*, 341–350. [[CrossRef](#)]
50. Sameshima, M.; Imai, Y.; Hashimoto, Y. The position of the microtubule-organizing center relative to the nucleus is independent of the direction of cell migration in Dictyostelium discoideum. *Cell Motil. Cytoskeleton.* **1988**, *9*, 111–116. [[CrossRef](#)]
51. Ueda, M.; Gräf, R.; MacWilliams, H.K.; Schliwa, M.; Euteneuer, U. Centrosome positioning and directionality of cell movements. *Proc. Natl. Acad. Sci. USA* **1997**, *94*, 9674–9678. [[CrossRef](#)] [[PubMed](#)]
52. Neujahr, R.; Albrecht, R.; Köhler, J.; Matzner, M.; Schwartz, J.M.; Westphal, M.; Gerisch, G. Microtubule-mediated centrosome motility and the positioning of cleavage furrows in multinucleate myosin II-null cells. *J. Cell Sci.* **1998**, *111*, 1227–1240. [[CrossRef](#)] [[PubMed](#)]
53. Koonce, M.P.; Tikhonenko, I. Centrosome Positioning in Dictyostelium: Moving beyond Microtubule Tip Dynamics. *Cells* **2018**, *7*, 29. [[CrossRef](#)] [[PubMed](#)]
54. Odell, J.; Sikirzhyski, V.; Tikhonenko, I.; Cobani, S.; Khodjakov, A.; Koonce, M. Force balances between interphase centrosomes as revealed by laser ablation. *Mol Biol Cell* **2019**, *30*, 1705–1715. [[CrossRef](#)] [[PubMed](#)]
55. Bindl, J.; Molnar, E.S.; Ecke, M.; Prassler, J.; Müller-Taubenberger, A.; Gerisch, G. Unilateral Cleavage Furrows in Multinucleate Cells. *Cells* **2020**, *9*, 1493. [[CrossRef](#)] [[PubMed](#)]
56. Renkawitz, J.; Reversat, A.; Leithner, A.; Merrin, J.; Sixt, M. Micro-engineered “pillar forests” to study cell migration in complex but controlled 3D environments. *Methods Cell Biol.* **2018**, *147*, 79–91. [[CrossRef](#)] [[PubMed](#)]
57. Kroll, J.; Ruiz-Fernandez, M.J.A.; Braun, M.B.; Merrin, J.; Renkawitz, J. Quantifying the Probing and Selection of Microenvironmental Pores by Motile Immune Cells. *Curr. Protoc.* **2022**, *2*, e407. [[CrossRef](#)]
58. Roth, H.; Samereier, M.; Trommler, G.; Noegel, A.A.; Schleicher, M.; Müller-Taubenberger, A. Balanced cortical stiffness is important for efficient migration of Dictyostelium cells in confined environments. *Biochem. Biophys. Res. Commun.* **2015**, *467*, 730–735. [[CrossRef](#)]
59. Schneider, C.A.; Rasband, W.S.; Eliceiri, K.W. NIH Image to ImageJ: 25 years of image analysis. *Nat. Methods* **2012**, *9*, 671–675. [[CrossRef](#)]
60. Gerisch, G. Imaging actin cytoskeleton dynamics in Dictyostelium chemotaxis. *Methods Mol. Biol.* **2009**, *571*, 385–400. [[CrossRef](#)]
61. Gräf, R.; Euteneuer, U.; Ho, T.H.; Rehberg, M. Regulated expression of the centrosomal protein DdCP224 affects microtubule dynamics and reveals mechanisms for the control of supernumerary centrosome number. *Mol. Biol. Cell* **2003**, *14*, 4067–4074. [[CrossRef](#)] [[PubMed](#)]
62. Bornens, M. Organelle positioning and cell polarity. *Nat. Rev. Mol. Cell Biol.* **2008**, *9*, 874–886. [[CrossRef](#)] [[PubMed](#)]
63. McGregor, A.L.; Hsia, C.R.; Lammerding, J. Squish and squeeze—the nucleus as a physical barrier during migration in confined environments. *Curr. Opin. Cell Biol.* **2016**, *40*, 32–40. [[CrossRef](#)] [[PubMed](#)]
64. Luxton, G.W.; Gomes, E.R.; Folker, E.S.; Vintinner, E.; Gundersen, G.G. Linear arrays of nuclear envelope proteins harness retrograde actin flow for nuclear movement. *Science* **2010**, *329*, 956–959. [[CrossRef](#)]
65. Janota, C.S.; Calero-Cuenca, F.J.; Costa, J.; Gomes, E.R. SnapShot: Nucleo-cytoskeletal Interactions. *Cell* **2017**, *169*, 970–971. [[CrossRef](#)]

66. Infante, E.; Castagnino, A.; Ferrari, R.; Monteiro, P.; Aguera-Gonzalez, S.; Paul-Gilloteaux, P.; Domingues, M.J.; Maiuri, P.; Raab, M.; Shanahan, C.M.; et al. LINC complex-Lis1 interplay controls MT1-MMP matrix digest-on-demand response for confined tumor cell migration. *Nat. Commun.* **2018**, *9*, 2443. [[CrossRef](#)]
67. Marks, P.C.; Petrie, R.J. Push or pull: How cytoskeletal crosstalk facilitates nuclear movement through 3D environments. *Phys. Biol.* **2022**, *19*, 021003. [[CrossRef](#)]
68. Calero-Cuenca, F.J.; Janota, C.S.; Gomes, E.R. Dealing with the nucleus during cell migration. *Curr. Opin. Cell Biol.* **2018**, *50*, 35–41. [[CrossRef](#)]
69. Barzilai, S.; Yadav, S.K.; Morrell, S.; Roncato, F.; Klein, E.; Stoler-Barak, L.; Golani, O.; Feigelson, S.W.; Zemel, A.; Nourshargh, S.; et al. Leukocytes Breach Endothelial Barriers by Insertion of Nuclear Lobes and Disassembly of Endothelial Actin Filaments. *Cell Rep.* **2017**, *18*, 685–699. [[CrossRef](#)]
70. Willard, S.S.; Devreotes, P.N. Signaling pathways mediating chemotaxis in the social amoeba, *Dictyostelium discoideum*. *Eur J Cell Biol.* **2006**, *85*, 897–904. [[CrossRef](#)]
71. King, J.S.; Insall, R.H. Chemotaxis: Finding the way forward with *Dictyostelium*. *Trends Cell Biol.* **2009**, *19*, 523–530. [[CrossRef](#)] [[PubMed](#)]
72. Kay, R.R.; Langridge, P.; Traynor, D.; Hoeller, O. Changing directions in the study of chemotaxis. *Nat. Rev. Mol Cell Biol.* **2008**, *9*, 455–463. [[CrossRef](#)] [[PubMed](#)]
73. Nichols, J.M.; Veltman, D.; Kay, R.R. Chemotaxis of a model organism: Progress with *Dictyostelium*. *Curr. Opin. Cell Biol.* **2015**, *36*, 7–12. [[CrossRef](#)] [[PubMed](#)]

Centrosome positioning in migrating *Dictyostelium* cells

Supplementary Materials

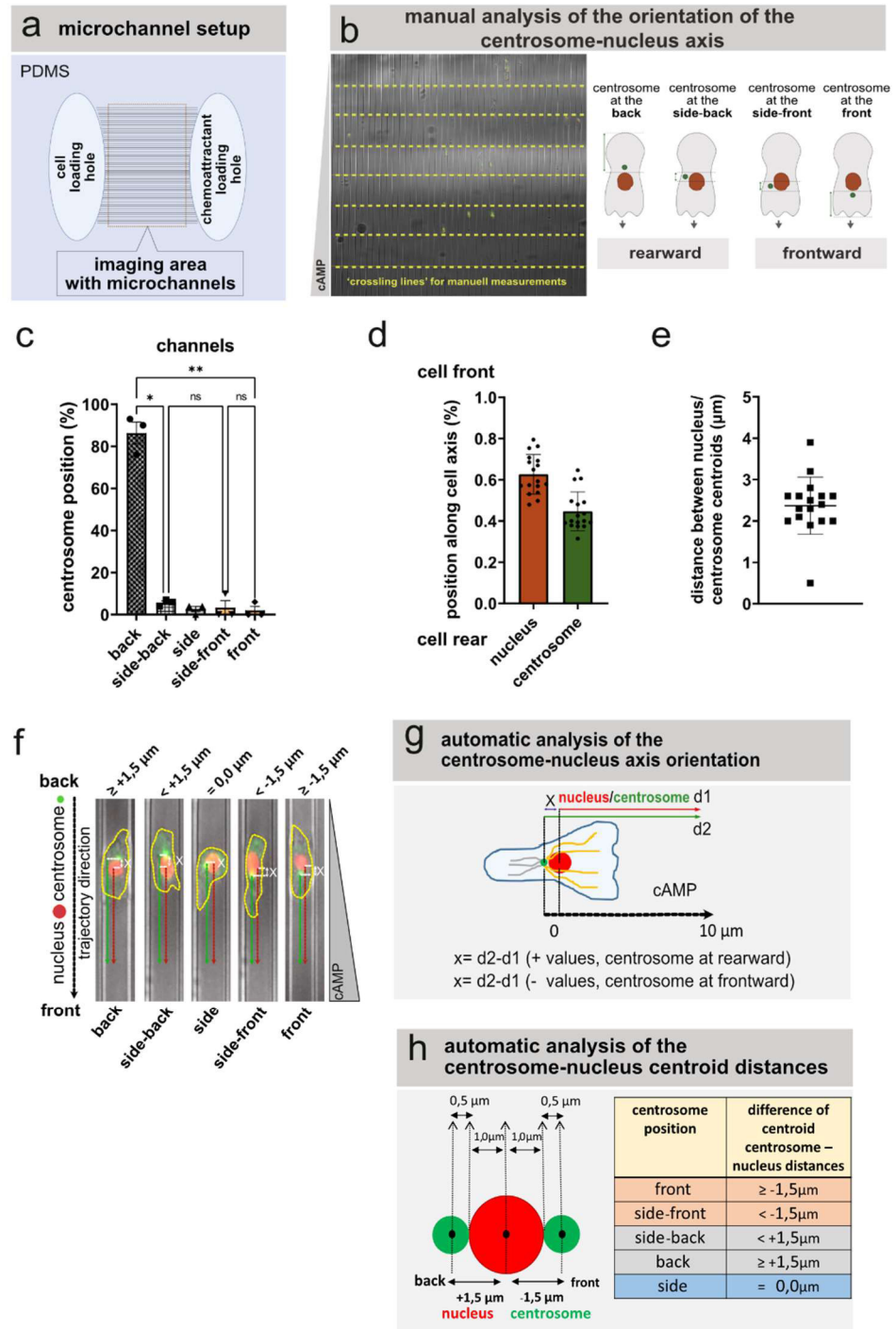


Figure S1. Microchannel setup and manual/automatic analysis of centrosome positioning. (a) Scheme of the PDMS device containing microchannels with one loading hole for cells and one loading hole for the chemoattractant. (b) Scheme illustrating the categories used for the manual quantification of the centrosome position in *Dictyostelium* cells. (c) Manual quantification of the centrosome position of *Dictyostelium* cells migrating in microchannels along a gradient of cAMP. $N = 3$, number

cells = 17. (d) Manual quantification of the positioning of the centrosome and the nucleus along the cell axis during migration in microchannels along a cAMP gradient (0 = cell rear; 1 = cell front). $N = 3$, number of cells = 17. (e) Manual quantification of the centrosome and the nucleus distances along the cell axis during migration in microchannels along a cAMP gradient. $N = 3$, number of cells = 17. (f) Representative microscopy images of a cell migrating in a microchannel along a gradient of cAMP showing how the centroid distances of the centrosome minus the nucleus centroid distances, were used to classify the centrosome position in relation to the nucleus. (g) Scheme illustrating how the automatic quantification was accomplished to classify the centrosome position relative to the nucleus. The distance of the nucleus and centrosome centroids were determined in relation to a reference point (where the cAMP or folate was released). The centroid centrosome distance (d2) minus the centroid nucleus distance (d1) were subtracted. Positive values (+) indicate centrosome is located behind, and negative values (-) indicate that the centrosome is positioned in front of the nucleus. (h) Table giving the threshold values used for automatic determination of centrosome-nucleus centroids as shown in (g).

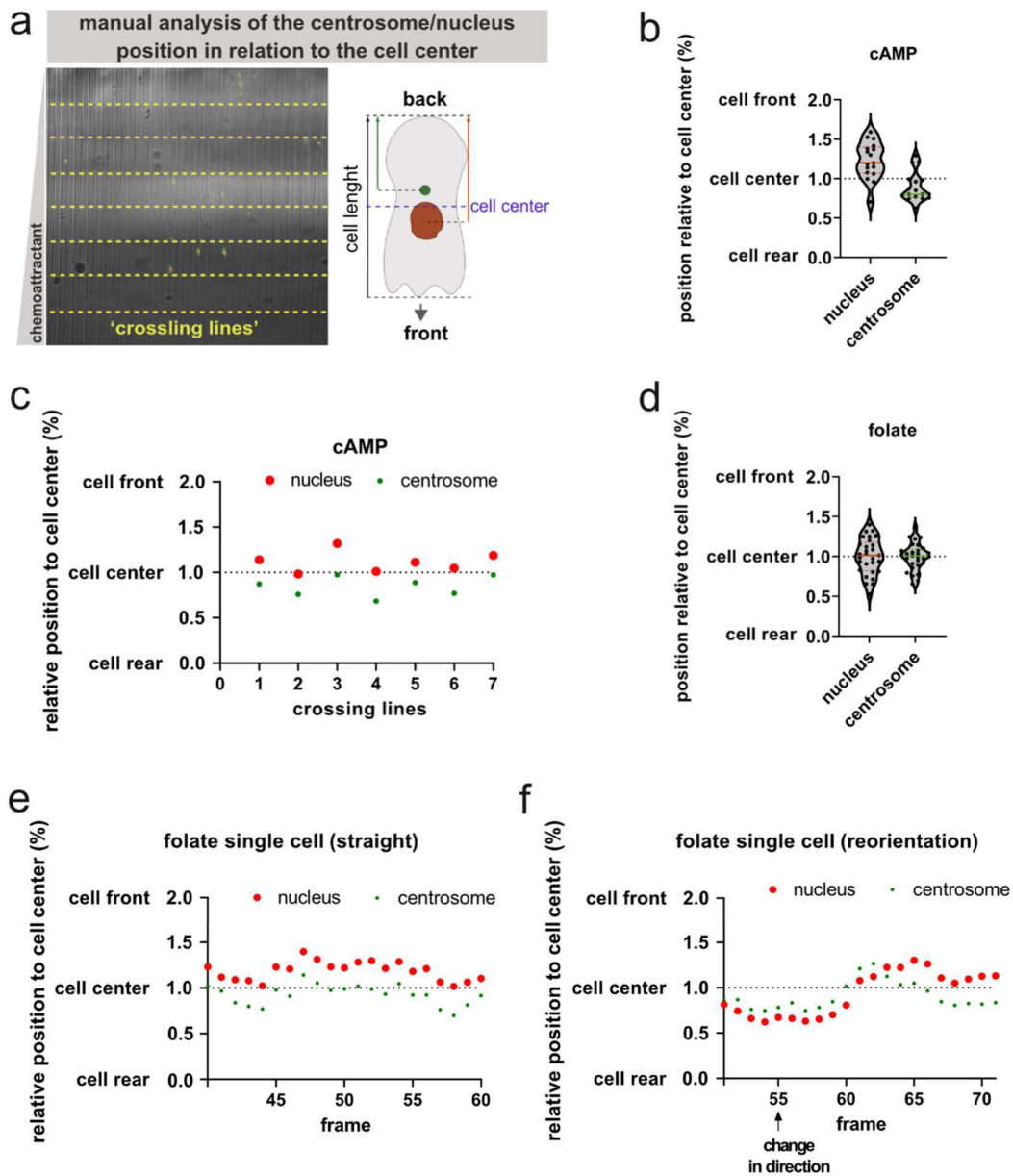


Figure S2. Position of nucleus and centrosome centroids in relation to the cell center. (a) Scheme illustrating the categories used for the manual quantification of the nucleus/centrosome position in relation to the cell center of *Dictyostelium* cells. Seven transverse lines were established as reference (yellow), where only the cells crossing these lines (crossing lines), were quantified for cell length,

cell center, and the distances of nucleus and centrosome centroids to the posterior edge of the cell were measured. To obtain the relative distances of the nucleus and centrosome to the cell center, the nucleus and centrosome centroid distances were divided by the distance of the cell center to the cell rear, giving the value 1.0 as the cell center. **(b and d)** Violin plots showing the distribution of nucleus and centrosome centroids to the cell center of *Dictyostelium* cells migrating in microchannels along a gradient of cAMP **(b)** or folate **(d)**. $N = 3$, number cells = 17 for the cAMP, and $N = 3$, number cell = 29 for the folate experiments. The red and green continuous lines indicate the median, and the dashed lines (red and green) indicate the 25% and 75% quartiles. **(c)** Manual quantification of the relative position of nucleus and centrosome centroids to the cell center of a single cell migrating in microchannels along the seven reference lines in a gradient of cAMP. **(e-f)** Single-frame analysis of the nucleus and centrosome distances relative to the cell center of single cells moving in a gradient of folate. During straight migration, the nucleus is preferentially located at the cell front and the centrosome is positioned closer to the cell center **(e)**. After changing direction, the nucleus re-orientates towards the front of the cell, and the centrosome is positioned behind the nucleus **(f)**. The cells analyzed in **(e and f)** correspond to Video 7.

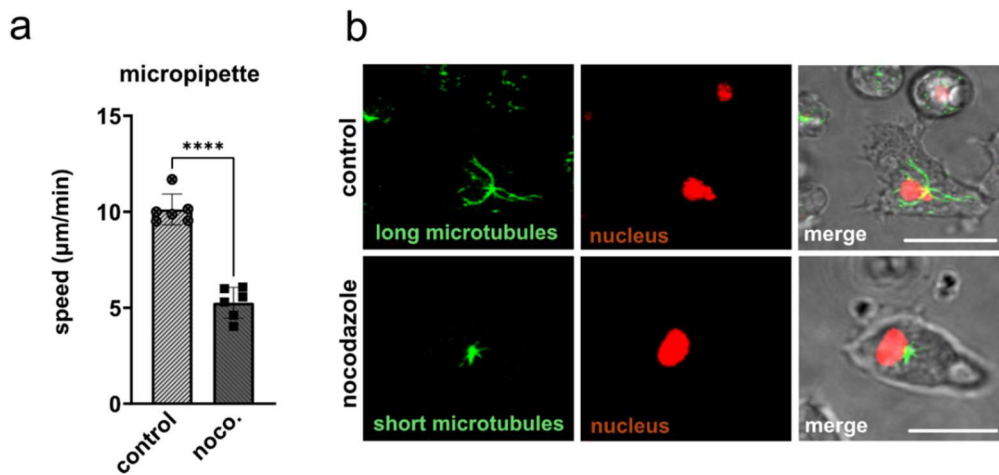


Figure S3. Nocodazole treatment results in decrease of cell speed and shorter microtubules in *Dictyostelium* cells. **(a)** Histograms shows migration speed of *Dictyostelium* cells treated with 30 μM of nocodazole for 1 h in comparison to untreated cells (control). **(b)** Confocal images of a *Dictyostelium* cell expressing GFP-tubulin (green) and mRFP-histone (red) (control), compared to a nocodazole-treated cell. After application of nocodazole, within 1 h long microtubules are massively shortened, and only short stumps emerge from the centrosome. Scale bar is 10 μm .

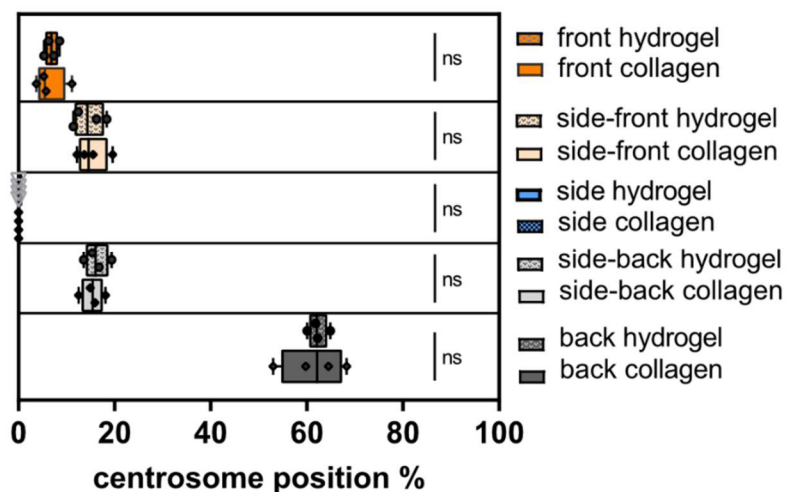


Figure S4. Positioning of the centrosome relative to the nucleus in aggregation competent *Dictyostelium* cells migrating chemotactically in 3D hydrogel or collagen type I matrices. The centrosome position shows a similar distribution under both conditions of folate chemotaxis.

Videos (available only online)

Video S1. The centrosome of *Dictyostelium* cells migrating in microchannels along a cAMP gradient preferentially locates rearward of the nucleus. *Dictyostelium* cells expressing GFP-tubulin (to visualize the centrosome) and mRFP-histone (nucleus) were starved for 8 to 10 h and loaded into a microchannel with a cAMP gradient. Gradient orientation in video: the higher cAMP concentration is at the bottom. The time series was recorded with a frame interval of 10 s. During directed migration of cells in the narrow channels, the centrosome is predominantly found behind the nucleus. Time in min is displayed at the top left. The dots covering nucleus and centrosome in the second part of the movie were generated with the Imaris software. The green dot represents the centrosome, and the red dot is the nucleus. The tracks display the trajectory of the cell toward the chemoattractant source.

Video S2. The centrosome of *Dictyostelium* cells migrating in a micropillar array along a cAMP gradient preferentially locates rearward of the nucleus. *Dictyostelium* cells expressing GFP-tubulin (centrosome) and mRFP-histone (nucleus) were starved for 8 to 10 h and loaded into a micropillar field with a cAMP gradient. Gradient orientation in video: the higher cAMP concentration is at the bottom. The time series was recorded with a frame interval of 10 s. During migration of the cells through the array of micropillars, the centrosome is predominantly positioned rearward of the nucleus. Time in min is displayed at the top left. The dots covering nucleus and centrosome in the second part of the movie were generated with the Imaris software. The green dots represent the centrosomes, and the red dots are the nuclei. The tracks display the trajectories of the cells toward the chemoattractant source.

Video S3. The preferential position of the centrosome of *Dictyostelium* cells during migration toward cAMP released from a micropipette is rearward of the nucleus. *Dictyostelium* cells expressing GFP-tubulin (centrosome) and mRFP-histone (nucleus) starved for 8 to 10 h, are migrating along a gradient of cAMP released from a micropipette tip. The position of the micropipette is visible at the upper left side. The centrosome is predominantly positioned rearward of the nucleus. The time series was recorded with a frame interval of 10 s. Time in minutes is displayed at the top left. The dots covering nucleus and centrosome in the second part of the movie were generated with the Imaris software. The green dot represents the centrosome, and the red dot is the nucleus. The tracks display the trajectory of the cell in the direction of the chemoattractant source.

Video S4. In *Dictyostelium* cells with disrupted microtubules, the position of the centrosome changes frequently from the back to sides and front of the nucleus during migration in a gradient of cAMP released from a micropipette. *Dictyostelium* cells expressing GFP-tubulin (centrosome) and mRFP-histone (nucleus) were starved for 8 to 10 h, and treated with 30 μ M nocodazole for 1 h, are migrating along a gradient of cAMP released from a micropipette tip. The position of the micropipette is visible at the upper left side. When the microtubule network is disrupted, the position of the centrosome relative to the nucleus is much more frequently changing compared to untreated control cells. The time series was recorded with a frame interval of 10 s. Time in minutes is displayed at the top left. The dots covering nucleus and centrosome in the second part of the movie were generated with the Imaris software. The green dot represents the centrosome, and the red dot is the nucleus. The tracks display the trajectory of the cell in the direction of the chemoattractant source.

Video S5. The centrosome of *Dictyostelium* cells is predominantly located behind the nucleus during migration in 3D environments. *Dictyostelium* cells expressing GFP-tubulin (centrosome) and mRFP-histone (nucleus) were starved for 8 to 10 h. Then, the cells were mixed with hydrogel, and the mixture was loaded immediately into the middle channel of a 3D chemotaxis chamber (ibidi). cAMP was loaded into one outer compartment of the channel and PBS into the other one. Gradient orientation in video: the higher cAMP concentration is at the bottom. Time series was recorded with a frame interval of 10 s. The dots covering nucleus and centrosome in the second part of the movie were generated with the Imaris software. The green dot represents the centrosome, and the red dot is the nucleus. The tracks display the trajectory of the cell in the direction of the chemoattractant source.

Video S6. In *Dictyostelium* cells moving in 3D environments, the position of the centrosome is more variable relative to the nucleus when microtubules are disrupted. *Dictyostelium* cells expressing GFP-tubulin (centrosome) and mRFP-histone (nucleus) starved for 8 to 10 h and treated with 30 μ M nocodazole for 1 h, were mixed with hydrogel. The hydrogel-cell mix was loaded into the middle channel of a 3D chemotaxis chamber (ibidi). cAMP was loaded into one end compartment, and PBS

into the other one of the channel. Gradient orientation in video: the higher cAMP concentration is at the bottom. The cells loaded into the middle channel were recorded with a time interval of 10 s per frame. The position of the centrosome relative to the nucleus is much more variable compared to untreated control cells. The dots covering nucleus and centrosome in the second part of the movie were generated with the Imaris software. The green dot represents the centrosome, and the red dot is the nucleus. The tracks display the trajectory of the cell in the direction to the chemoattractant source.

Video S7. The centrosome of *Dictyostelium* cells migrating in microchannels along a gradient of folate preferentially locates rearward of the nucleus. Growth phase *Dictyostelium* expressing GFP-tubulin (centrosome) and mRFP-histone (nucleus) were loaded into microchannels with a folate gradient. Gradient orientation in video: the higher folate concentration is at the bottom. The time series was recorded with a frame interval of 10 s. During directed migration of cells in the narrow channels, the centrosome is predominantly found behind the nucleus. Time in minutes is displayed at the top left. The dots covering nucleus and centrosome in the second part of the movie were generated with the Imaris software. The green dots represent the centrosomes, and the red dots are the nuclei. The tracks display the trajectories of the cells toward the chemoattractant source.

References

- Akhmanova A & Kapitein LC (2022) Mechanisms of microtubule organization in differentiated animal cells. *Nature Reviews Molecular Cell Biology* 23(8): 541–558.
- Alanko J, Uçar MC, Canigova N, Stopp J, Schwarz J, Merrin J, Hannezo E, Sixt M (2023) CCR7 acts as both a sensor and a sink for CCL19 to coordinate collective leukocyte migration. *Science Immunology* 8: eadc9584.
- Alberti S & Hyman AA (2021) Biomolecular condensates at the nexus of cellular stress, protein aggregation disease and ageing. *Nature Reviews Molecular Cell Biology* 22(3): 196–213.
- Andrew N & Insall RH (2007) Chemotaxis in shallow gradients is mediated independently of PtdIns 3-kinase by biased choices between random protrusions. *Nature Cell Biology* 9: 193–200.
- Barbier L, Sáez PJ, Attia R, Lennon-Duménil A-M, Lavi I, Piel M, Vargas P (2019) Myosin II Activity Is Selectively Needed for Migration in Highly Confined Microenvironments in Mature Dendritic Cells. *Frontiers in Immunology* 10: 747.
- Barzilai S, Yadav SK, Morrell S, Roncato F, Klein E, Stoler-Barak L, Golani O, Feigelson SW, Zemel A, Nourshargh S, Alon R (2017) Leukocytes Breach Endothelial Barriers by Insertion of Nuclear Lobes and Disassembly of Endothelial Actin Filaments. *Cell Reports* 18(3): 685–699.
- Bear JE & Haugh JM (2014) Directed migration of mesenchymal cells: where signaling and the cytoskeleton meet. *Current Opinion in Cell Biology* 30: 74–82.
- Berg S, Kutra D, Kroeger T, Straehle CN, Kausler BX, Haubold C, Schiegg M, Ales J, Beier T, Rudy M, Eren K, Cervantes JI, Xu B, Beuttenmueller F, Wolny A, Zhang C, Koethe U, Hamprecht FA, Kreshuk A (2019) ilastik: interactive machine learning for (bio)image analysis. *Nature Methods* 16(12): 1226–1232.
- Bindl J, Molnar ES, Ecke M, Prassler J, Müller-Taubenberger A, Gerisch G (2020) Unilateral Cleavage Furrows in Multinucleate Cells. *Cells* 9(6): 1493.
- Bodor DL, Pönisch W, Endres RG, Paluch EK (2020) Of Cell Shapes and Motion: The Physical Basis of Animal Cell Migration. *Developmental Cell* 52(5): 550–562.
- Bone CR & Starr DA (2016) Nuclear migration events throughout development. *Journal of Cell Science* 129: 1951–1961.
- Bornens M (2008) Organelle positioning and cell polarity. *Nature Reviews Molecular Cell Biology* 9(11): 874–886.
- Calero-Cuenca FJ, Janota CS, Gomes ER (2018) Dealing with the nucleus during cell migration. *Current Opinion in Cell Biology* 50: 35–41.
- Caswell PT & Zech T (2018) Actin-Based Cell Protrusion in a 3D Matrix. *Trends in Cell Biology* 28(10): 823–834.
- Charras G & Sahai E (2014) Physical influences of the extracellular environment on cell migration. *Nature Reviews Molecular Cell Biology* 15: 813–824.
- Charras GT, Hu C-K, Coughlin M, Mitchison TJ (2006) Reassembly of contractile actin cortex in cell blebs. *Journal of Cell Biology* 175(3): 477–490.
- Crisp M, Liu Q, Roux K, Rattner JB, Shanahan C, Burke B, Stahl PD, Hodzic D (2006) Coupling of the nucleus and cytoplasm: role of the LINC complex. *Journal of Cell Biology* 172(1): 41–53.

Davidson PM, Denais C, Bakshi MC, Lammerding J (2014) Nuclear deformability constitutes a rate-limiting step during cell migration in 3-D environments. *Cellular and Molecular Bioengineering* 7(3): 293–306.

Denais CM, Gilbert RM, Isermann P, McGregor AL, Te Lindert M, Weigelin B, Davidson PM, Friedl P, Wolf K, Lammerding J (2016) Nuclear envelope rupture and repair during cancer cell migration. *Science* 352(6283): 353–358.

Devreotes PN & Zigmond SH (1988) Chemotaxis in eukaryotic cells: a focus on leukocytes and Dictyostelium. *Annual Review of Cell Biology* 4: 649–686.

Devreotes PN, Bhattacharya S, Edwards M, Iglesias PA, Lampert T, Miao Y (2017) Excitable Signal Transduction Networks in Directed Cell Migration. *Annual Review of Cell and Developmental Biology* 33: 103–125.

Doyle AD, Wang FW, Matsumoto K, Yamada KM (2009) One-dimensional topography underlies three-dimensional fibrillar cell migration. *Journal of Cell Biology* 184(4): 481–490.

Doyle AD, Nazari SS, Yamada KM (2022) Cell-extracellular matrix dynamics. *Physical Biology* 19(2).

DuChes BJ, Doyle AD, Dimitriadis EK, Yamada KM (2019) Durotaxis by Human Cancer Cells. *Biophysical Journal* 116(4): 670–683.

Fritz-Laylin LK, Riel-Mehan M, Chen B, Lord SJ, Goddard TD, Ferrin TE, Nicholson-Dykstra SM, Higgs H, Johnson GT, Betzig E, Mullins RD (2017) Actin-based protrusions of migrating neutrophils are intrinsically lamellar and facilitate direction changes. *eLife*, 6: e26990.

Gache V, Gomes ER, Cadot B (2017) Microtubule motors involved in nuclear movement during skeletal muscle differentiation. *Molecular Biology of the Cell* 28(7): 865–874.

Gaggioli C, Hooper S, Hidalgo-Carcedo C, Grosse R, Marshall JF, Harrington K, Sahai E (2007) Fibroblast-led collective invasion of carcinoma cells with differing roles for RhoGTPases in leading and following cells. *Nature Cell Biology* 9(12): 1392–1400.

Garde A, Kenny IW, Kelley LC, Chi Q, Mutlu AS, Wang MC, Sherwood DR (2022) Localized glucose import, glycolytic processing, and mitochondria generate a focused ATP burst to power basement-membrane invasion. *Developmental Cell* 57(6): 732-749.e7.

Gärtner F, Reis-Rodrigues P, Vries I de, Hons M, Aguilera J, Riedl M, Leithner A, Tasciyan S, Kopf A, Merrin J, Zheden V, Kaufmann WA, Hauschild R, Sixt M (2022) WASp triggers mechanosensitive actin patches to facilitate immune cell migration in dense tissues. *Developmental Cell* 57: 47-62.

Gomes ER, Jani S, Gundersen GG (2005) Nuclear movement regulated by Cdc42, MRCK, myosin, and actin flow establishes MTOC polarization in migrating cells. *Cell* 121(3): 451–463.

Gundersen GG & Worman HJ (2013) Nuclear positioning. *Cell* 152: 1376–1389.

Hadjitheodorou A, Bell GRR, Ellett F, Shastry S, Irimia D, Collins SR, Theriot JA (2021) Directional reorientation of migrating neutrophils is limited by suppression of receptor input signaling at the cell rear through myosin II activity. *Nature Communications* 12(1): 6619.

Hadjitheodorou A, Bell GRR, Ellett F, Irimia D, Tibshirani R, Collins SR, Theriot JA (2023) Leading edge competition promotes context-dependent responses to receptor inputs to resolve directional dilemmas in neutrophil migration. *Cell Systems* 14(3): 196-209.e6.

Harada T, Swift J, Irianto J, Shin J-W, Spinler KR, Athirasala A, Diegmiller R, Dingal PCDP, Ivanovska IL, Discher DE (2014) Nuclear lamin stiffness is a barrier to 3D migration, but softness can limit survival. *Journal of Cell Biology* 204(5): 669–682.

- Harada Y, Tanaka Y, Terasawa M, Pieczyk M, Habiro K, Katakai T, Hanawa-Suetsugu K, Kukimoto-Niino M, Nishizaki T, Shirouzu M, Duan X, Uruno T, Nishikimi A, Sanematsu F, Yokoyama S, Stein JV, Kinashi T, Fukui Y (2012) DOCK8 is a Cdc42 activator critical for interstitial dendritic cell migration during immune responses. *Blood* 119(19): 4451–4461.
- Infante E, Castagnino A, Ferrari R, Monteiro P, Agüera-González S, Paul-Gilloteaux P, Domingues MJ, Maiuri P, Raab M, Shanahan CM, Baffet A, Piel M, Gomes ER, Chavrier P (2018) LINC complex-Lis1 interplay controls MT1-MMP matrix digest-on-demand response for confined tumor cell migration. *Nature Communications* 9(1): 2443.
- Jimenez AJ, Schaeffer A, Pascalis C de, Letort G, Vianay B, Bornens M, Piel M, Blanchoin L, Théry M (2021) Acto-myosin network geometry defines centrosome position. *Current Biology* 31(6): 1206–1220.e5.
- Jin T, Xu X, Fang J, Isik N, Yan J, Brzostowski JA, Hereld D (2009) How human leukocytes track down and destroy pathogens: lessons learned from the model organism *Dictyostelium discoideum*. *Immunologic Research* 43(1-3): 118–127.
- Kalukula Y, Stephens AD, Lammerding J, Gabriele S (2022) Mechanics and functional consequences of nuclear deformations. *Nature Reviews Molecular Cell Biology* 23(9): 583–602.
- Kameritsch P & Renkawitz J (2020) Principles of Leukocyte Migration Strategies. *Trends in Cell Biology* 30(10): 818–832.
- Képiró M, Várkuti BH, Végner L, Vörös G, Hegyi G, Varga M, Málnási-Csizmadia A (2014) para-Nitroblebbistatin, the non-cytotoxic and photostable myosin II inhibitor. *Angewandte Chemie (International ed. in English)* 53(31): 8211–8215.
- Kirby TJ & Lammerding J (2018) Emerging views of the nucleus as a cellular mechanosensor. *Nature Cell Biology* 20(4): 373–381.
- Knoblauch B & Rachubinski RA (2015) Sharing the cell's bounty - organelle inheritance in yeast. *Journal of Cell Science* 128(4): 621–630.
- Konijn TM, van de Meene JG, Bonner JT, Barkley DS (1967) The acrasin activity of adenosine-3',5'-cyclic phosphate. *Proceedings of the National Academy of Sciences of the United States of America* 58(3): 1152–1154.
- Kopf A, Renkawitz J, Hauschild R, Girkontaite I, Tedford K, Merrin J, Thorn-Seshold O, Trauner D, Häcker H, Fischer K-D, Kiermaier E, Sixt M (2020) Microtubules control cellular shape and coherence in amoeboid migrating cells. *Journal of Cell Biology* 219(6).
- Lämmermann T, Bader BL, Monkley SJ, Worbs T, Wedlich-Söldner R, Hirsch K, Keller M, Förster R, Critchley DR, Fässler R, Sixt M (2008) Rapid leukocyte migration by integrin-independent flowing and squeezing. *Nature* 453: 51–55.
- Lämmermann T, Renkawitz J, Wu X, Hirsch K, Brakebusch C, Sixt M (2009) Cdc42-dependent leading edge coordination is essential for interstitial dendritic cell migration. *Blood* 113(23): 5703–5710.
- Lämmermann T & Sixt M (2009) Mechanical modes of 'amoeboid' cell migration. *Current Opinion in Cell Biology* 21(5): 636–644.
- Lämmermann T & Germain RN (2014) The multiple faces of leukocyte interstitial migration. *Seminars in Immunopathology* 36(2): 227–251.

Lancaster OM, Le Berre M, Dimitracopoulos A, Bonazzi D, Zlotek-Zlotkiewicz E, Picone R, Duke T, Piel M, Baum B (2013) Mitotic rounding alters cell geometry to ensure efficient bipolar spindle formation. *Developmental Cell* 25(3): 270–283.

Liao Y-C, Fernandopulle MS, Wang G, Choi H, Hao L, Drerup CM, Patel R, Qamar S, Nixon-Abell J, Shen Y, Meadows W, Vendruscolo M, Knowles TPJ, Nelson M, Czekalska MA, Musteikyte G, Gachechiladze MA, Stephens CA, Pasolli HA, Forrest LR, St George-Hyslop P, Lippincott-Schwartz J, Ward ME (2019) RNA Granules Hitchhike on Lysosomes for Long-Distance Transport, Using Annexin A11 as a Molecular Tether. *Cell* 179(1): 147-164.e20.

Li R & Gundersen GG (2008) Beyond polymer polarity: how the cytoskeleton builds a polarized cell. *Nature Reviews Molecular Cell Biology* 9(11): 860–873.

Lomakin AJ, Cattin CJ, Cuvelier D, Alraies Z, Molina M, Nader GPF, Srivastava N, Saez PJ, Garcia-Arcos JM, Zhitnyak IY, Bhargava A, Driscoll MK, Welf ES, Fiolka R, Petrie RJ, Silva NS de, González-Granado JM, Manel N, Lennon-Duménil AM, Müller DJ, Piel M (2020) The nucleus acts as a ruler tailoring cell responses to spatial constraints. *Science* 370(6514): eaba2894.

Luxton GWG, Gomes ER, Folker ES, Vintinner E, Gundersen GG (2010) Linear arrays of nuclear envelope proteins harness retrograde actin flow for nuclear movement. *Science* 329(5994): 956–959.

Manstein DJ, Titus MA, Lozanne A de, Spudich JA (1989) Gene replacement in Dictyostelium: generation of myosin null mutants. *The EMBO Journal* 8(3): 923–932.

Mayor R & Etienne-Manneville S (2016) The front and rear of collective cell migration. *Nature Reviews Molecular Cell Biology* 17(2): 97–109.

McGregor AL, Hsia C-R, Lammerding J (2016) Squish and squeeze-the nucleus as a physical barrier during migration in confined environments. *Current Opinion in Cell Biology* 40: 32–40.

Metzger T, Gache V, Xu M, Cadot B, Folker ES, Richardson BE, Gomes ER, Baylies MK (2012) MAP and kinesin-dependent nuclear positioning is required for skeletal muscle function. *Nature* 484(7392): 120–124.

Mitchison TJ & Cramer LP (1996) Actin-based cell motility and cell locomotion. *Cell* 84(3): 371–379.

Moore AS, Coscia SM, Simpson CL, Ortega FE, Wait EC, Heddleston JM, Nirschl JJ, Obara CJ, Guedes-Dias P, Boecker CA, Chew T-L, Theriot JA, Lippincott-Schwartz J, Holzbaur ELF (2021) Actin cables and comet tails organize mitochondrial networks in mitosis. *Nature* 591(7851): 659–664.

Moser M, Legate KR, Zent R, Fässler R (2009) The tail of integrins, talin, and kindlins. *Science* 324(5929): 895–899.

Müller-Taubenberger A, Kortholt A, Eichinger L (2013) Simple system--substantial share: the use of Dictyostelium in cell biology and molecular medicine. *European Journal of Cell Biology* 92(2): 45–53.

Norden C, Young S, Link BA, Harris WA (2009) Actomyosin is the main driver of interkinetic nuclear migration in the retina. *Cell* 138(6): 1195–1208.

Nourshargh S & Alon R (2014) Leukocyte migration into inflamed tissues. *Immunity* 41(5): 694–707.

Odell J, Sikirzhyski V, Tikhonenko I, Cobani S, Khodjakov A, Koonce M (2019) Force balances between interphase centrosomes as revealed by laser ablation. *Molecular Biology of the Cell* 30(14): 1705–1715.

- Padmakumar VC, Libotte T, Lu W, Zaim H, Abraham S, Noegel AA, Gotzmann J, Foisner R, Karakesisoglou I (2005) The inner nuclear membrane protein Sun1 mediates the anchorage of Nesprin-2 to the nuclear envelope. *Journal of Cell Science* 118: 3419–3430.
- Pal DS, Li X, Banerjee T, Miao Y, Devreotes PN (2019) The excitable signal transduction networks: movers and shapers of eukaryotic cell migration. *The International Journal of Developmental Biology* 63(8-9-10): 407–416.
- Paluch E, Piel M, Prost J, Bornens M, Sykes C (2005) Cortical actomyosin breakage triggers shape oscillations in cells and cell fragments. *Biophysical Journal* 89(1): 724–733.
- Paluch EK, Aspalter IM, Sixt M (2016) Focal Adhesion-Independent Cell Migration. *Annual Review of Cell and Developmental Biology* 32: 469–490.
- Pan P, Hall EM, Bonner JT (1972) Folic acid as second chemotactic substance in the cellular slime moulds. *Nature New Biology* 237: 181–182.
- Petrie RJ, Koo H, Yamada KM (2014) Generation of compartmentalized pressure by a nuclear piston governs cell motility in a 3D matrix. *Science* 345(6200): 1062–1065.
- Petrie RJ & Yamada KM (2015) Fibroblasts Lead the Way: A Unified View of 3D Cell Motility. *Trends in Cell Biology* 25(11): 666–674.
- Pflicke H & Sixt M (2009) Preformed portals facilitate dendritic cell entry into afferent lymphatic vessels. *Journal of Experimental Medicine* 206(13): 2925–2935.
- Pollard TD & Borisy GG (2003) Cellular motility driven by assembly and disassembly of actin filaments. *Cell* 112(4): 453–465.
- Quintanilla MA, Hammer JA, Beach JR (2023) Non-muscle myosin 2 at a glance. *Journal of Cell Science* 136(5): jcs260890.
- Raab M, Gentili M, Belly H de, Thiam HR, Vargas P, Jimenez AJ, Lautenschlaeger F, Voituriez R, Lennon-Duménil AM, Manel N, Piel M (2016) ESCRT III repairs nuclear envelope ruptures during cell migration to limit DNA damage and cell death. *Science* 352(6283): 359–362.
- Reinsch S & Gönczy P (1998) Mechanisms of nuclear positioning. *Journal of Cell Science* 111: 2283–2295.
- Renkawitz J, Schumann K, Weber M, Lämmermann T, Pflicke H, Piel M, Polleux J, Spatz JP, Sixt M (2009) Adaptive force transmission in amoeboid cell migration. *Nature Cell Biology* 11(12): 1438–1443.
- Renkawitz J & Sixt M (2010) Mechanisms of force generation and force transmission during interstitial leukocyte migration. *EMBO Reports* 11(10): 744–750.
- Renkawitz J, Kopf A, Stopp J, Vries I de, Driscoll MK, Merrin J, Hauschild R, Welf ES, Danuser G, Fiolka R, Sixt M (2019) Nuclear positioning facilitates amoeboid migration along the path of least resistance. *Nature* 568: 546–550.
- Reversat A, Gaertner F, Merrin J, Stopp J, Tasciyan S, Aguilera J, Vries I de, Hauschild R, Hons M, Piel M, Callan-Jones A, Voituriez R, Sixt M (2020) Cellular locomotion using environmental topography. *Nature* 582(7813): 582–585.
- Ridley AJ, Schwartz MA, Burridge K, Firtel RA, Ginsberg MH, Borisy G, Parsons JT, Horwitz AR (2003) Cell migration: integrating signals from front to back. *Science* 302(5651): 1704–1709.

- Rodriguez-Boulan E & Macara IG (2014) Organization and execution of the epithelial polarity programme. *Nature Reviews Molecular Cell Biology* 15(4): 225–242.
- Roman W & Gomes ER (2018) Nuclear positioning in skeletal muscle. *Seminars in Cell & Developmental Biology* 82: 51–56.
- Roman W, Pinheiro H, Pimentel MR, Segalés J, Oliveira LM, García-Domínguez E, Gómez-Cabrera MC, Serrano AL, Gomes ER, Muñoz-Cánoves P (2021) Muscle repair after physiological damage relies on nuclear migration for cellular reconstruction. *Science* 374(6565): 355–359.
- Sameshima M, Imai Y, Hashimoto Y (1988) The position of the microtubule-organizing center relative to the nucleus is independent of the direction of cell migration in *Dictyostelium discoideum*. *Cell Motility and the Cytoskeleton* 9(2): 111–116.
- Sauer FC (1935) Mitosis in the neural tube. *Journal of Comparative Neurology* 62(2): 377–405.
- Schindelin J, Arganda-Carreras I, Frise E, Kaynig V, Longair M, Pietzsch T, Preibisch S, Rueden C, Saalfeld S, Schmid B, Tinevez J-Y, White DJ, Hartenstein V, Eliceiri K, Tomancak P, Cardona A (2012) Fiji: an open-source platform for biological-image analysis. *Nature Methods* 9(7): 676–682.
- Schumann K, Lämmermann T, Bruckner M, Legler DF, Polleux J, Spatz JP, Schuler G, Förster R, Lutz MB, Sorokin L, Sixt M (2010) Immobilized chemokine fields and soluble chemokine gradients cooperatively shape migration patterns of dendritic cells. *Immunity* 32(5): 703–713.
- Schwarz J, Bierbaum V, Vaahromeri K, Hauschild R, Brown M, Vries I de, Leithner A, Reversat A, Merrin J, Tarrant T, Bollenbach T, Sixt M (2017) Dendritic Cells Interpret Haptotactic Chemokine Gradients in a Manner Governed by Signal-to-Noise Ratio and Dependent on GRK6. *Current Biology* 27(9): 1314–1325.
- SenGupta S, Parent CA, Bear JE (2021) The principles of directed cell migration. *Nature Reviews Molecular Cell Biology* 22(8): 529–547.
- Shellard A & Mayor R (2020) All Roads Lead to Directional Cell Migration. *Trends in Cell Biology* 30(11): 852–868.
- Silva CG, Peyre E, Adhikari MH, Tielens S, Tanco S, van Damme P, Magno L, Krusy N, Agirman G, Magiera MM, Kessaris N, Malgrange B, Andrieux A, Janke C, Nguyen L (2018) Cell-Intrinsic Control of Interneuron Migration Drives Cortical Morphogenesis. *Cell* 172(5): 1063-1078.e19.
- Solecki DJ, Model L, Gaetz J, Kapoor TM, Hatten ME (2004) Par6alpha signaling controls glial-guided neuronal migration. *Nature Neuroscience* 7(11): 1195–1203.
- Solecki DJ, Trivedi N, Govek E-E, Kerekes RA, Gleason SS, Hatten ME (2009) Myosin II motors and F-actin dynamics drive the coordinated movement of the centrosome and soma during CNS glial-guided neuronal migration. *Neuron* 63(1): 63–80.
- Sosa BA, Rothballer A, Kutay U, Schwartz TU (2012) LINC complexes form by binding of three KASH peptides to domain interfaces of trimeric SUN proteins. *Cell* 149(5): 1035–1047.
- Starr DA & Han M (2002) Role of ANC-1 in tethering nuclei to the actin cytoskeleton. *Science* 298(5592): 406–409.
- Starr DA & Fridolfsson HN (2010) Interactions between nuclei and the cytoskeleton are mediated by SUN-KASH nuclear-envelope bridges. *Annual Review of Cell and Developmental Biology* 26: 421–444.
- Stinchcombe JC, Majorovits E, Bossi G, Fuller S, Griffiths GM (2006) Centrosome polarization delivers secretory granules to the immunological synapse. *Nature* 443(7110): 462–465.

- Taverna E & Huttner WB (2010) Neural progenitor nuclei IN motion. *Neuron* 67(6): 906–914.
- te Boekhorst V, Preziosi L, Friedl P (2016) Plasticity of Cell Migration In Vivo and In Silico. *Annual Review of Cell and Developmental Biology* 32(1): 491–526.
- Thiam H-R, Vargas P, Carpi N, Crespo CL, Raab M, Terriac E, King MC, Jacobelli J, Alberts AS, Stradal T, Lennon-Dumenil A-M, Piel M (2016) Perinuclear Arp2/3-driven actin polymerization enables nuclear deformation to facilitate cell migration through complex environments. *Nature Communications* 7: 10997.
- Tsai J-W, Bremner KH, Vallee RB (2007) Dual subcellular roles for LIS1 and dynein in radial neuronal migration in live brain tissue. *Nature Neuroscience* 10(8): 970–979.
- Tsai J-W, Lian W-N, Kemal S, Kriegstein AR, Vallee RB (2010) Kinesin 3 and cytoplasmic dynein mediate interkinetic nuclear migration in neural stem cells. *Nature Neuroscience* 13(12): 1463–1471.
- Tsai TY-C, Collins SR, Chan CK, Hadjitheodorou A, Lam P-Y, Lou SS, Yang HW, Jorgensen J, Ellett F, Irimia D, Davidson MW, Fischer RS, Huttenlocher A, Meyer T, Ferrell JE, Theriot JA (2019) Efficient Front-Rear Coupling in Neutrophil Chemotaxis by Dynamic Myosin II Localization. *Developmental Cell* 49: 189-205.
- Tweedy L, Thomason PA, Paschke PI, Martin K, Machesky LM, Zagnoni M, Insall RH (2020) Seeing around corners: Cells solve mazes and respond at a distance using attractant breakdown. *Science* 369: eaay9792.
- Ueda M, Gräf R, MacWilliams HK, Schliwa M, Euteneuer U (1997) Centrosome positioning and directionality of cell movements. *Proceedings of the National Academy of Sciences of the United States of America* 94(18): 9674–9678.
- van Driessche N, Shaw C, Katoh M, Morio T, Sugang R, Ibarra M, Kuwayama H, Saito T, Urushihara H, Maeda M, Takeuchi I, Ochiai H, Eaton W, Tollett J, Halter J, Kuspa A, Tanaka Y, Shaulsky G (2002) A transcriptional profile of multicellular development in *Dictyostelium discoideum*. *Development* 129(7): 1543–1552.
- van Helvert S, Storm C, Friedl P (2018) Mechanoreciprocity in cell migration. *Nature Cell Biology* 20: 8–20.
- Venturini V, Pezzano F, Català Castro F, Häkkinen H-M, Jiménez-Delgado S, Colomer-Rosell M, Marro M, Tolosa-Ramon Q, Paz-López S, Valverde MA, Weghuber J, Loza-Alvarez P, Krieg M, Wieser S, Ruprecht V (2020) The nucleus measures shape changes for cellular proprioception to control dynamic cell behavior. *Science* 370(6514): eaba2644.
- Weber M, Hauschild R, Schwarz J, Moussion C, Vries I de, Legler DF, Luther SA, Bollenbach T, Sixt M (2013) Interstitial dendritic cell guidance by haptotactic chemokine gradients. *Science* 339(6117): 328–332.
- Weninger W, Biro M, Jain R (2014) Leukocyte migration in the interstitial space of non-lymphoid organs. *Nature Reviews Immunology* 14(4): 232–246.
- Wisdom KM, Adebowale K, Chang J, Lee JY, Nam S, Desai R, Rossen NS, Rafat M, West RB, Hodgson L, Chaudhuri O (2018) Matrix mechanical plasticity regulates cancer cell migration through confining microenvironments. *Nature Communications* 9(1): 4144.
- Wolf K, Müller R, Borgmann S, Bröcker E-B, Friedl P (2003) Amoeboid shape change and contact guidance: T-lymphocyte crawling through fibrillar collagen is independent of matrix remodeling by MMPs and other proteases. *Blood* 102(9): 3262–3269.

- Wolf K, Alexander S, Schacht V, Coussens LM, Andrian UH von, van Rheenen J, Deryugina E, Friedl P (2009) Collagen-based cell migration models in vitro and in vivo. *Seminars in Cell & Developmental Biology* 20(8): 931–941.
- Wolf K & Friedl P (2011) Extracellular matrix determinants of proteolytic and non-proteolytic cell migration. *Trends in Cell Biology* 21(12): 736–744.
- Wolf K, Te Lindert M, Krause M, Alexander S, Te Riet J, Willis AL, Hoffman RM, Figdor CG, Weiss SJ, Friedl P (2013) Physical limits of cell migration: control by ECM space and nuclear deformation and tuning by proteolysis and traction force. *Journal of Cell Biology* 201(7): 1069–1084.
- Worbs T, Hammerschmidt SI, Förster R (2017) Dendritic cell migration in health and disease. *Nature Reviews Immunology* 17(1): 30–48.
- Yamada KM & Sixt M (2019) Mechanisms of 3D cell migration. *Nature Reviews Molecular Cell Biology* 20: 738–752.
- Yoshida K & Soldati T (2006) Dissection of amoeboid movement into two mechanically distinct modes. *Journal of Cell Science* 119(18): 3833–3844.
- Zhang Q, Dove CG, Hor JL, Murdock HM, Strauss-Albee DM, Garcia JA, Mandl JN, Grodick RA, Jing H, Chandler-Brown DB, Lenardo TE, Crawford G, Matthews HF, Freeman AF, Cornall RJ, Germain RN, Mueller SN, Su HC (2014) DOCK8 regulates lymphocyte shape integrity for skin antiviral immunity. *Journal of Experimental Medicine* 211(13): 2549–2566.
- Zwenger M, Ho CY, Lammerding J (2011) Nuclear mechanics in disease. *Annual Review of Biomedical Engineering* 13: 397–428.

Acknowledgements

First, I would like to thank my supervisor Prof. Dr. Jörg Renkawitz for his support, advice, and all the valuable discussions. He was an excellent supervisor during the whole time of my PhD and always more than available for any questions.

Furthermore, I would like to thank the members of my Thesis Advisory Committee PD Dr. Markus Moser and Prof. Dr. Ludger Klein for their helpful advice, insightful comments, and suggestions during our TAC meetings and beyond.

A special thanks goes to all the collaborators involved in this project. To Robert Hauschild for all his help regarding image analysis and software. To Annette Müller-Taubenberger and Hellen Ishikawa-Ankerhold for their help with all the *Dictyostelium* experiments and to Jack Merrin and Lubuna Shafeek for providing us with all the different wafer designs for the microfluidic experiments. It was a pleasure working with you.

Of course, I would like to thank all the current and former members of the Renkawitz lab. I really appreciated the collaborative spirit and all the fun events within and outside of the lab, and of course the coffee breaks in particular.

Finally, I want to thank my family and friends for their encouragement and unceasing support in all respects.